

UNIVERSITY OF BRISTOL

Diamond Betavoltaic Batteries

by

Rhodri Hutchison



A thesis submitted in partial fulfillment for the
degree of Chemical Physics MSci

in the
Faculty of Science
School of Chemistry

April 2017

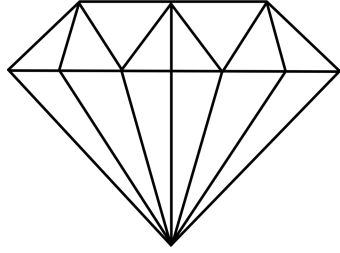
Declaration of Authorship

I, Rhodri Hutchison, declare that this thesis titled, ‘Diamond Betavoltaic Batteries’ and the work presented in it are my own. I confirm that:

- This work was done wholly or mainly while in candidature for a research degree at this University.
- Where any part of this thesis has previously been submitted for a degree or any other qualification at this University or any other institution, this has been clearly stated.
- Where I have consulted the published work of others, this is always clearly attributed.
- Where I have quoted from the work of others, the source is always given. With the exception of such quotations, this thesis is entirely my own work.
- I have acknowledged all main sources of help.
- Where the thesis is based on work done by myself jointly with others, I have made clear exactly what was done by others and what I have contributed myself.

Signed:

Date:



UNIVERSITY OF BRISTOL

Abstract

Faculty of Science
School of Chemistry

MSci Chemical Physics

by Rhodri Hutchison

The next generation of power sources is increasingly sought after as nanoelectronics request both smaller sized and longer lifetime batteries. Nuclear batteries can provide this long lifetime in addition to minimal maintenance, which is crucial for ‘difficult to access’ areas such as space exploration or cardiac pacemakers. Betavoltaic batteries are a type of nuclear battery which convert the kinetic energy of beta particles emitted from a radioactive source into electrical energy across a semiconducting diode junction.

The betavoltaic battery fabricated in this study used the MiP (metal-intrinsic-p-type) configuration, comprised of a metal/undoped diamond/BDD (boron doped diamond) junction, which can take advantage of the exceptionally high intrinsic hole mobility of diamond and overcome the lack of an effective n-type dopant. The MiP battery structure operated as follows: electrons emitted from the beta source penetrated the structure through the p-type diamond and transferred their excess energy to the depletion region of the device, exciting numerous electron-hole pairs per incident particle. Here, the device’s inbuilt electric field ‘pulled’ the mobile carriers to the metal contact on the reverse of the structure to be collected as current.

Numerous research groups have previously demonstrated semiconducting structures that can harness electrical power from a radioactive isotope under beta decay. However, little research has been conducted using semiconducting diamond and none using polycrystalline diamond. Diamond, with its large band gap and high radiation hardness, has exceptional characteristics to produce a large open circuit voltage and long device lifetime when paired with a high quality beta source. These characteristics will benefit the electrical output of betavoltaic battery. The radioisotope used in this study is the pure beta emitting Ni-63, with a long half life of over 100 years and potential to excite numerous excitons per incident beta particle, with negligible deterioration to the diamond structure. The diamond MiP diode structure with added Ni-63 source is assembled in this research

and the electrical properties of the membrane characterised throughout. The project investigates how modifying the Schottky diode structure, particularly by modifying the i-diamond thickness, will give the highest overall efficiency.

A short circuit current of 24 ± 6 nA and an open circuit voltage of 40 ± 4 mV with total device efficiency of 0.1 % was measured. This efficiency is unarguably low when compared to other betavoltaic structures, but it proves the capabilities of using polycrystalline diamond structures as a low-cost alternative to single crystal diamond. Perhaps this result could spur significant research into the use of polycrystalline diamond for electronic applications, similar to the increased use of polycrystalline silicon in the alike structures of photovoltaic devices. A significant increase in the overall efficiency of solar cells has been noted with years of notable breakthroughs in modelling and device optimisation. Betavoltaic batteries are anticipating a similar revolution.

Acknowledgements

I would like to gratefully acknowledge the support from all those who have helped me during the course of this project. Sincere thanks go to Dr Neil Fox for his persistent help and supervision- the many extended email threads and numerous links to papers proved invaluable in my final understanding. I'd also like to thank Professor Paul May for his constructive and critical (but fair!) comments throughout the year. Thanks Paul for helping me to focus on sometimes unconsidered areas of research.

Additionally, many thanks go out to my parents for their crucial help in constructing the final thesis and most importantly for teaching me how to use apostrophes! I would also like to thank my amazing girlfriend for generally putting up with me throughout the year and managing to remain positive even whilst working long weeks. The relentless cups of coffee and gifts/snacks also helped to keep me alive throughout the report writing.

Finally, thank you to all in the Bristol Diamond Group who made being stuck in the basement enjoyable, particular to Alex Croot for just knowing everything about diamonds and showing a constant willingness to help.

Thanks all!

Contents

Declaration of Authorship	iii
Abstract	v
Acknowledgements	vii
1 Introduction	1
1.1 Diamond	1
1.1.1 History	1
1.1.2 Properties	1
1.1.3 High-Pressure High-Temperature	3
1.1.4 Chemical Vapour Deposition	4
1.1.5 CVD Chemistry	6
1.1.6 The Importance of Atomic Hydrogen	7
1.1.7 The Bachmann Triangle	8
1.1.8 Growth Mechanisms	9
1.1.9 Morphology	10
1.1.10 Substrates	11
1.1.11 Nucleation	12
1.1.12 Surfaces	14
1.1.13 Surface Termination	14
1.2 Band Theory	15
1.2.1 Overview	15
1.2.2 Semiconductors	17
1.2.3 Doping	18
1.2.4 Band Bending	19
1.2.5 Semiconductor Heterojunctions	20
1.2.6 Schottky Barrier Height	24
1.2.7 Ohmic Contact	26
1.2.8 Schottky Contact	27
1.2.9 Electron Affinity	30
1.2.10 Mobility	31
1.2.11 Secondary Electron Emission	32
1.3 Batteries	38

1.3.1	History	38
1.3.2	Nuclear Batteries	38
1.3.3	Energy Conversion Techniques	39
1.3.4	Betavoltaic Batteries	41
1.3.5	Efficiency	42
1.3.6	Diamond Betavoltaic Batteries	43
1.3.7	Beta Source	45
1.4	Aims of the Research	46
2	Experimental Method	49
2.1	Diamond Growth	50
2.2	Diamond Characterisation	56
2.3	Metallisation	57
2.4	Electrical Characterisation	59
2.5	Simulation	63
3	Results & Discussion	65
3.1	Diamond Growth	65
3.1.1	Undoped Layer - (i)	65
3.1.2	Substrate Removal	70
3.1.3	Nucleation Face	74
3.1.4	Boron Doped Layer - (P)	77
3.1.5	Thickness Measurements	79
3.2	Metal Contacts - (M)	82
3.3	Device Testing	85
3.3.1	Sheet Resistivity Measurements	85
3.3.2	Current/Voltage Characteristics	86
3.3.3	Beta Illumination	91
3.4	CASINO Simulations	95
3.5	Final Discussion	97
3.5.1	Improved Device Design	99
4	Conclusion	103
4.1	Summary	103
4.2	Future Work	105
A	BDD Layer Trial	107
	Bibliography	111

Chapter 1

Introduction

1.1 Diamond

1.1.1 History

Natural diamond was first discovered in the 4th century BC along the Penner River in India after a growth period of over 900 million years [1]. It became popular for use in the gemstone industry in the 15th century and has remained the most popular choice of ring gemstone for hundreds of years. Diamond was coupled with arguably one of the most popular slogans of the 20th century, ‘a diamond is forever’- conveying the durability of diamond and the lengthy timescales of creation. Despite diamond’s popularity in the gemstone industry, the use of natural diamond in other industrial sectors such as engineering and science decreased due to its rarity and hence high cost. Diamond was commonly used in engineering as a coating for machining tools due to its incredible hardness, but the increasing durability and much lower cost of metal alloys depleted diamond’s effective usage [2, 3]. The scarcity of natural diamond was one of the main driving factors for the development of an effective technique to mass produce synthetic diamond.

1.1.2 Properties

Diamond is a naturally occurring allotrope of carbon, where the carbon atoms are arranged in a variation of the face centered cubic (FCC) crystal structure called the ‘diamond cubic’ structure, with a small lattice constant of 0.3567 nm [4]. Another, more thermodynamically stable allotrope of carbon is graphite. Although the standard enthalpies of diamond and graphite only differ by a few kJ mol^{-1} , a large activation

barrier separates these two phases which causes the interconversion rate between them to be negligible at standard conditions [5]. This activation barrier is what makes diamond so rare to form naturally, but is also responsible for its existence- as once formed, it cannot spontaneously convert back to the more stable phase. Diamond is the metastable allotrope of carbon, being kinetically stable but thermodynamically unstable.

Despite having the same elemental composition, graphite and diamond have very different physical properties due to differences in their lattice arrangements [5]. A carbon atom contains six electrons which occupy the $1s^2 2s^2 2p^2$ electron configuration in the ground state. There are two unpaired electrons in the outer (2p) shell, so it could be naively assumed that carbon could bond to two additional molecules. It has however been proven that carbon has a binding ability of four species- this can be understood by the formation of mixed, or hybridised, states [6]. The 2s and 2p states in carbon are separated by a small energy difference meaning that when subject to an external perturbation, an electron can be excited between these states, resulting in a mixing of the 2s and 2p orbitals.

In graphite, each carbon atom is covalently bonded to three nearest neighbours forming sp^2 hybridised orbitals. This results in strong sheet-like layers weakly bound together by van der Waals forces. Conversely, in a diamond lattice, the carbon atoms are arranged in a tetrahedral structure with each carbon atom sharing one of its outer four electrons with another carbon atom, forming a mixed state of one s-orbital and three p-orbitals (sp^3 hybridised). Within the diamond's 3D sp^3 structure, the bonding strength between each neighbouring carbon atom is equal, and very strong, making diamond one of the hardest known materials [6].

TABLE 1.1: Physical properties of diamond [7].

Property	Value
Hardness	$1.0 \times 10^4 \text{ kg mm}^{-2}$
Young's Modulus	1.22 GPa
Thermal Expansion Coefficient	$1.1 \times 10^{-6} \text{ K}^{-1}$
Thermal Conductivity	$20 \text{ W m}^{-1} \text{ K}^{-1}$
Electron Mobility	$4500 \text{ cm}^2 \text{ V}^{-1} \text{ s}^{-1}$
Hole Mobility	$3800 \text{ cm}^2 \text{ V}^{-1} \text{ s}^{-1}$
Band Gap	5.45 eV
Resistivity	$10^{13} - 10^{16} \text{ } \Omega \text{ cm}$

Apart from diamond's remarkable strength, it also has an exceptional range of physical properties as shown in table 1.1. Notably, diamond has a wide band gap, high carrier

mobility and high thermal stability allowing it to be used in microelectronic devices [8]. Diamond also has an incredible inertness to a vast majority of chemical reagents and large structural rigidity allowing it to be formed into thin films. These properties are those of most interest for use in betavoltaic batteries and will be discussed thoroughly in later sections. There are many other areas of research which explore the vast range of excellent properties of diamond, these are shown in table 1.2. For applications involving high power densities and severe conditions, diamond is often the only material which can meet the relevant characteristics required.

TABLE 1.2: Possible applications of diamond [9].

Application	Primary Author	Year
Cold Cathodes	P.K. Baumann	2000
Radiation Sensors	P. Bergonzo	2001
Electron Multiplication	D.M. Trucchi	2006
Biosensing	C.E. Nebel	2007
Transistors / Superconductors	Y. Takeno	2009
Room Temperature Quantum Computing	M.L. Markham	2011
Bionics	A.E. Hadjinicolaou	2012
Micro-electromechanical systems (MEMS)	O. Auciello	2012
Cutting Tools	X. ding	2012
Optical Windows	R.A. Campos	2013
Electrodes	Y. Zhang	2013

1.1.3 High-Pressure High-Temperature

In order to cope with the increasing demand for synthetic diamond, the first steps to commercial production were conducted by General Electric (GE) in the 1950s [10]. GE initially attempted to mimic the conditions under which diamond was naturally found deep underground by heating carbon under extreme pressure. This was the so-called high-pressure high-temperature (HPHT) growth of diamond and was used to produce ‘industrial’ diamond for several decades. However, the large range of crystal sizes produced by HPHT, along with its high cost, limited the method’s use. To allow the full range of diamond’s properties to be exploited, a method of producing synthetic diamond was required which could consistently grow a preselected grain size with a much lower associated cost.

1.1.4 Chemical Vapour Deposition

Instead of trying to mimic the conditions of natural diamond growth, a method was developed by Eversole in 1958 that attempted to add carbon atoms one by one onto an initial diamond seed crystal [11]. This method, known as chemical vapour deposition (CVD), involved feeding source gases into a chamber, energising them with some external source and providing a suitable substrate for the diamond to grow onto. CVD used much lower growth temperatures and pressures than HPHT and allowed for thin films of diamond to be grown for a much lower cost. However, the growth rates of early CVD diamond were poor due to graphite being co-deposited onto the substrate alongside diamond, leading to significant impurities and hindering growth. This flaw was overcome by the research conducted by Deryagin and co-workers who substantially improved the growth rate and purity of CVD diamond [12]. Despite the many smaller, but significant, improvements to the CVD method over the following years, the next major breakthrough for CVD diamond came in the 1960s when Angus's group discovered the great importance of atomic hydrogen in the growth chamber during diamond deposition. Atomic hydrogen was found to preferentially etch deposited graphite over diamond during the growth process at a factor of 20-30, allowing a higher purity of diamond growth [13]. Succeeding this discovery, additional work by Deryagin in 1976 discovered methods of growing diamond onto non diamond substrates. This series of discoveries triggered the large interest in diamond CVD growth; an interest which is still present.

There are many different types of CVD processes which can grow diamond films, two common variants are hot filament (HF) and microwave plasma (MW). These techniques only differ significantly in the method by which the carbon containing gaseous reactants are activated. In all diamond CVD methods, a hydrogen to carbon carrier gas percentage ratio (usually CH_4) of roughly 99 % is needed to etch any graphitic carbon formed on the substrate [14]. A substrate temperature, typically above 700 °C is also required to ensure formation of diamond rather than amorphous carbon. Both HF and MW CVD will be elucidated further in the following sections.

Matsumoto *et al.* introduced hot-filament activated CVD for diamond growth at the National Institute of Research in Inorganic Materials in 1982 [15]. Since this discovery, HF activated CVD growth of diamond in a dilute CH_4/H_2 gas ratio has proven a well established method of synthetic diamond growth. It allows for low cost diamond growth at low pressures with a growth rate of $>1 \mu\text{m h}^{-1}$ [16]. In a HFCVD reactor, the gaseous reactant molecules are introduced to the chamber where they pass over a filament, drastically increase in temperature and fragment to form reactive radicals. The reactive radicals can then deposit epitaxially onto a substrate material. The filament is electrically heated to a temperature in excess of 2200 °C and is usually constructed of tungsten,

tantalum or rhenium. The first two metals have a relatively low cost but limited lifetime due to their reaction with carbon and formation of a brittle carbide layer. Rhenium carburises very slowly and so has become the filament material of choice for stability and longevity, but it is considerably more expensive than tungsten or tantalum [17]. The quality of diamond growth relies enormously on the performance of these filaments, with a major disadvantage being that the grown films may be contaminated by metal impurities from the filament [18]. A schematic of a typical HFCVD is shown in figure 1.1.

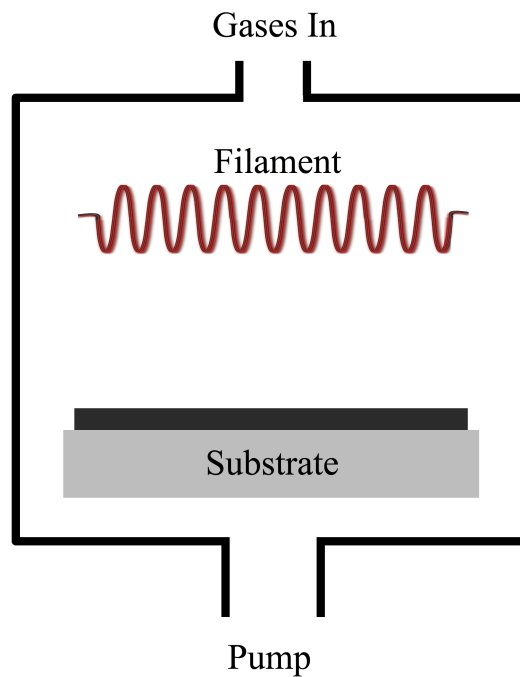


FIGURE 1.1: Schematic diagram of a HFCVD reactor.

Another well established type of CVD reactor is the linear antenna type microwave reactor ¹ [19]. In a MWCVD reactor, the generated microwaves, usually 2.45 GHz, are channelled through a rectangular waveguide and coupled into the deposition chamber through a dielectric (quartz) window. The antenna converts the transverse TE_{10} mode in the rectangular waveguide to the TM_{01} radial mode in the circular cavity. The quartz is cooled to minimise the loss of microwave permeability and hence minimise the amount of reflected power. A three prong tuner also allows the waves to be tuned, helping to minimise this reflection. The microwaves penetrate through the quartz glass and transfer their energy to the source gases beneath, heating the molecules and igniting a plasma. A solid layer is deposited onto a substrate placed just below the plasma ball. A rotary pump is used to keep a constant gas pressure during growth. A schematic of a linear antenna MW reactor is shown in figure 1.2.

¹formerly referred to as an ASTeX style reactor after the company who originally designed it

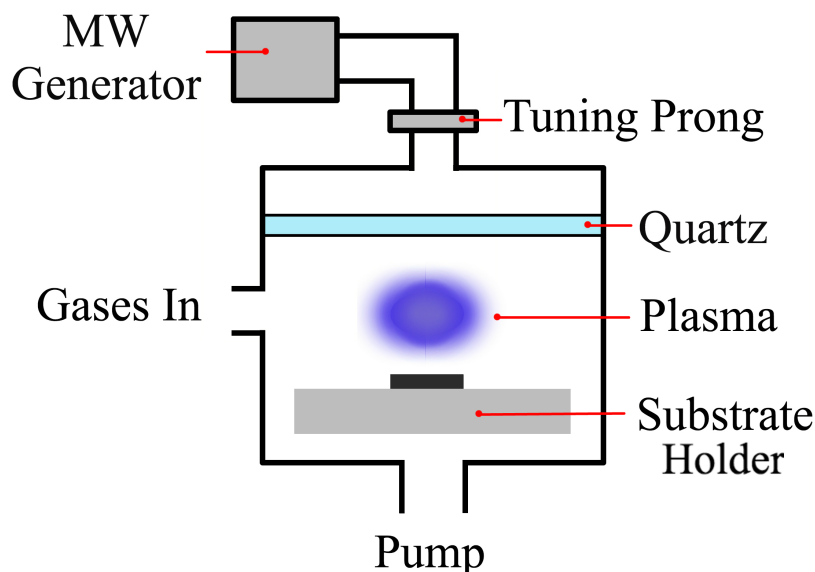


FIGURE 1.2: Schematic diagram of a MWCVD reactor. The blue/purple colour of the plasma is expected for undoped diamond growth.

Using microwaves as the activator allows diverse mixtures of gases to be used. In comparison, HFCVD only allows the use of non corrosive gases and also, the lack of filament makes MWCVD systems intrinsically cleaner than hot filament reactors [20]. The high microwave power achievable can give high growth rates (over $10 \mu\text{m h}^{-1}$) of high crystalline quality diamond which is able to be used in many electronic applications where near perfect crystal growth is paramount [21].

1.1.5 CVD Chemistry

The complex series of chemical reactions which occur during diamond CVD growth can be summarised as follows- the precursor gases, usually CH_4 and H_2 , initially mix in the chamber before passing through an activation region (plasma for the linear MW reactor or the filament in the HF reactor) where they heat to a few thousand Kelvin and form reactive radicals such as H and CH_x where $x=1, 2$ or 3 . These radicals continue to mix and diffuse towards the substrate where they can either desorb back into the gas phase or, if an appropriate site is found, can adsorb onto the surface [22]. The outcome is that both graphitic carbon and diamond will grow over the substrate; it is here where the high percentage of atomic hydrogen is used to etch the graphite allowing for pure sp^3 bonded diamond growth. This process is pictorially shown in figure 1.3 for the example of a HF reactor. Numerous groups have studied the gas phase chemistry which occurs above the substrate surface in diamond growth and it is now believed that atomic hydrogen and

CH_3 are the most crucial components in the gas phase system and it is these molecules which drive the entire chemical process [12, 23].

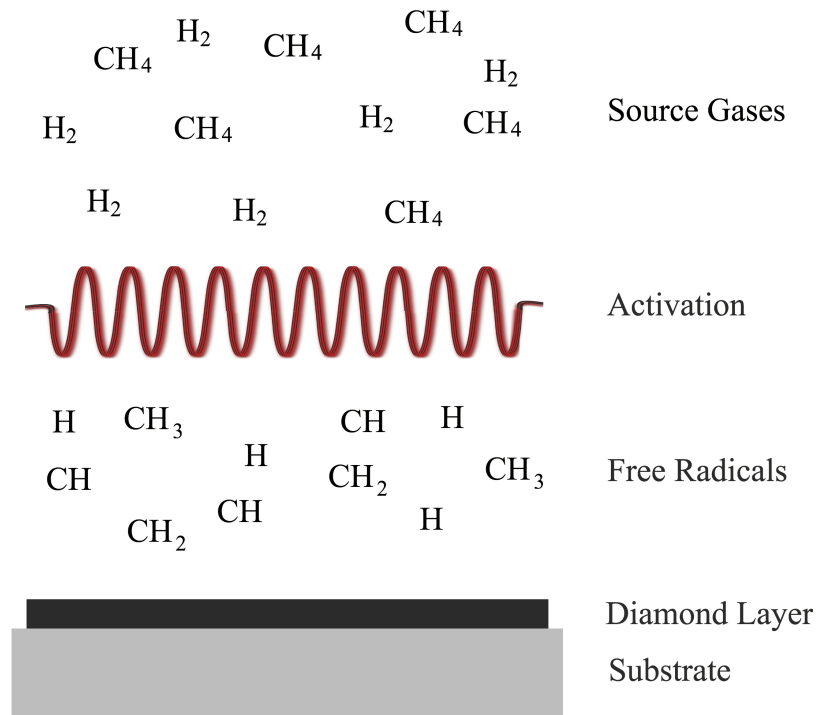


FIGURE 1.3: Schematic of free radical formation as the source gases pass an activation region. The activator is shown as a hot filament in this case. Adapted from [14].

1.1.6 The Importance of Atomic Hydrogen

A high concentration of atomic hydrogen to other CVD gases (predominantly CH_4) during diamond growth is crucial for many processes. As previously discussed, atomic hydrogen etches graphitic sp^2 carbon considerably faster than sp^3 carbon [24]. This removes any graphitic clusters from the surface of the substrate, whilst leaving the diamond behind. H atoms can also effectively break down long chain hydrocarbons into smaller pieces. This considerably lowers the amount of cyclic polymers in the chamber which then limits the amount deposited onto the substrate. H atoms can additionally break down neutral methane into reactive radicals which can attach to the surface on suitable sites. The bulk of diamond is tetrahedrally bonded, but at the surface there are a number of ‘dangling bonds’ which, without termination, could cross-link to form graphite. Hydrogen terminates this free bond at the surface, keeping the sp^3 lattice stable.

Atomic hydrogen is created by electron impact dissociation of hydrogen gas (H_2) in a MW reactor and by molecular hydrogen dissociation in a HF reactor [25]. These reactions are shown in 1.1 and 1.2 respectively.



1.1.7 The Bachmann Triangle

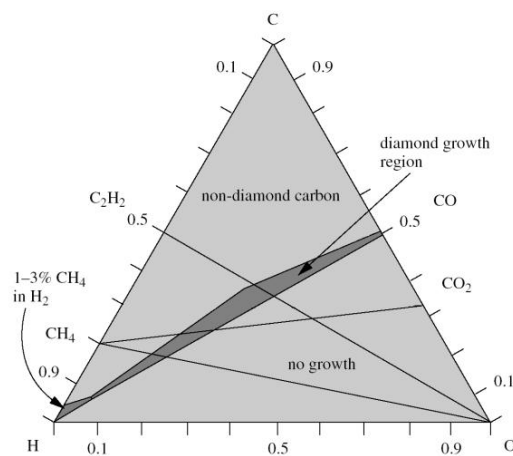


FIGURE 1.4: Simplified C-H-O composition diagram (Bachmann triangle). Normal diamond growth is labelled in the lower left corner [14].

The most important components of CVD growth (C, H and O) can be condensed into a C-H-O composition diagram known as the ‘Bachmann triangle diagram’ (shown in figure 1.4) after its founder [23]. Bachmann found that diamond could only grow when the gas mixture was just above the CO tie line deducing that the diamond growth was independent of the nature of the gaseous precursors and instead dependant on the C, H, O ratio. This suggested that the gas phase reactions effectively broke the reactants into its constituent components instantaneously. Most CVD experiments contain low percentages of CH_4 in H_2 and are restricted to the lower left corner of the phase diagram.

1.1.8 Growth Mechanisms

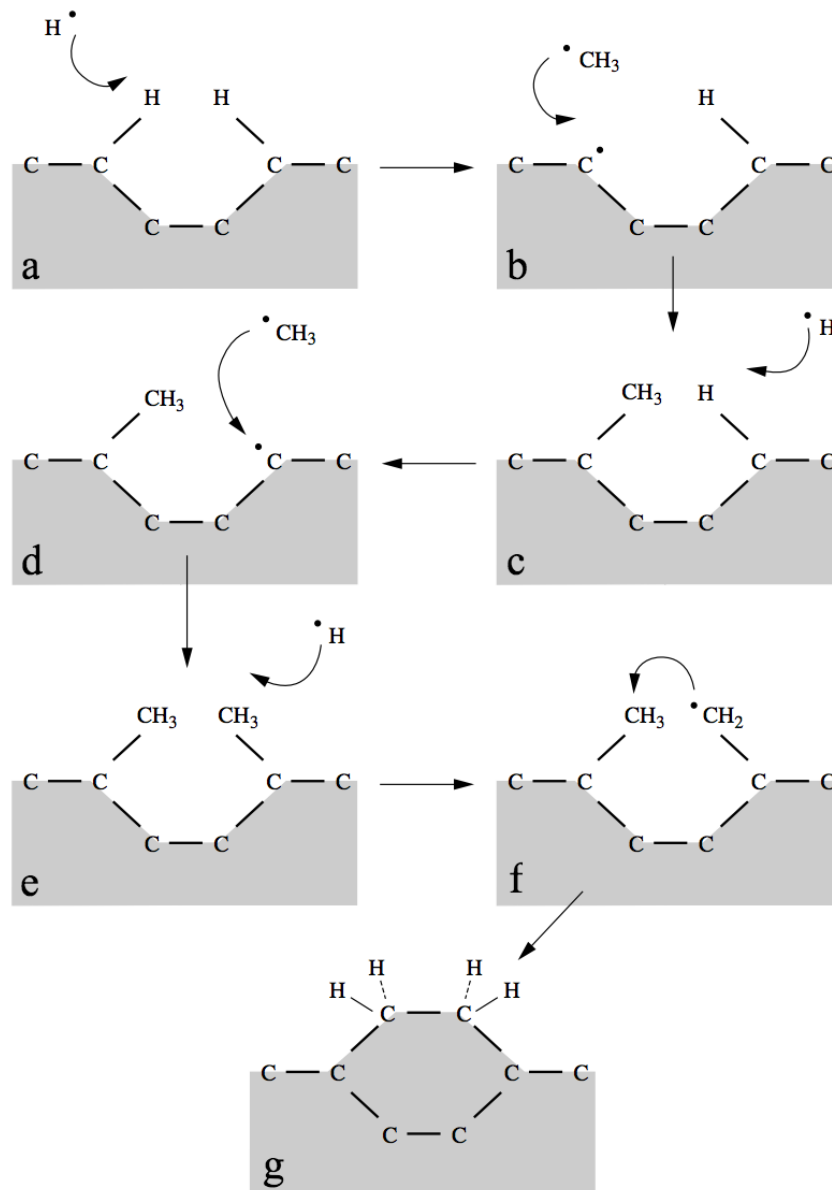


FIGURE 1.5: Schematic representation of diamond growth at a (100) diamond surface—showing step by step the addition of methyl radicals. Diagram adapted from citation [14].

A simplified schematic of CVD diamond growth at a (100) surface is shown in figure 1.5. The diamond surface is predominantly covered with hydrogen during growth as depicted in figure 1.5a. If a gaseous atomic H atom comes near a surface H atom, it may react to form H₂, leaving a surface radical site behind, as depicted by the first two diagrams in figure 1.5. This surface site is highly reactive and will encourage adsorption of the activated gaseous radicals [26]. The most common fate for this form of site is for atomic hydrogen to adsorb onto it, bringing the surface back to its original condition

[14]. Occasionally a hydrocarbon radical, usually CH_3 , may adsorb to these surface sites, adding a carbon to the surface (shown in figure 1.5b and c). This same process of surface hydrogen abstraction and hydrocarbon radical addition may also occur at an adjacent lattice site, leaving two ‘dangling’ methyl groups (figure 1.5e). A final H abstraction from one of these methyl groups creates a radical, which can attack the neighbouring methyl group, closing the ring. This is shown in the final two diagrams in figure 1.5. This method has effectively added two carbon atoms to the diamond lattice. Although this method is (very) simplified due to neglects of all other surface activity, it portrays the standard growth mechanism of (100) surface growth well [27].

1.1.9 Morphology

Different diamond applications will need different classes of film, from single crystal to polycrystalline- where polycrystalline films can be microcrystalline (MCD), nanocrystalline (NCD) or ultrananocrystalline (UNCD) diamond, dependant on the average size of crystals that comprise it. Single crystal films have minimal grain boundaries and can be thought of as perfect, unbroken lattices (although not strictly true) which are optically transparent. Polycrystalline films have a large amount of defects caused by grain boundaries between the numerous small grains and appear dark due the strong light absorption and scattering. Single crystal diamond films are the most attractive diamond form for electronic applications as they contain the lowest number of grain boundaries. These are hence inherently high purity [28]. They also have a higher electrical resistance than polycrystalline diamond.

However, compromises must often be made between the mechanical/electrical properties and the price of the structure. Polycrystalline diamond is significantly lower cost to manufacture than single crystal diamond. High purity polycrystalline diamond still has excellent electrical properties (approaching that of single crystal diamond) and has the added ability to be grown by CVD on a number of non-diamond substrates [29]. Single crystal diamond growth on non-diamond substrates is significantly more difficult. The morphology of polycrystalline diamond can be altered by changing the growth conditions (pressure, MW power, temperature, duration, substrate material) and the concentrations of precursor gases.

In addition to the conditions under which the diamond is grown affecting the morphology, the grain sizes are also expected to increase with a longer growth duration [30]. The grain boundaries of polycrystalline diamond play a crucial role in many of the noted characteristics of diamond and so the variation of grain size with growth duration must be considered in device manufacture. The resistivity of polycrystalline diamond increases

with increasing grain sizes. Larger grain sized diamond also allows for longer charge carrier lifetimes and hence diffusion lengths due to grain boundaries being active recombination sites for charge carriers [31]. These actions make larger grain sizes more effective than smaller grains for electrical applications of polycrystalline diamond.

The morphology of the diamond surface will greatly impact the quality of interfaces in a structure; a higher surface roughness will reduce the contact between materials at an interface, reducing the contact efficiency. CVD diamond surfaces can be polished to a uniform flatness of approximately 5 nm using rotating polishing pads and a colloidal soft particle solution alongside a number of other methods. But, all have proved time consuming and expensive and so are only considered when there is no other alternative [32]. The geometry of the surface will also dictate the penetration and emission of electrons from the diamond. Larger surface areas will limit electron backscattering and result in a larger penetration depth for a given energy primary electron. The surface area of diamond can be increased, minimising backscattering, by milling channels into the material with length scales proportional to the wavelength of the incoming electron [33]. The morphology of the diamond must be considered when manufacturing a betavoltaic device as the structure must allow for efficient electron transport. A betavoltaic structure also comprises of a number of different layers- making sufficient contacts between them is crucial to the power output of the battery.

1.1.10 Substrates

As well as being able to alter the properties of synthetic diamond by changing the growth conditions, the substrate on which the growth occurs greatly affects the type of diamond crystals formed. Diamond growth occurs when carbon atoms are added one by one to a diamond surface in a tetrahedral structure. If the substrate is made of diamond itself, (homoepitaxial) growth can occur immediately as a simple extension of the substrate lattice. However, if the substrate material is anything other than diamond (heteroepitaxial growth), the criteria below must be met before nucleation can occur and diamond growth can commence:

1. The substrate must have a melting point higher than the temperature of diamond growth required to avoid deformation of the substrate under growth conditions.
2. The substrate material must be capable of forming a thin carbide layer. This layer aids the adhesion of diamond to the substrate by a partial relief of stresses at the interface that are due to a mismatch in lattice constants [34].

3. The thermal expansion coefficient of the substrate material must be comparable with that of diamond to avoid blistering of the deposited film as the sample cools after growth.

In some cases, note 2 is ignored and a substrate unable to form a carbide layer may be used in order to make free standing diamond films. In these cases, the diamond film will not adhere to the substrate and will delaminate after deposition.

If the CVD process were to happen at lower temperatures, selection of a suitable substrate for diamond growth could be made remarkably easier. Copious research groups have investigated low temperature diamond deposition in recent years with varying levels of success [35, 36]. But, until a sound method is finalised, silicon will continue to be utilised as the most frequently used substrate material for polycrystalline diamond growth due to its high melting point, low thermal expansion coefficient and ability to form a localised carbide layer [14]. Single crystal silicon wafers are also accessible and low cost [37].

It is widely believed that CVD grown single crystal diamond requires a single crystal diamond substrate material. Numerous authors argue that this is not the case [38]. However, the methods utilised to bypass the need for a single crystal substrate require copious thin layer differing materials followed by a difficult removal of the unwanted substrate by mechanical polishing. The complexity of the production process makes this unfavourable and the vast majority of single crystal diamond is bought from commercial diamond suppliers, costing approximately 30 times the price of a polycrystalline equivalent [39]. Alongside the increased cost of single crystal diamond, the small size of substrates currently available limits the scalability of the final structures [40]. Due to the higher cost and limited size of single crystal diamond, efforts are moving into manufacturing devices from polycrystalline diamond. This same activity was previously seen for silicon in the photovoltaic industry. Polycrystalline silicon solar cells are now being manufactured over much larger areas than single crystal cells at a fraction of the cost. Unfortunately, this is coupled with significantly lower efficiencies [41].

1.1.11 Nucleation

During homoepitaxial growth, an sp^3 tetrahedral lattice is already present and so the diamond growth can grow ‘atom by atom’ as described previously (section 1.1.8). However, when the sample is non-diamond (e.g. Si), there is no base structure for the diamond growth to continue and the majority of deposited carbon atoms are instantaneously etched back into the gas phase by the presence of atomic hydrogen. Thus, without any pretreatment of the substrate, the nucleation density of diamond is very low. Extensive

research on diamond nucleation methods has been completed and the nucleation density of a clean Si substrate has been shown to increase from less than 10^5 cm^{-2} to 10^{11} cm^{-2} using a variety of techniques [42, 43]. The most popular methods utilised are primarily manual abrasive techniques as they are low cost, simple to conduct and effective. A number of nucleation enhancing techniques will be described below.

By simply mechanically polishing the substrate surface using a diamond grit (10 nm - 10 μm), it has been found that both the microscopic scratches on the surface and diamond crystals implanted into the surface, increase the nucleation density [44]. The defects created by the abrasion will act as favourable sites for diamond growth and any residual diamond particles from the abrasion will act as seed crystals for growth of the tetrahedral diamond structure. The nucleation density of the substrate has been found to increase with decreasing diamond grain size [42]. Abrasion with non-diamond powders (SiC and stainless steel) have also been found to increase the nucleation density, although non-diamond powders do not benefit from the addition of diamond seeds and so the nucleation density is lower [45, 46].

Another method used to increase the nucleation density of CVD diamond growth, in a more controlled manner, is abrasion by ultrasonic treatment. The substrates to be seeded are immersed into a slurry of diamond powder ($< \mu\text{m}$ diameter) before agitation within an ultrasonic bath. When removed from the bath, the diamond seeds stick to the surface of the substrate by electrostatic or van der Waals forces. This method has proven to give high nucleation densities of 10^{10} cm^{-2} when using a nanodiamond suspension with a 150 nm average grain size [47].

Although abrasive methods have been proven as a worthy method to increase the nucleation rate for synthetic diamond growth; its resultant roughness makes it inadequate for use where the condition of single crystal diamond films is paramount. This is especially relevant within the electronics industry where circuit geometries are often less than micrometres in length and high quality diamond is required [48].

The most widely used process of substrate pre-treatment in electronics is bias-enhanced nucleation (BEN). BEN has the advantage of negligible damage to the substrate but its disadvantage is that it is only effective when working with conducting or semiconducting substrates. BEN works by negatively biasing the substrate (approximately 200 V) for the initial few minutes of growth under standard CVD conditions [49]. For diamond growth, BEN attracts the carbon containing atoms to the substrate and causes them to penetrate beneath the surface, resulting in a high carbon concentration in the top few layers of the substrate. This saturated carbon layer greatly increases the initial nucleation rates as well as providing a diamond template onto which the CVD diamond can grow. By

altering the biasing of the substrate, the implantation of the carbon rich layer can be adapted and the orientation and texture of the diamond growth can be adjusted [50].

1.1.12 Surfaces

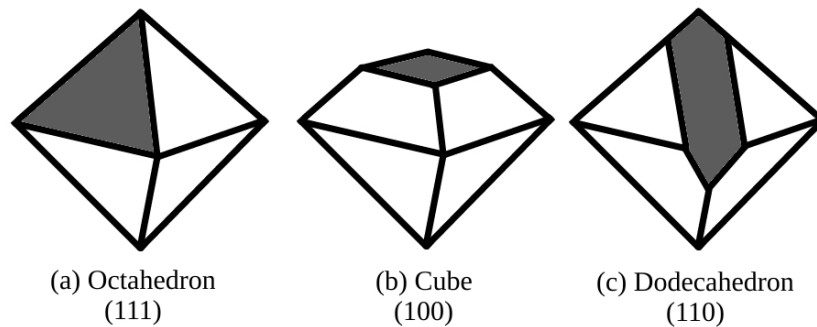


FIGURE 1.6: Schematic showing the locations of a) (111), b) (100) & c) (110) planes on an octahedron diamond crystal. Diagram redrawn from citation [51].

Three lattice planes which are most important for growth and functionalisation of diamond are the (100), (110) and (111) planes and are shown in figure 1.6. These surfaces must be understood in order to take advantage of their differing properties (e.g. surface state densities and bond strengths) when creating diamond structures [51]. The rate of diamond growth on each of these surfaces is dependent on the temperature and gas concentrations of CVD growth and consequently, the morphology of the crystal growth can be altered by changing the parameters of growth.

The {110} and {111} diamond faces have one dangling bond per adatom whereas {100} diamond has two. Growth on diamond {100} planes forms a cubic morphology which is planar and smooth with considerably fewer defects than the other main planes. This makes the {100} diamond planes the key area for experimental and theoretical studies. {111} diamond growth is a quicker but more complicated process which forms octahedral crystallites. The {111} planes are the natural cleavage planes in a diamond crystal due to their lower bond densities [52]. The {110} planes are the fastest growing diamond surfaces under typical deposition conditions, but are less well defined and have not been as extensively studied as the other two [7].

1.1.13 Surface Termination

Many of the electronic properties of diamond are a result of dipole formation, constructed by termination of the dangling surface bonds with a non-carbon molecule. Without this surface termination, the dangling surface bonds cross link to form undesirable graphitic

sp² carbon. Termination of diamond surfaces, usually with hydrogen or oxygen, is a widely researched topic and has been proven to benefit a number of different uses [53].

Hydrogenation of the {111} diamond surfaces gives CVD diamond a negative electron affinity (the conduction band energy is higher than the vacuum energy level) which greatly enhances the secondary electron emission yield (the number of secondary electrons emitted per incident particle) of the sample [54]. These effects are of interest when creating an efficient diamond battery structure and are discussed in depth in sections 1.2.9 and 1.2.11 respectively. Alongside the emission enhancements of a H-terminated diamond surface, the termination has also been found to stabilize the lattice up to temperatures of roughly 900 °C, increasing the structural rigidity of thin film structures due to the high C-H bond energy of 4.2 eV [55, 56]. H-termination of a diamond surface can be executed in a CVD reactor after diamond growth completion using a hydrogen plasma at approximately 700 °C [57].

Oxygen termination of a diamond surface is found to dramatically increase the surface resistivity and also increase the Schottky barrier height (section 1.2.6) of metal to diamond contacts [58]. O-termination of a diamond surface can be simply conducted through a 30 minute UV light irradiation in an oxygen atmosphere [59]. However, the most thorough method is by immersion in a hot mixture of HNO₃/H₂SO₄ acid [60]. This wet-oxidation is an effective way of removing all surface contaminants (metals, graphitic carbon, previous terminations or organic compounds) and replacing them with an oxidised surface.

1.2 Band Theory

1.2.1 Overview

Band theory, an adapted model of molecular orbital theory, can be used to explain the bonding of conductors, insulators and semiconductors as follows. As atoms come together, their atomic orbitals form molecular orbitals of the product compound. In the case of two atoms, the two atomic orbitals overlap and each split into two molecular orbitals with differing energies (due to the Pauli exclusion principle). As much larger numbers of atoms are introduced, as seen in a crystal lattice ($N \approx 10^{20}$), the atomic orbital energies are in such close proximity that they overlap and each atomic orbital splits into N discrete molecular orbitals². The large number of energy levels are now so closely spaced that they can be assumed to form a continuous energy band. This is known as the ‘tight binding approximation’, which states that electrons which occupy a partially filled band are able to populate all accessible energy levels and allow electrical conduction.

²where N is an integer number of atoms

Many interesting properties of a material can be established from the combination of their energy bands and energy differences.

The ‘band diagram’ was developed by Painter, Ellis and Lubinsky in the 1970s using ‘*ab Initio*’ calculations as a diagrammatic way of explaining band theory [61]. Band diagrams graphically show the energy levels of a variety of bands (most importantly the valence and conduction bands) as a function of a spatial dimension. The highest electron energy states at absolute zero temperature form the valence band and the lowest vacant electron states form the conduction band. The energy difference between the valence band maximum (E_v) and conduction band minimum (E_c) is known as the band gap (E_g) and it is this gap which fundamentally determines the electronic properties of a material.

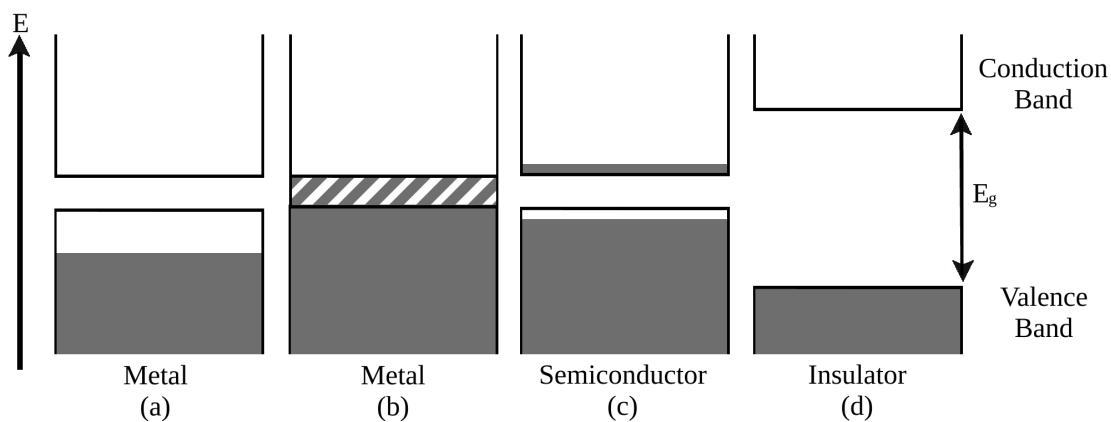


FIGURE 1.7: Band diagram showing the energy level differences between a metal (a & b), semiconductor (c) and insulator (d).

A band diagram of a simple metal, semiconductor and insulator are shown in figure 1.7. For a material to conduct, it can either have a half filled valence band (shown in figure 1.7a) or have an overlap of the valence and conduction bands (shown in figure 1.7b). Importantly, if the material has one valence electron per atom, then the valence band will be half filled and the material will conduct. If there is an overlap in the valence and conduction bands of a material then the electrons are essentially ‘free’ and able to move through the material and they can also conduct. In insulators, the electrons in the full valence band are separated by a large band gap from the empty conduction band and consequently there is no conduction (shown in figure 1.7d). In semiconductors, the band gap is small and therefore external excitations (e.g. thermal energy) can cause electrons (and holes) to bridge this energy difference. This is shown pictorially in figure 1.7c by an ‘almost full’ valence band separated by a small band gap from an ‘almost empty’ conduction band. ‘Holes’ are positive charge carriers at a position in a lattice where there is a lack of an electron. Holes are introduced to simplify the discussion of almost full bands due to the ease of tracking a single hole rather than monitoring the many

electrons in the almost full band. Although not a physical particle, holes are the second charge carrier (alongside electrons) responsible for current in semiconducting materials.

Many of a material's electrical properties can be explained by the differences in their energy bands- some of the most common are depicted in the semiconductor to vacuum interface shown in figure 1.8 and will be referred to extensively in later sections.

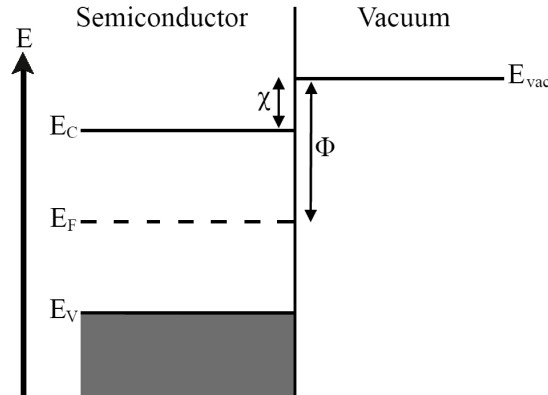


FIGURE 1.8: Band diagram labelling the energy level differences of a semiconductor to vacuum interface.

The electron affinity (χ) of a material is the energy required for an electron in the conduction band to emit from the surface and is shown on a band diagram as the energy difference between the conduction band minimum and the vacuum energy E_{vac} . The Fermi level (E_F) of a material represents the maximum energy an electron occupies in a material at 0 K. The work function (Φ) is the energy difference between the vacuum energy level and the Fermi level.

1.2.2 Semiconductors

The electronic properties of semiconducting materials are dominated by the highest partially empty band and the lowest partially filled band. At absolute zero temperature (0 K), semiconductors behave as insulators, as electrons cannot surpass the energy band gap, and the conduction and valence bands remain as an empty and filled band respectively. Above this temperature, thermal excitations in the material may cause electrons from the valence band to ‘jump’ into the conduction band, allowing the material to electrically conduct. The power of semiconductor materials comes from the ability to change their electronic properties through the intentional addition of impurity atoms (defects) to the crystal lattice. The addition of impurities to the lattice is called doping. A semiconductor with no significant dopant concentration is known as an intrinsic, or i-type, semiconductor (e.g. i-diamond). Semiconductors with additions of significant concentrations of dopants are called extrinsic semiconductors.

1.2.3 Doping

Pure diamond has a wide band gap of 5.45 eV making it electrically insulating, but it can be doped by other materials with either donor or acceptor impurities to explore its semiconducting properties- ranging from insulating to near metallic conduction [62]. Dopants enhance the electrical conductivity of the material by allowing extra energy levels into the band gap from which either electrons can excite into the conduction band or holes can excite into the valence band. n-type (negative) semiconductors have extra electron (donor) energy levels near the conduction band and p-type (positive) semiconductors have extra hole (electron acceptor) levels near the valence band. These structures are illustrated in figure 1.9. The electron donor level is shown at the top of the band gap in figure 1.9 by E_d and the electron acceptor (hole donor) level is at the bottom of the band gap and shown by E_a . The more abundant charge carriers in a semiconductor are known as majority carriers and are responsible for most of the conduction in the material. The compact, close packing of the diamond lattice affords limited substitutional space for dopants, only a few dopant species have been successfully incorporated into the lattice during the growth process [63]. The most common will be explained below.

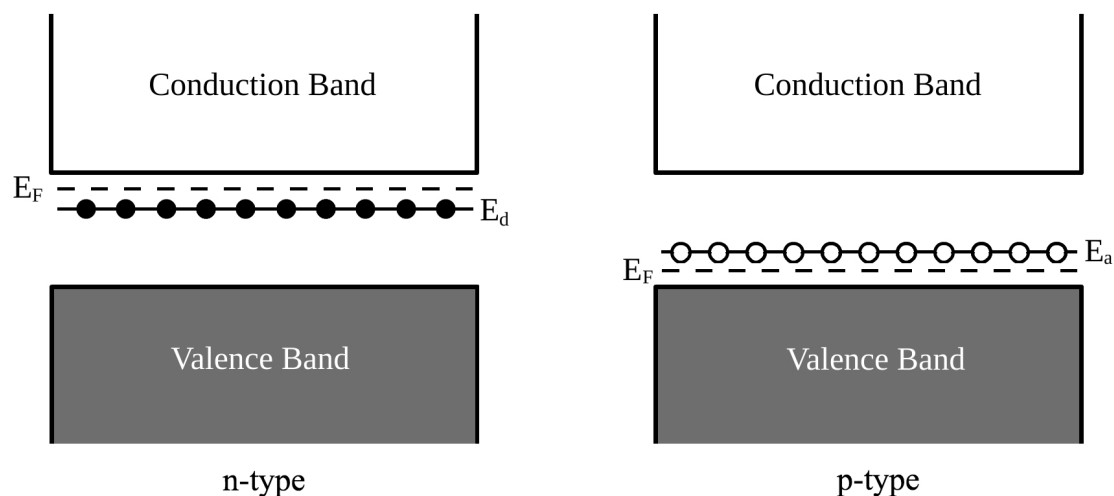


FIGURE 1.9: Energy bands of an n-type and p-type semiconductor. Additional energy levels are added to the band structure by impurity atoms.

p-type doping of diamond is relatively straight forward and can be achieved by substitution of boron atoms into the diamond lattice. Boron has one less valence electron than carbon and thus donates an additional free hole carrier to the lattice, creating an electron acceptor level 0.37 eV above the valence band maximum [64]. Electrons can excite from the valence band into the acceptor level, leaving behind an unfilled band which can electrically conduct. Addition of boron atoms at concentrations of approximately

10^{19} cm^{-3} alters the resistivity of diamond from $10^{16} \Omega \text{ cm}$ to $10^{-1} \Omega \text{ cm}$ [65]. High enough boron concentrations have even been found to give diamond superconducting behaviour [66]. However, at a high concentration of boron incorporation, differences in the atomic radii of carbon and boron have been shown to significantly distort the lattice which affects the quality of the diamond, limiting its use [67]. Boron doped diamond (BDD) with a CH_4/H_2 ratio of 1 % limits the lattice distortions whilst still allowing electrical conductivity at room temperature [68].

n-type diamond doping is significantly more difficult to achieve than p-type doping and is still a highly researched topic for many groups [69]. n-type doping of diamond adds an atom with one valence electron more than carbon (*i.e.* a group V atom) to the diamond lattice. This introduces an extra donor level to the top of band gap as shown in figure 1.9. From a similar explanation to that of p-type doping, it could be assumed that this level would allow electrical conduction by promotion of electrons to the conduction band. However, significant investigations into nitrogen and phosphorus diamond dopants have found that this is not always the case. The donor level of nitrogen in diamond is too deep into the band gap to allow electrical conduction at room temperature. The nitrogen donor level is 1.7 eV below the conduction band minimum and would require an energy much larger than thermal energy at room temperature for electrical excitation and hence conduction [70, 71]. Phosphorus is a better n-type dopant for diamond than nitrogen, with a donor level 0.6 eV beneath the conduction band minimum. From this donor level, a small number of electrons can excite into the conduction band at room temperature to allow conduction. But, phosphorus doping of diamond gives a low carrier mobility and does not give the effective n-type semiconducting properties required for many semiconducting applications [72].

Studies into co-doping (combinations of more than one type of defect) of the diamond lattice have proven better n-type properties than phosphorus alone. By co-doping the CVD diamond with both sulfur and small amounts of boron, significant n-type diamond conduction has been noted by a number of groups [73, 74]. Co-doping of diamond to form an n-type semiconductor has registered its promise, but has not been fully accepted due its complex and unreliable synthesis.

1.2.4 Band Bending

As two materials come into contact, local changes in the energy structure of the interface can be explained by visualising the energy bands bending ³. The concept of band bending was first developed by Schottky and Mott to explain the rectifying effect when

³this does not correspond to any physical bending of the materials

semiconductors and metals contact [73]. These contacts are unavoidable when electrical contacts are made to a semiconducting material in order to measure the electrical properties. As the metal and semiconductor come into contact, any free electrons will transfer between them due to the differences in their work functions. Electrons will flow from the lower work function material to the higher work function material in order to equilibrate the Fermi levels of the two materials. Once at equilibrium, a 'space charge' region will form at the interface due to the differing charge carrier concentrations of the interface and the bulk material. This space charge is a region in the metal to semiconductor junction where there are no mobile charge carriers. The movement of charge carriers justifies whether the type of bending is upwards or downwards, representing differences in the energy levels of the bulk and surface. n-type semiconductors typically have upwards band bending due to electrons transferring from the bulk of a donor atom to the vacant surface states. p-type semiconductors normally have downward band bending due to electron movement from the surface states to the acceptor level of the bulk material.

However, the amount of band bending found at an interface greatly depends on not only the types of material in contact, but also on the terminations of the surfaces, semiconducting doping levels and work functions of the metals used. Understanding this band bending is crucial for all semiconducting devices, as a property which was noted in one environment may significantly change when subject to a different environment. For a betavoltaic device, there are numerous interfaces between differing materials which will need to be fabricated- the most important combinations will be explored below.

1.2.5 Semiconductor Heterojunctions

When semiconductors of different band structures are brought together, their energy bands will bend at the interface due to the lining up of their Fermi levels at equilibrium. The most commonly used semiconducting heterojunction is the p-n junction and is comprised of a p-type and n-type semiconductor in contact. p-n junctions are often considered the 'building blocks' of semiconducting electronic devices, included in diodes, transistors, solar cells and LEDs (light emitting diodes) [75]. Both p-type and n-type semiconductors are relatively conductive separately, but when brought into contact, a momentary flow of electrons from the n-type to the p-type material results in formation of a region depleted of charge carriers. This region is known as the depletion zone and is non-conductive. The reason for this formation in a semiconducting heterojunction is as follows.

Electrons will diffuse from the n-type to the p-type material due to differences in their electron concentrations. As both the n and p-type semiconductors had no net charge at equilibrium, this diffusion of electrons will form an imbalance of charge in the material. The n-type material has lost electrons and will now have an overall positive charge, the p-type material has lost holes (gained electrons) and so will have a negative overall charge. This charge difference across the junction will oppose the initial diffusion and will start to move the electrons back to where they started from. This is known as the electron drift. The opposing movements of charge carriers (diffusion and drift) will form a region where the charge carriers recombine and there is a depletion of carriers- namely, the depletion zone.

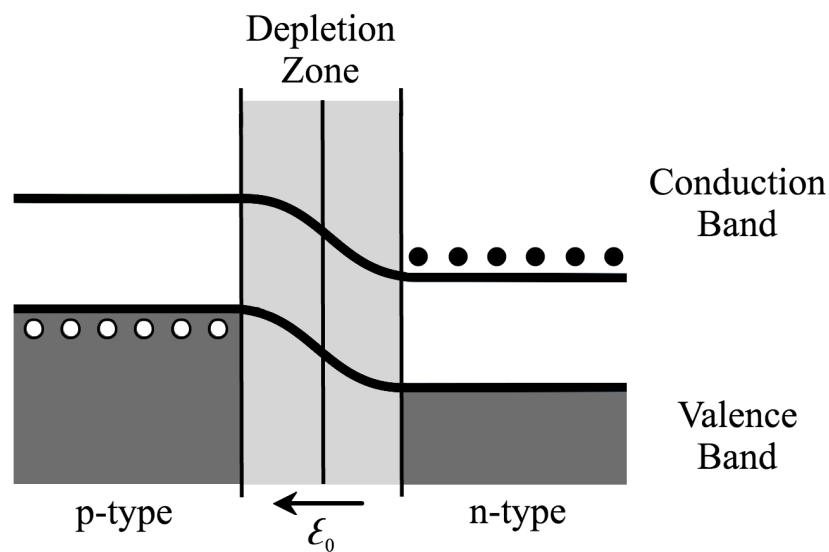


FIGURE 1.10: Cross section of a pn junction at thermal equilibrium with no bias applied. Holes are represented in the p-type side by empty circles and electrons are represented in the n-type side by black (filled) circles. The light grey depletion zone in the centre of the figure represents the region of no charge carriers.

This presence of unbalanced charges across the depletion region will also form an inbuilt electric field (ϵ_0) across the interface. Any remaining electrons in the n-type material will have to move against this electric field to move across the junction. Manipulation of this non-conductive depletion layer by application of a bias across the junction can allow the interface to act as a diode. That is, allowing current to flow in one direction but not in the opposite direction. An unbiased p-n junction is depicted in figure 1.10. By applying a forward bias across the junction, the p-type side is made more positive and so electrons are able to move across the junction and fill vacancies (holes) on the other side. The electric field caused by the applied bias (ϵ_{ext}) will act against the inbuilt electric field and the overall electric field will be reduced. This reduced field will bring the p-n junction to another equilibrium, but this time with a narrower depletion region which can allow additional carriers to cross the depletion zone with a smaller energy

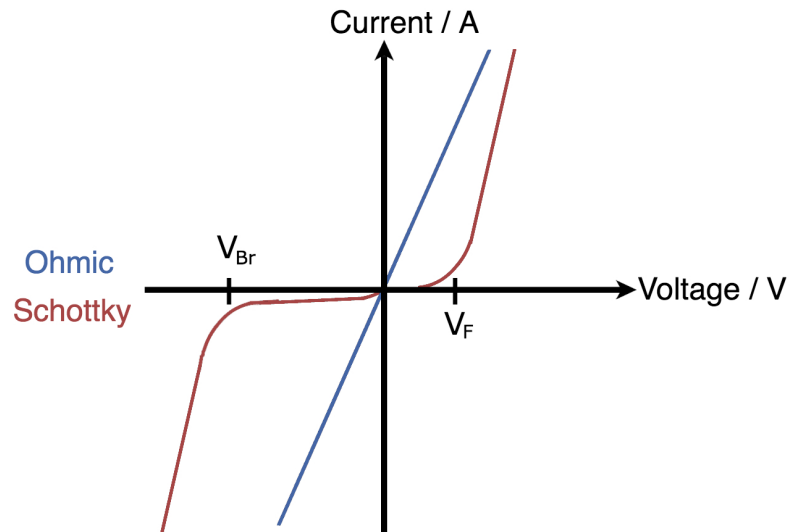


FIGURE 1.12: I/V characteristics for both ohmic (blue) and Schottky (red) metal to semiconductor contacts.

From figure 1.12, the current/voltage plot of an ohmic contact is shown as a straight line passing through the origin with the slope representing the resistance of the contact (from Ohm's law). The Schottky contact shows diodic character, shown by the red curve in figure 1.12. For a Schottky contact in the forward direction (positive voltage), the current rises exponentially with a 'knee' at above the internal barrier voltage (V_F) where the current will increase rapidly over a small increase in voltage. V_F is known as the turn on (or forward) voltage of the diode. For a small reverse bias (negative voltage), the junction will mostly block the current except for a small leakage current due to imperfections in the structure. The reverse direction will show a sharp increase in reverse current flow at a voltage known as the reverse breakdown voltage (V_{Br}). At this point, reverse current travels through the diode and follows a linear path on the current/voltage plot.

For a betavoltaic device to be able to harness energy from the nuclear decay products of a radioactive isotope, a semiconducting diode (either Schottky or p-n junction) is required. However, due to the lack of a convincing n-type dopant for diamond, Schottky diode structure are the most commonly used. Ohmic contacts are also needed in betavoltaic devices as a way of extracting the electrical information from the structure. The incoming beta particle will ideally transfer its energy to the depletion region of the semiconducting diode device where it can be separated by the electric field and collected as a charge by a connected wire. How the final device functions will be largely affected by the interfaces between the materials used in construction and so manipulating these regions is of great importance.

The addition of an intrinsic layer between either the p-n or Schottky junctions increases the distance between the conductive layers, decreasing the capacitance and increasing the

switching speed (rate at which device can provide output in response to input change) of the diode device [76]. This has been extensively researched in p-n junctions to form PIN (p-type-intrinsic-n-type) diodes used in many photovoltaic applications. The added i-layer increases the region for incoming photons to excite electron-hole pairs and consequently increases the overall efficiency of the cell [77]. Similarly, an intrinsic layer provides a larger region for the incoming beta particles to excite electron-hole pairs in betavoltaic devices. The highly doped semiconductors used in these devices are crucial due to their high electrical conductance but have been found to significantly decrease the width of the depletion region. Thus limiting the region for electron-hole excitation. The addition of an intrinsic region counteracts this. An insulating layer between the semiconductor and metal layers in a Schottky diode forms a metal-intrinsic-p-type (MiP) structure. The MiP structure has been recently studied as an alternative to the PIN diode for use with semiconducting materials incapable of forming an n-type form [78]. The Schottky (metal to semiconductor) diode structure has registered its promise for use in diamond energy conversion devices, due to the lack of a convincing n-type dopant for diamond. As both a Schottky diode and ohmic connections are used in the design of betavoltaic devices, their differences will be explained in greater detail below.

1.2.6 Schottky Barrier Height

Whether the metal to semiconductor junction forms an ohmic contact or Schottky diode depends on a critical parameter known as the Schottky barrier height (Φ_B). The Schottky barrier is defined differently for n-type and p-type semiconductors, this is the energy difference between the Fermi level and conduction or valence band edges respectively. This is shown in figure 1.13. For a large Schottky barrier height (significantly larger than thermal energy) the semiconductor will be depleted near the metal junction and will act as a Schottky barrier. For a small Schottky barrier height, the semiconductor will not be depleted and will form an ohmic contact.

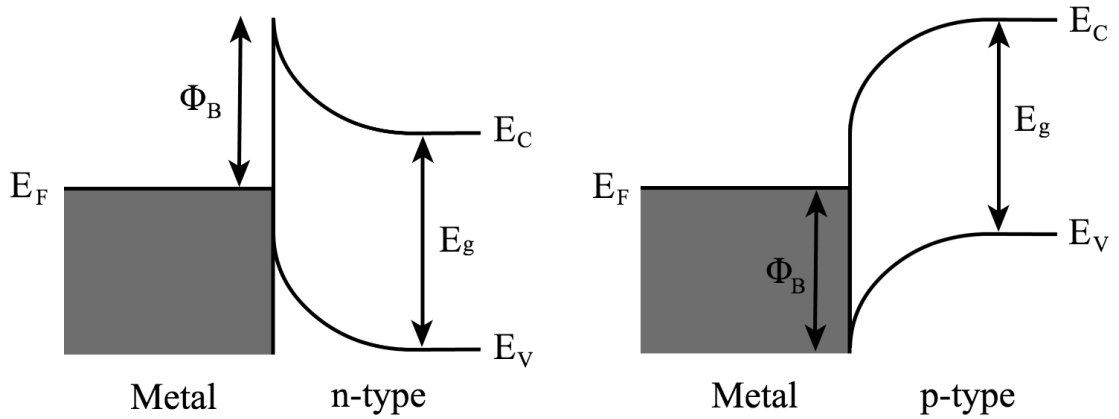


FIGURE 1.13: Band diagrams showing the Schottky barrier height of both n-type and p-type semiconductors. Adapted from reference [79].

The Schottky barrier height was initially predicted using the Schottky-Mott rule, which is calculated from difference in the work function of the metal (Φ_{Metal}) relative to the semiconductor electron affinity ($\chi_{Semiconductor}$):

$$\Phi_B = \Phi_{Metal} - \chi_{Semiconductor}. \quad (1.3)$$

This simple estimation to the barrier height of semiconductor to metal interfaces has been found experimentally to give grossly incorrect predictions [80]. The Schottky-Mott rule predicts some presence of band bending in the semiconductor at an interface, but ignores any changes in this bending due to the chemistry of the metal to semiconductor bonds [81]. Another theory explains a phenomenon called ‘Fermi level pinning’ in which the bands of the semiconductor are already bent before contact (due to the presence of states in the band gap) and the Fermi level becomes locked to one of these states without any influence from the metal. In this case, the Schottky barrier height is approximated to be insensitive to the work function of the metal and is generally assessed as half the band gap of the semiconductor [81]. A similar approximation of the barrier height has been found in the literature which suggests that the barrier height of a strong covalently bonded semiconductor with a large band gap (e.g. diamond) is actually closer to one third of the band gap [82]. Due to the lack of a conclusive approximation to a parameter which is fundamental to the output of the final device, the Schottky barrier heights for metal to semiconductor junctions must be measured experimentally or estimated from previous experimental studies.

1.2.7 Ohmic Contact

Generally, metal contacts to diamond will increase the barrier height due to the wide band gap of diamond. However, by damaging the diamond surface by introducing a carbide interfacial layer before metal evaporation, the barrier height of the metal to diamond interface can be lowered [83]. A non-rectifying ohmic contact on diamond can usually be attained by annealing a carbide forming metal onto a p-type diamond surface. The carbide at the interface creates a defect layer which allows a firm adhesion, critical for ohmic contact fabrication. This also generates gap states which will lower the barrier height [83]. Heavy doping of the diamond contact area decreases the contact resistivity and reduces the depletion width, enhancing carrier transport by quantum tunneling (if depletion region width < 25 nm) [84]. The key requirements for selection of a metal for ohmic contact to diamond are as follows:

1. The metal must be able to form a carbide to create a defect layer.
2. The metal to diamond interface must have a low contact resistivity (this can usually be overcome by heavily doping the diamond surface in the contact region).
3. The contact must form a good mechanical adhesion to the diamond and have a bondable top-layer.
4. The interface must have a high thermal stability in order to remain in contact throughout the annealing process.

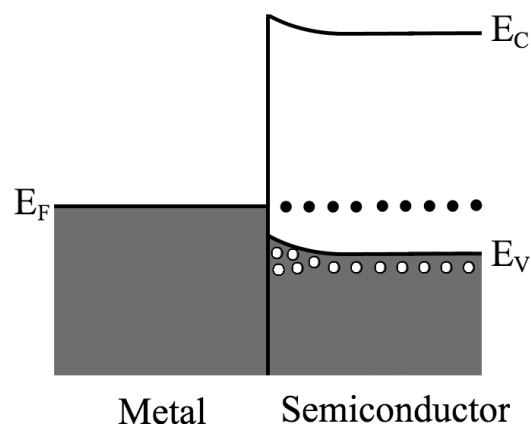


FIGURE 1.14: Metal to p-type semiconductor junction showing an ohmic contact. Redrawn from [79].

The band structure of an ohmic p-type semiconductor to metal junction at thermal equilibrium is shown in figure 1.14. The semiconductor bands bend upwards at the

interface and if biased, the accumulation of holes can flow from the semiconductor to the metal with ease due to the lack of any significant barrier [79]. Ideally, ohmic contacts will have a low resistance and linear current/voltage characteristics.

A common method for forming an ohmic contact to diamond is by annealing a p-type diamond interface covered with a thin layer of titanium (30 nm) and 50 nm gold [85]. Heating the contact at over 750 °C in hydrogen ensures the formation of a titanium carbide interfacial layer and lowers the resistivity of the contacts by several order of magnitude. The titanium provides a good mechanical contact to the p-type diamond by formation of a carbide layer with almost linear I/V characteristics and the gold layer prevents oxidation of the titanium which would degrade the characteristics of the device. The resistance of Ti-Au contacts on heavily boron doped polycrystalline diamond ($>10^{20}$ cm⁻³) has been reported as low as 20 mΩ [79].

As the metals are deposited onto the semiconductor surface, interdiffusion between the metals and the substrate can affect the ohmic behaviour of the contact. Carrier diffusion is increased at grain boundaries between metals and so can be minimised by adding a central metal with an appropriate grain size and inertness to the adjacent materials. Bächli *et al.* discovered that the addition of a ‘tungsten in nitrogen’ layer between the Ti and Au contacts will give stable ohmic contacts without metal interdiffusion and high device working temperatures (1000 °C) [86]. The nitrogen present in this method saturates grain boundaries and ceases the route for interdiffusion. This research found that the use of tungsten in nitrogen between ohmic contacts was more effective at limiting diffusion than the more commonly used Pt and Pd.

1.2.8 Schottky Contact

When a metal to semiconductor interface has a large Schottky barrier, a Schottky contact is formed with rectifying electrical properties. In a Schottky contact, charges will transfer from the higher Fermi level material (p-type semiconductor) to the metal and give rise to a built-in barrier at the interface (Φ_B). This is shown in figure 1.15. To fabricate a Schottky contact, the selected metal to semiconductor interface must have good adhesion, must be stable and must form a large barrier [79]. For a Schottky contact to diamond, the selected metal must not form a carbide layer with the diamond surface as this would increase the number of surface states and render the contact ohmic. Oxygen terminating the diamond surface is the most common method of limiting the density of gap states and providing a Schottky contact to diamond, but this method is known to give an undesired high forward voltage drop in the resulting diode. The O-termination is also found to be

thermally unstable at higher temperatures, which limits the potential functionality of the diode.

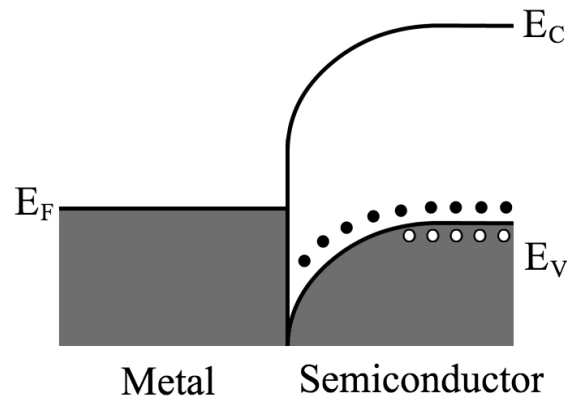


FIGURE 1.15: Metal to p-type semiconductor junction showing a Schottky contact. Redrawn from [79].

An approach was adopted by Traoré which formed a Schottky contact to diamond by using an easily oxidisable metal (zirconium) which could form a thin oxide layer at the interface. This method gave a large barrier height of 1.81-2.29 eV and device rectification up to 773 K [79]. However, the Schottky barrier height decreased at temperatures approaching this value. By annealing the contact at 623 K, the barrier height reduced from 1.88 eV to 1.49 eV and fell below 1 eV at temperatures of 773 K. A recent study has proposed that the Schottky barrier height of many transition metals, as well as aluminium, onto oxygen terminated diamond is approximately the same value (1.4 eV) after annealing at 700 K [87]. This indicates that the barrier height of diamond to these metals is mostly controlled by the electron affinity of the diamond and dipole formation at the interface and not dependant on the metal. Despite this discovery, for lower temperature applications, zirconium contacts onto oxygen terminated diamond have proven a sound method for Schottky diode fabrication. The addition of an aluminium cap on top of the zirconium has also proven to increase the thermal stability of the device whilst also increasing its lifetime by avoiding zirconium oxidation [88].

Teraji and Fiori discovered an alternative method for constructing a Schottky contact to diamond for use in higher temperature applications. They annealed a carbide-preformed metal (tungsten carbide) onto the diamond surface at 600 K [89]. This method limited the carbide formation of the metal onto the diamond as the metal was already in its carbide form. It was found that annealing the metal contact thermally stabilised the interface by the formation of interfacial bonds between the metal and the diamond. The corresponding device showed uniform rectification characteristics up to 800 K.

Similar to how a p-n junction responds under applied bias, a Schottky diode will also give non-linear current characteristics dependant on the inbuilt potential barrier and direction of external bias. Under increasing forward bias, the thickness of the depletion region will decrease to a point where the barrier is close to zero. There, a linear current/voltage regime is established with a resistance corresponding to the materials used in the junction. Under reverse bias, the width of the depletion region will increase due to an increase in the barrier height and the measured current will be minimal. As the reverse bias is further increased, the current measured will also increase at the breakdown voltage of the diode and will follow a linear path as in the forward direction. The band structure of these statements are shown in figure 1.16 and will have electrical characteristics which follow the Schottky diode curve in figure 1.12.

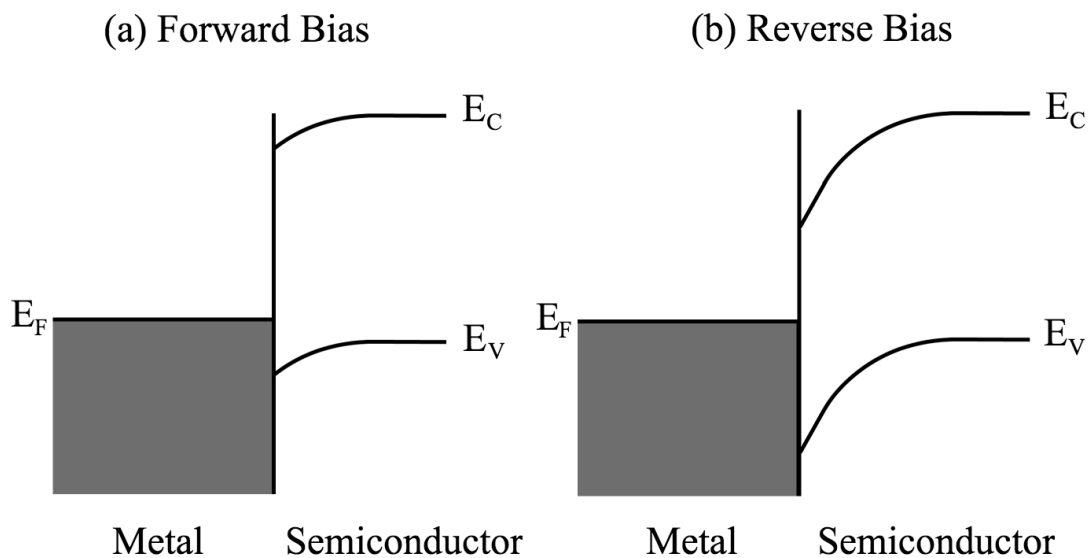


FIGURE 1.16: Metal to p-type semiconductor Schottky junction under both a) forward and b) reverse bias.

Despite showing similar diodic behaviour, Schottky diodes and p-n junctions have a number of differences. Schottky diodes have lower forward voltage drops (voltage needed to push charges through the depletion zone), switching times and due to being a unipolar device (only majority carriers), the reverse leakage current is significantly smaller than in p-n junctions [90]. p-n junctions have a large temperature dependence due to the diffusion of minority carriers across the depletion layer whereas Schottky diodes have a much less pronounced temperature dependence (neglecting any chemical changes at metal interfaces) [91]. Diamond Schottky diodes have the highest voltage breakdown of any Schottky device, but are attributed to larger forward resistance than other materials [92]. This high forward resistance is often due to poor metal contacts or choice of device geometry. In an ideal case, forward resistances of diamond Schottky devices have been

measured as low as $0.01 \Omega \text{ cm}^{-2}$ (in comparison to $30 \Omega \text{ cm}^{-2}$ of Si) but this has not yet been found in a device with a breakdown voltage near the maximum diamond value of 10 kV [93]. The capability of a Schottky diode can be represented by two major factors: the properties of the semiconductor itself and the properties of the metal to semiconductor interface. The blocking voltage will be a property of the semiconductor material whereas the reverse leakage and forward voltage drop will depend on the rectifying effect of the Schottky contacts [79]. A low forward voltage drop, low reverse current leakage and large blocking voltage are the characteristics of most importance to a good overall diode.

1.2.9 Electron Affinity

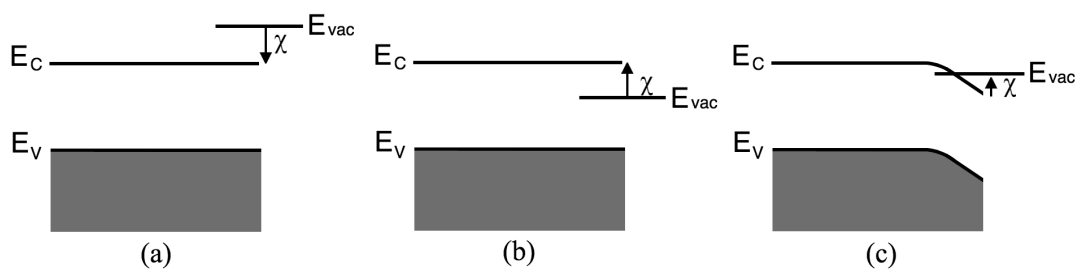


FIGURE 1.17: Energy band diagrams of surfaces shown a) positive electron affinity, b) 'true' negative electron affinity and c) 'effective' negative electron affinity.

Understanding how electrons leave a surface of a material is crucial in understanding how a current is measured from a betavoltaic cell. As previously mentioned, the electron affinity (χ) is the energy difference between the conduction band minimum and the vacuum energy level. Physically, this is the energy required for an electron in the conduction band to escape from the material and into the vacuum. Insulating materials are known to efficiently eject electrons from the conduction band, but, by definition, do not have any electrons in the conduction band to eject [94]. Semiconductors, however, can excite electrons into the conduction band and are therefore ideal for electron emission applications. Figure 1.17a shows the band structure of a semiconductor surface where the energy level of the vacuum is higher than the conduction band minimum, therefore χ is positive and the low energy conduction electrons cannot escape without excitement. This condition is known as a positive electron affinity (PEA) surface and it is this energy barrier which stops electrons in the conduction band from spontaneously leaving the surface. A (true) negative electron affinity (NEA) surface can be seen in figure 1.17b where the conduction band minimum lies above the vacuum energy level. Electrons in a NEA semiconductor can easily diffuse through the surface and into the vacuum, with an excess energy equal to their energy difference [95]. Mearini found that NEA surfaces could be split into two distinct categories: 'true' NEA and 'effective' NEA, with both

categories giving similar electron emission results. Both NEA types have their conduction band minimums above the vacuum energy level in the bulk, but effective NEA surface bands bend at the vacuum to semiconductor interface causing the energy levels to switch their energy order. An effective NEA surface is depicted in figure 1.17c.

Numerous groups have studied the termination of diamond surfaces to show NEA characteristics [96]. Hydrogen terminated diamond has become a standard surface for NEA studies after discovery by Himpsel in 1979 on natural BDD [97]. However, alternatives to H-terminated surfaces have been increasingly researched following the discovery of their upwards band bending on absorption of water. This subsequently degrades the NEA characteristics of H-terminated diamond upon contact with air [98]. The most common alternative to achieve a NEA uses lithium on an oxygen-terminated surface [96].

A negative electron affinity surface is beneficial to a betavoltaic structure as it will minimise the energy wastage of charge carriers on emission from the semiconducting to metal contact. However, providing an adequate Schottky barrier is critical to the final structure and so this requirement must be assessed first. This restricts the terminations available to only those which benefit the Schottky barrier height, dismissing the option of H-terminating the diamond to achieve NEA characteristics.

1.2.10 Mobility

How the charge carriers move through a structure is of major importance to any semiconducting electrical device. For a betavoltaic structure, the way electrons move through the multiple regions must be understood in order to fabricate the most efficient device. Carriers move in a straight line through a material until their path is blocked by a scattering mechanism (normally impurity atoms). Single crystal intrinsic diamond has both the highest electron and hole mobilities of any large band gap semiconductor of $4500 \text{ cm}^2 \text{ V}^{-1} \text{ s}^{-1}$ and $3800 \text{ cm}^2 \text{ V}^{-1} \text{ s}^{-1}$ respectively [99]. However, these carrier mobilities decrease rapidly with increased doping levels and temperature, due to the increased scattering mechanisms. Hole mobilities in single crystal diamond have been shown to decrease to approximately $450 \text{ cm}^2 \text{ V}^{-1} \text{ s}^{-1}$ when boron doped to a concentration of 10^{19} cm^{-3} . For this reason, any electrical device in which the active region is comprised of intrinsic diamond (as in the case for a betavoltaic cell) needs to ensure that the layer remains totally impurity free ⁴. This can be difficult if the device architecture already includes a doped layer as it is well documented in previous literature that impurity atoms can diffuse into intrinsic diamond during the high temperatures present in CVD

⁴the active region is defined as the region in a device in which the charge carriers have to move through

diamond growth [100]. Even boron contamination from the inside of a thoroughly cleaned CVD chamber has been found to dramatically affect the electrical properties of intrinsic diamond growth. This non intentional boron doping of diamond can normally be avoided by either careful consideration of the sequence of device fabrication or can be limited through addition of oxygen to the gas phase reaction [101].

Polycrystalline diamond grown by CVD can still have a high electrical mobility approaching that of single crystal (combined electron-hole mobility of $4000 \text{ cm}^2 \text{ V}^{-1} \text{ s}^{-1}$) for larger grain sizes ($>20 \text{ }\mu\text{m}$) [102]. However, this high mobility greatly reduces to approximately $50 \text{ cm}^2 \text{ V}^{-1} \text{ s}^{-1}$ for grain sizes between $3\text{-}6 \text{ }\mu\text{m}$, showing that the larger grain diamond shows superior electrical properties. The same paper showed a temperature dependence of carrier mobilities in polycrystalline diamond of $T^{-\frac{3}{2}}$, also documenting that the mobility of carriers is limited by phonon scattering. The presence of grain boundaries in polycrystalline diamond is known to increase the density of charge trapping states, which severely hinders carrier lifetimes. It is often difficult to predict the density of defects throughout the growth process due to the constant nucleation of columnar CVD diamond growth and therefore the ever changing grain boundary density [103].

1.2.11 Secondary Electron Emission

In 1902, Austin and Starke found that the number of electrons emitted from a material was greater than the number of incident electrons under certain conditions [104]. This increase in the number of electrons emitted from a solid when bombarded with primary electrons marked the discovery of secondary electron emission- a phenomenon which is still not fully quantitatively understood today. In practice, secondary electrons are defined as electrons emitted from a material with energies below 50 eV. The 50 eV limit is an estimate as there is still no experiment which can distinguish between a secondary electron or a backscattered primary electron, but the number of higher energy secondary electrons and the number of lower energy backscattered electrons is considered minimal and so this value proves an accurate limit [105].

A betavoltaic device works by converting an electron emitted from a radioisotope into a current collected through a semiconducting device. If the number of collected electrons could be made larger than the number of incoming electrons, then the output power of the device could be increased and hence could increase the range of potential device applications. Enhancing this current is of major significance to the output energy production of the betavoltaic cell and so careful device design must be explored to utilise this characteristic.

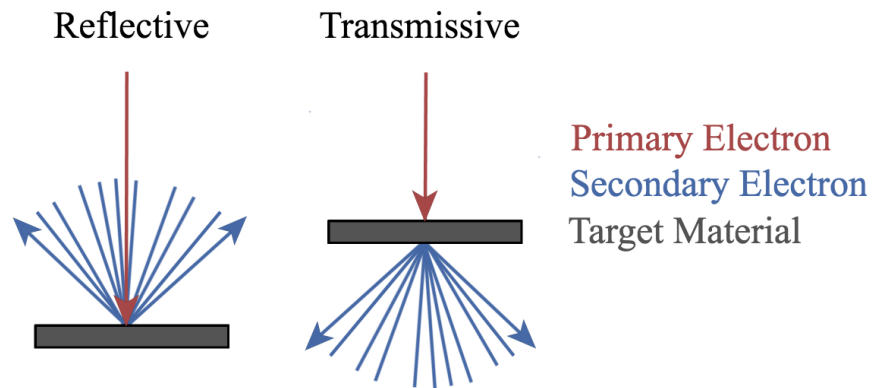


FIGURE 1.18: Secondary electron emission of both reflective and transmissive structures.

The two geometries important in the understanding of secondary electron emission are reflective and transmissive. Their different architectures are shown in figure 1.18. As a beam of incident electrons is accelerated into a material, the electrons can interact with the solid in a number of different ways, all resulting in the emission of electrons. The primary electron may be backscattered, either elastically or inelastically, or result in ‘true’ secondary electron emission which can be described by three distinct steps [94]:

1. The production of internal secondary electrons by kinetic impact of incident electrons.
2. Transport of the secondary electrons through the sample bulk and to the surface.
3. Escape of the secondary electrons through the solid to vacuum interface.

A fraction of the incoming electrons will be backscattered at the surface and will not contribute to the number of generated secondaries in the material. The low atomic number of carbon minimises this backscattering to a few percent which is considerably lower than that of other wide band gap semiconductors [106]. If not backscattered, the primary electrons can penetrate the material and collide with electrons in the bulk where they slow down and transfer their kinetic energy to generate internal secondary electrons in the material. If the energy transferred by the incident electron is greater than the band gap, a secondary electron can be excited from the valence to the conduction band, leaving a positively charged hole in the valence band. This forms an electron-hole pair (exciton) in the material, attracted to each other by an electrostatic interaction. The electron in the conduction band could fall back into the valence band, re-coupling with the positive hole (exciton decay). Alternatively, the electrons could move from the conduction band into the vacuum (exciton dissociation). In this case, the polar exciton is attracted to

the dipole at the surface to vacuum interface and when the exciton reaches the surface, the strong exciton-lattice coupling breaks and releases the electron into the vacuum as a secondary electron [107]. As the internal secondary electrons move through the solid, they can collide with other bulk electrons resulting in multiple electron-hole pairs piled up in the conduction band [108]. If the material has NEA characteristics, the electrons in the conduction band will easily escape into the vacuum as emitted secondaries.

The ratio of the intensities of total emitted secondary electrons (I_t) from a surface to the intensity of incident electrons (I_0) on that surface can be simply described as the secondary electron yield (SEY). This is shown as

$$\delta = \frac{I_t}{I_0}, \quad (1.4)$$

where δ is the SEY. For a reflective structure, the secondary electron yield will be noted as RSEY and can be calculated at varying primary electron energies to analyse the emission properties of a material. The bell-shaped curve shown in figure 1.19 is a typical result for this method.

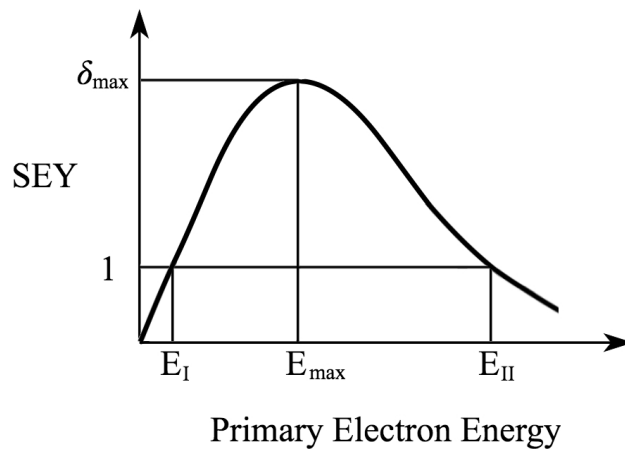


FIGURE 1.19: Variation of secondary electron yield with primary electron beam energy. Design from [9].

Calculation of three parameters from the curve gives fundamental information about the charge transport properties of the solid. There are two energies, E_I and E_{II} , at which the SEY is unity, and a maximum yield (δ_{max}) at a corresponding energy, E_{max} . These parameters can be used to deduce the penetration depth of the incident electrons and the escape depth of the internal secondaries.

For $E < E_I$, the SEY increases with increasing primary electron energy, but is below one, as the primary electron is not energetic enough to penetrate the surface and reflect

back. At $\delta=1$, the net current of the material is zero [109]. For $E_I < E < E_{\max}$, the SEY increases with increasing incident energy due to the fact that the penetration depth of the primary electrons is smaller than the escape depth of the secondary electrons. The depth of penetration of primary electrons and hence the depth at which the secondaries are generated, increases proportionally with the incident energy. At the maximum SEY, the penetration depth and escape depth are equal. Above E_{\max} , the secondary electrons are generated at a point so deep into the material that most electrons lose their energy before reaching the surface. For $E < E_{\max}$, the penetration depth of primary electrons is the controlling factor of the SEY and for $E > E_{\max}$, the escape depth of the secondaries dominates.

Diamond has regularly shown excellent electron emission properties accredited to its large electron escape depth (tens of nm for 1 keV primary energy) and ability to offer a NEA surfaces [110]. High emission yields are regularly reported for H-terminated boron doped diamond with variations dependant on the morphology and orientation of the surface, together with the surface termination and doping levels. Yater *et al.* documented the RSEY of diamond increasing from 3 to over 100 by changing the crystallographic orientation and termination of the surfaces [111]. Another study documented the RSEY of single crystal diamond at 3 keV to be 80, which reduced to 10 for polycrystalline films [110]. Although the SEY is not directly dependant on the electrical conductivity of the sample, the literature values quoted have all boron doped the diamond to allow the necessary conductivity to prevent charging of the sample by balancing the electron flow [112]. They also utilise H-terminated surfaces to include NEA characteristics so that the maximum number of generated secondaries can be collected.

As the boron doping level of diamond initially increases, the SEY also increases. However, after an optimum boron doping level is reached, any additional doping will reduce the yield due to the extra impurity atoms increasing the number of electron scattering sites. The SEY of boron doped diamond has been calculated to be maximum at boron concentrations of approximately 10^{19} cm^{-3} [95].

Reflection secondary emission structures typically give higher yields than transmissive structures, but the devices fabricated often have a shorter lifetime caused by deterioration of the structure due to radiation damage from the high currents passing through it [113]. Over time, constant electron bombardment of a NEA surface will degrade its characteristics and the device efficiency will dramatically decrease. Transmissive structures have an increased lifetime due to the negative electron affinity surface being on an opposite face to the incoming electrons, limiting wear of the NEA surface. However, generated secondaries may emit from the penetrative surface and not contribute to the TSEY.

Using different functionalisations on the top and bottom surfaces of the structure can limit this [110].

For transmissive devices, the yield calculation is altered slightly and is calculated as the intensity ratio of secondary electrons transmitted through the material per incident electron intensity on the penetrative surface. This will be documented as TSEY. Transmission electron emission yields of polycrystalline diamond are found to be 1-4 using high energy primary electrons of 20-25 keV [114]. The main cause for this low value is due to the low transport efficiencies and increased scattering of electrons encountered on passing through a material. Single crystal diamond has a larger diffusion length than polycrystalline diamond and so gives greater yields for given device thicknesses. Although better, the TSEY of single crystal diamond is still no greater than 5 [9]. Using isotopically pure methane (less than 1 part per billion impurities) to grow the diamond would increase the yield due to a lower density of scattering sites. The corresponding penetration and escape depths of isotopically pure diamond are also established to be higher than the natural isotopic mixture of C-12 and C-13 [115].

The thickness of the transmissive device used must be considered to maximise its secondary yield. If the device is too thick, for a given primary electron energy, then no secondary electrons will make it through the sample and the yield will be low. If the device is too thin, then the primary electrons will pass straight through the structure with excess energy not employed to generate a higher number of secondaries- not utilising the benefits of the electron gain device. Diamond device thicknesses often need to be less than a micron (dependant on the primary electron energy) in order for the low energy secondary electrons to emit from the material [9]. This increases the difficulty of device fabrication, as growing thin diamond films has been proven difficult due to poor substrate seeding giving intermittent diamond coverages. Using structures with an inbuilt electric field, or applying a bias, can help to ‘pull’ the generated secondaries through the material and allow for thicker structures. The desired thickness of the device can be approximated by calculating the penetration depths of electrons in diamond- this can be done using the Kanaya and Okayama equation [116]:

$$R = \frac{0.0276AE_p^{1.67}}{Z^{0.889}\rho}, \quad (1.5)$$

where for diamond, $A=12$, $Z=6$ and $\rho=3.513 \text{ g cm}^{-3}$ [117]. The primary electron energy (E_p) is in keV and the penetration depth (R) is given in microns using the scaling factor of 0.0276. Using this relationship, an electron with a considerable energy of 15 keV will only penetrate 2 μm into diamond.

Similar to in reflection mode, the morphology of the surface will affect the penetration depth of incoming electrons. For polycrystalline diamond, the energies of the secondary electrons will typically be eV and so for secondaries with an energy less than the band gap, the escape depth is very low due to scattering from phonons and impurity atoms [118]. If the incoming electron generates a secondary electron at a region in the material where there is a high density of grain boundaries (e.g. nucleation layers), the secondary electrons will lose all of their energy quickly and will remain trapped in the material very close to their region of generation. Secondary electrons generated away from this nucleation layer will have a much greater chance of successfully moving through the film and being emitted from the surface. If a generated secondary electron has sufficient energy (larger than the band gap), then it may be able to escape from deeper within the bulk due to the absence of collisions with valence electrons.

As the grain sizes and quality of CVD diamond increases with growth duration, the quality of the crystal will change throughout the transport region of a material. This difference must be considered when looking at the TSEY of a material. For electrons penetrating through the nucleation side of a sample, the deeper they make their way into the material, the higher the quality of the material they will generate secondaries into. This will increase the chances of secondary electron emission due to both the lower density of grain boundaries (trapping sites) and a shorter distance from the emitting surface.

If an incoming electron has to penetrate through a metal to reach the diamond structure, then the metal coating will capture a proportion of the primary electron's energy. The amount of energy lost in the metal contacts will vary dependant on the metal used and its thickness. For a common ohmic contact to diamond (30 nm Ti/50 nm Au), the energy lost is approximately 3.3 keV and only the remaining electron energy will contribute to the secondary electron generation [85]. The energy to create an electron-hole pair (E_{e-h}) in diamond is fixed and can be calculated using the following equation:

$$E_{e-h} = \frac{E_p - E_{lost}}{\delta_{max}}, \quad (1.6)$$

where E_p is the primary electron energy and E_{lost} is the energy lost in travelling through the electrode. The exciton generation energy in polycrystalline diamond has been experimentally recorded as 19.82 eV, higher than the theoretical value of 14.66 eV [85]. Variations in these values can be attributed to both experimental unknowns at the metal to semiconductor interfaces and limitations in the ability of the simulation to predict scattering mechanisms [119].

1.3 Batteries

1.3.1 History

Sony commercialised the first Li-ion battery in 1991 which has become the fastest growing battery type on the market and can now store charges of approximately 1 A h cm^{-3} [120]. With current technologies, this value seems unlikely to be surpassed. On the negative side, lithium based batteries have a relatively short life span and the electronics market is continually requesting smaller and longer lifetime battery devices. A possible alternative to lithium ion cells are nuclear batteries, which convert the nuclear decay products of radioactive isotopes into electricity. The first nuclear cell was introduced in 1913 when Henry Moseley demonstrated that using high positive voltages to pull beta particles from a radioactive radium source, generated a current [121]. Nuclear batteries provide a reliable alternative to chemical batteries for use in low power electronics, boasting a long lifetime and reduced size. They can allow long term energy production in the harshest of environments where minimal maintenance is crucial- namely, in space exploration and cardiac pacemakers where battery re-charging is not a viable option.

1.3.2 Nuclear Batteries

Similar to nuclear reactors, nuclear batteries harness the energy from radioactive decay products to generate electricity. However, where nuclear reactors would use chain reactions to provide energy, nuclear batteries continually harness energy from constant radioactive emissions [122]. Nuclear batteries have energy densities up to five orders of magnitude higher than chemical batteries and can operate over a wider range of environments without the need for recharging. Despite these positive characteristics, nuclear batteries commonly have a lower power density and conversion efficiency than today's chemical batteries. They also pose difficulties with usage due to the strict regulations imposed on their disposal and are impractical to work with. Nuclear batteries are not planned to replace the need for chemical batteries in the near future, but have certain characteristics which make them a considerable alternative for certain applications (e.g. those which request long timescales or high energy densities). The attributes of popular energy storage methods are shown in figure 1.20.

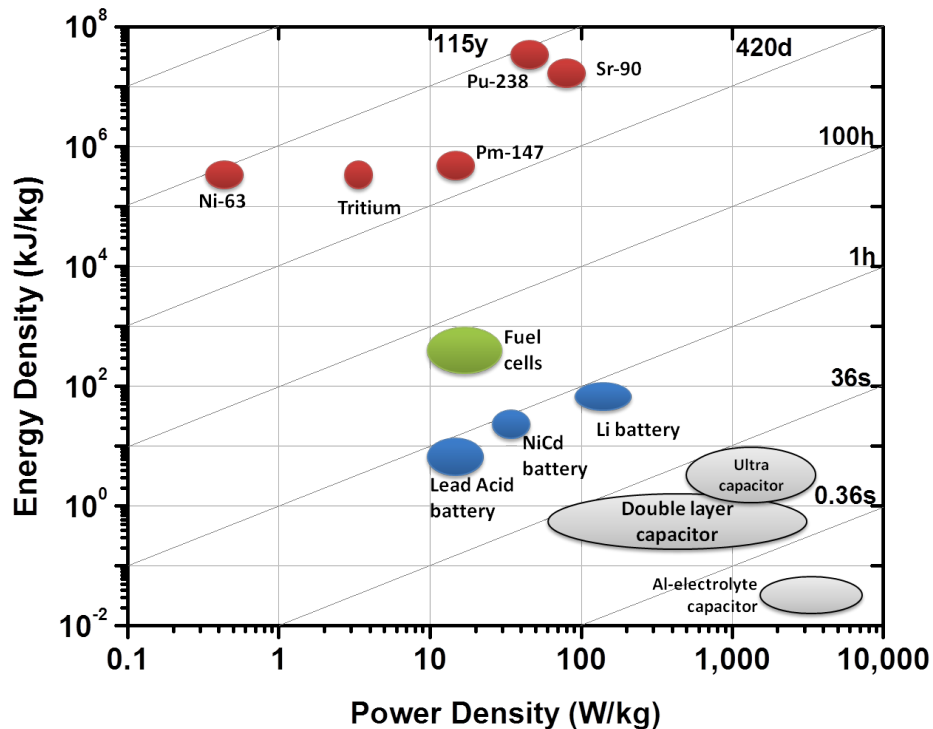


FIGURE 1.20: Ragone plot of capacitors (grey), chemical batteries (blue), fuel cell (green) and atomic batteries of popular isotopes (red). Sloped lines show constant time. Figure from [122].

From figure 1.20, chemical batteries and fuel cells can store moderate energy and power densities and discharge over a timeframe of hours. These properties are those which the majority of everyday electrical items need. Capacitors have high power densities, which chemical batteries can currently not compete with, but release this power over shorter timeframes (seconds) and can only cater for applications which can harness this. Nuclear batteries occupy a completely different region of the Ragone plot (figure 1.20) than the aforementioned, featuring a considerably larger energy density at a similar power density (for certain sources) and a much higher working time frame of hundreds of years. Both types of energy storage devices (low energy density over short timescales and high energy density over long periods) have vastly different properties despite effectively providing the same service. Consequently, they are to be used for very different applications. The workings of nuclear batteries will be further explored below.

1.3.3 Energy Conversion Techniques

The energy conversion techniques of nuclear batteries can either be thermal (where the output power is a function of a temperature differential) or non-thermal (where the

output power is independent of a temperature differential). Thermal energy converters generate electricity from the thermal energy of a radioisotope under decay. They can produce high kW of power but require large amounts of radioactive material to complete this [123]. More than a gram of radioactive isotope is currently needed to create a thermal gradient sufficient for thermal energy conversion in this power range.

Non-thermal converters can be further split into three sectors- direct charge, direct conversion or indirect conversion batteries. Direct charge cells use the charges of emitted particles to directly drive a current in a device when collected across an air gap. The low currents and high voltages found in these devices have limited their potential applications [124]. Indirect conversion batteries involve multiple steps of energy conversion. Typically, the emitted particles from the radioactive source will strike a radio luminescent material (phosphor) to produce photons which can then be collected by photodiodes. The low efficiencies (2 %) and fast degradation of the luminescent material with incoming high energy radiation, have also limited the use of these devices [125].

Direct conversion batteries convert the radioactive decay products directly into electricity- either utilising the voltaic effect, a contact potential difference or secondary emission from an irradiated surface. Secondary emission cells are a variant of direct charge cells which use the generation of secondary electrons in a dielectric material to increase the current collected from the device [126]. By placing a thin dielectric between the electrodes of a direct charge cell, secondary electrons can be generated across the gap enhancing the collected current. Although no working secondary emission cells have been fabricated to date, a number of theoretical studies have been conducted. Secondary emission cells are predicted to have low efficiencies of between 0.5-1 % due to the low energy secondary electrons being stopped in the thick insulating region before ever reaching the collector [127]. The insulator thickness cannot be reduced to overcome this, as it is needed to initially scatter the primary electrons in order to produce the secondaries.

Contact potential difference batteries work by generating electron-hole pairs in a material on impact of a radioactive decay particle. The generated electron and hole migrate and are held at opposite ends of the cell (due to differences in the work functions of the metals). Here they can supply a current to a connected external load [128]. Contact potential batteries have low efficiencies and currents of 1 % and nA respectively and hence have had a limited amount of associated usage.

The final direct conversion device is a voltaic cell which works by converting radioisotopic decay products (alpha or beta particles) into electricity using a semiconducting junction. The theory behind this device works with a principle similar to photovoltaic cells. However, instead of photons penetrating the material to generate excitons, this excitation is conducted by an alpha or beta particle. The incoming particles are typically high

energy which allows thousands of electron-hole pairs to be produced in the semiconductor per incident particle. These can be swept across the device by the inbuilt field and collected as a current [129]. Single voltaic cells have been constructed with efficiencies of 10 % and are likely to increase in efficiency with improved device modifications. Voltaic cells have a considerably higher efficiency than the other energy conversion techniques mentioned and have proved to be a strong competitor for applications where chemical batteries are ineffective.

1.3.4 Betavoltaic Batteries

Betavoltaic batteries use the beta particles emitted from a radioactive source to generate an electric current across a semiconducting diode junction. As the high energy beta particles penetrate the semiconducting bulk material, they have the ability to generate a large number of electron-hole pairs per incident particle. The electron-hole pairs generated at the depletion region in the semiconducting material will be separated by the internal electric field and collected as current at the contact terminals of the device. A simplified schematic of a betavoltaic battery device is shown in figure 1.21

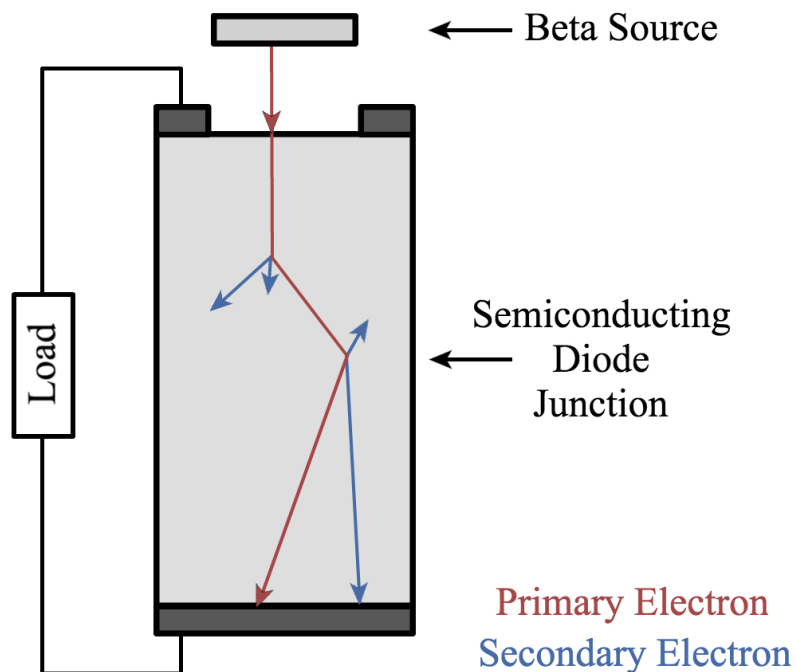


FIGURE 1.21: Schematic of how a betavoltaic device converts beta particles emitted from a radiation source into current across a semiconducting diode.

Betavoltaic batteries were initially proposed as long-term medical devices in the 1970s when researchers developed a working battery using Si and a Pm-147 source. This

battery had a conversion efficiency of 4 % and a 10 year lifetime and was implanted into the pacemakers of 285 test patients [130]. However, the high costs of manufacturing and concerns over emission of harmful gamma rays halted further exploration in this area. Researchers since then have a far greater understanding about the workings of betavoltaic batteries but despite this increased proficiency, the overall efficiency of the cells still remains low (less than 10 %). Nevertheless, a number of corporations are continuing to research and manufacture betavoltaic cells in attempt to increase this. In 2008, an American company, City Labs, produced a tritium betavoltaic cell with the highest power density of any betavoltaic battery and a 7.5 % efficiency [131]. This City Labs NanoTritium™ battery also satisfies all nuclear regulatory guidelines and is able to be sold within the United States, proving that there is a potential market for these devices. The principal obstacle in betavoltaic battery development is undoubtedly the low device efficiency and overcoming this may drastically increase their popularity.

The key to any feasible radioisotope battery is for an efficient conversion mechanism between nuclear and electrical energy. Previous studies have shown that wide band gap semiconducting materials can greatly improve the internal efficiency of betavoltaic devices by increasing the open circuit voltage and radiation resistance [33, 125, 132]. It has also been found that a wide depletion region assists in collecting a maximum number of electron-hole pairs generated by the incoming radiation, increasing the power output of the device [133]. Although Si p-n junctions are the most commonly used device for the conversion of radiational decay into electrical power in the betavoltaic method, an array of different semiconducting materials and architectures have recently been explored. Batteries using Si, SiC and GaN with both Schottky and p-n rectifying junctions have been tested with a Ni-63 radioactive source and have given power conversion efficiencies of approximately 5 % and open circuit voltages of 1.5 V [131, 134, 135].

1.3.5 Efficiency

The efficiency of a betavoltaic battery is calculated as the product of the source efficiency (η_b), the coupling efficiency (η_c) and the internal efficiency of the semiconductor (η_s) [136]. The source efficiency is related to the fraction of energy impinging on the semiconductor and the coupling efficiency is related to the efficiency of the structure to collect beta particles. The source efficiency is dependant solely on the radioisotope used and the efficiencies of the semiconductor and the coupling are shown by the following two equations:

$$\eta_s = \frac{qV_{OC}FF}{\varepsilon}, \quad (1.7)$$

$$\eta_c = (1 - r)Q, \quad (1.8)$$

where q is the elementary charge, V_{OC} is the open circuit voltage and ε is the ionization energy of the material. FF is the fill factor parameter which evaluates the overall performance of the cell, r is the reflection coefficient of the primary beta particles from the device surface and Q is the charge collection efficiency (CCE) of the semiconductor. The CCE is defined as the ratio of the charge induced on the contacts to the total free charge created by the ionization.

The CCE of today's betavoltaic batteries is approaching 100 % suggesting that it is the open circuit voltage which must be increased to improve the overall cell efficiency. This can be increased by using large band gap materials but also by lowering the barrier height of the metal to diamond ohmic contacts [135]. Minimising the recombination rate of carriers will also increase the open circuit voltage. Using a lighter metal as the ohmic contact material could also reduce the energy loss of electrons passing through it to increase the output voltage.

Over the last decade, a number of numerical simulations have allowed further exploration into the most efficient design of betavoltaic batteries [137]. A paper detailing a model based on Monte Carlo and Silvaco simulations of a GaN construction with Ni-63 energy source has enhanced the understanding of electron-hole pair generation and the carrier collection mechanism in the cell structure [138]. The results were verified by comparison with experimental testing under scanning electron microscope radiance. Monte Carlo simulations can also provide information on the backscattering of electrons at a surface, secondary electron yield and the penetration and escape depths of electrons. These characteristics are of huge importance to creating an efficient betavoltaic device and simulations provide a rapid way of analysing device design.

1.3.6 Diamond Betavoltaic Batteries

Although investigations into using diamond as the betavoltaic battery material are not as abundant as the aforementioned materials, many beneficial characteristics for efficient nuclear to electrical energy conversion are noticed in diamond. The intrinsic properties of Si, GaN, 4H-SiC and CVD diamond are compared in table 1.3 ⁵.

⁵4H is the polytype of SiC with the highest mobility and is considered best suited for betavoltaic applications

TABLE 1.3: Properties of potential semiconducting materials for betavoltaic device fabrication [99].

	Si	4H-SiC	GaN	CVD Diamond
Band Gap (eV)	1.1	3.2	3.44	5.47
Breakdown Field (MV cm ⁻¹)	0.3	3	5	10
Electron Mobility (cm ² V ⁻¹ s ⁻¹)	1450	900	440	4500
Hole Mobility (cm ² V ⁻¹ s ⁻¹)	480	120	200	3800
Electron Saturation Velocity (×10 ⁷ cm s ⁻¹)	0.86	3	2.5	2
Hole Saturation Velocity (×10 ⁷ cm s ⁻¹)	n/a	n/a	n/a	0.8
Thermal Conductivity (W cm ⁻¹ K ⁻¹)	1.5	5	1.3	24

From the findings shown in table 1.3, it can be seen that diamond shows significant potential for use as a betavoltaic battery. Diamond (carbon) has a low atomic number implying low electron backscattering and bremsstrahlung radiation, it also has a high stopping power due to its high electron density allowing for thinner layered final structures. Diamond has a remarkable radiation hardness and large carrier diffusion lengths admitting a lower recombination rate and hence higher CCE [106, 139]. However, diamond's use as the semiconducting material in betavoltaic batteries also has a number of challenges. As diamond does not have an effective n-type dopant, diamond devices need to be designed so that holes are the only available charge carrier [99]. Brezeanu and co workers compensated for this difficulty by utilising the exceptionally high hole mobility of intrinsic diamond and a metal-intrinsic-semiconductor (MiP) unipolar device to prove that diamond is a substantial candidate for use in power electronics [140].

A single crystal (MiP) diamond membrane was tested as a betavoltaic battery using an electron beam induced current (EBIC) by Pomorski *et al.* [106]. Pomorski reported a high open circuit voltage of 1.85 V and an energy conversion efficiency of 9.4 % across a 1 mm² active area. Although the EBIC method is useful for characterisation, simulating beta emission using a diffused electron beam from a scanning electron microscope (SEM) does not give an accurate representation of the wider range of energies and angles seen to be emitted from a beta source. Pomorki's group used simulations from the *CASINO* software to calculate the amount of backscattered electrons and exciton recombination rate in the

p-doped diamond layer. Their resulting efficiency and open circuit voltage are significantly higher than other groups, but the area of the cell was limited to 1 mm². It has been previously discovered that the effectiveness of Schottky diodes significantly decreases with increasing device area due to inconsistencies across larger diamond substrates. Consequently, Pomorski's quoted efficiency is likely to decrease on increasing device size [141].

Bormashov and his group used a different technique to make a betavoltaic battery by combining 130 single crystal CVD cells into a battery structure. The resulting device was then characterized with several beta sources (Ni-63, Pm-147 and Sr-90/Y-90) and an SEM with 20 keV beam. A maximum conversion efficiency of 4-6 % and open circuit voltage of 0.8 V was reported [142]. Using the *CASINO* software to simulate the power deposition of beta particles emitted from Ni-63 in diamond, Bormashov et al. found that the maximum power deposition of the particles would take place at the surface of the cell, exponentially decreasing with depth into the surface. The MiP diode structure used by Bormashov complemented this finding as the depletion region of the fabricated structure is very close to the surface of the device, allowing for secondary electrons to be generated whilst the energy of the incoming particles is highest. The intrinsic diamond layer included in the chosen structure also provided a larger depletion region for electron-hole excitations and hence a higher potential output.

1.3.7 Beta Source

Despite the importance of the semiconducting device, selection of a beta source also needs careful consideration. The decay isotope, average energy, half life and the effects of radiation damage on the semiconducting device need to be reviewed. In order to increase the power output of the betavoltaic cell, a radioisotope with high specific power should be selected. To fabricate long life devices, a source with a long half life should be selected. The specific power is proportional to the average energy of emitted beta particles but inversely proportional to the half life of the material and so a balance between the device lifetime and energy required needs to be selected for the individual application of each device. The energy of the emitted beta particles must also be smaller than the radiation damage threshold of the semiconductor, to avoid device degradation, but also large enough to generate multiple excitons in the intrinsic region of the structure.

TABLE 1.4: Properties of potential beta emitting radioisotopes. Y-90 is shown in the same row as Sr-90 due to being its radioactive daughter isotope. All other daughters are non-radioactive [33].

Source	Half-life	Av. Energy (keV)	Max. Energy (keV)	Av. Specific Power (mW g ⁻¹)
H-3	12.32 y	5.69	18.59	324.914
Ni-63	100.2 y	17.42	66.94	5.796
Pm-147	2.62 y	61.93	224.6	340.367
Sr-90	28.79 y	195.8	546	160.238
Y-90	64 h	933.6	2280.1	3.011×10^6
C-14	5700 y	49.47	156.475	1.313

A comparison of some popular radioisotope sources are shown in table 1.4. Ni-63 is the most commonly used radioisotope for betavoltaic battery design. It is a pure beta emitter, with a long half life (approximately 100 years) and maximum energy well below the radiation damage limit of diamond [143]. But, Ni-63 has very low specific power of 5.8 mW g⁻¹, due to the long half life and low beta energy, and so is only suitable as a power source for the nano-microwatt range [33]. Ni-63 is easy to handle as it has a solid metal form and low energy emission spectrum and can easily be electroplated into the battery structure, making it a popular choice for low power applications [144].

All radioisotopes will show a certain amount of self absorbance of beta particles which is dependant on the dimensions of the source used [33]. The apparent (measured) activity of a source will always be less than its actual activity and so it is the measured value which will benefit to the energy conversion of the betavoltaic cell. The self absorbance of the source can be minimised by calculating and slicing the optimal thickness of active material. Research into using either gaseous or liquid beta emitters has been investigated, resulting in an improved specific power output [145, 146]. Using a fluid state radioisotope makes filling the maximum surface area of the structure much simpler with minimal self absorbance, but increases the likelihood of radioactive contamination and so is rarely used for device testing [147].

1.4 Aims of the Research

The main proposal for this project is to construct and characterise a CVD grown diamond betavoltaic battery device. Understanding the behaviour of each of the material interfaces in the device is of as much importance to the final results as the manufacturing process and so the device design must play a considerable part in the research. Substantial

literature is available on the individual junctions required to construct the diamond betavoltaic device. This project aims to incorporate many of these previous findings into a testable battery. The sequencing of each of the manufacturing operations must be clearly considered so as not to impair any of the previously constructed layers when adding a new component. The final battery structures will be constructed with homologous materials but with varying i-diamond thicknesses in order to assess how this affects the final energy output.

The resulting betavoltaic devices can be tested using an array of techniques after each deposition stage to study how any small discrepancies across the samples may result in major differences in the final outputs. Computational simulations are also conducted to provide information about features of the device which are unable to be recorded experimentally. Finally, the electrical output of the structures must be analysed under normal room conditions to assess the prospect of the devices use as a standalone betavoltaic battery.

The benefits of using diamond within the device are primarily due to its large band gap and high intrinsic carrier mobility. A number of groups have previously proven the capabilities of using diamond in betavoltaic devices, however, little work has been conducted using polycrystalline diamond or over larger active areas (cm^2). This project aims to attempt exactly this. If an efficient device could be manufactured using CVD grown polycrystalline diamond, then perhaps this could spur further research into the use of this low cost and CVD grown material for electrical applications. As we develop a greater understanding of how polycrystalline diamond functions in electrical applications, the overall efficiencies of the devices are sure to follow. A similar increase in the amount of research into the use of polycrystalline silicon in photovoltaic applications resulted in a greatly increased device efficiency [148]. Polycrystalline diamond use for betavoltaic batteries aims to mimic this gain in device efficiency.

Energy storage is clearly a problem in today's society and so developing an effective alternative to the relatively short term energy discharge of current battery technologies is of major importance. Both smaller and longer lifetime batteries are also increasingly required to assist with the rapid developments and expanding capabilities of nanoelectronic devices. The current use of lithium ion batteries can no longer cater for these applications and a new generation of power sources is required for nanoelectronic developments to progress [149]. Betavoltaic batteries could assist in this ongoing product evolution.

Chapter 2

Experimental Method

The experimental research conducted throughout this project can be split into four main sections:

- Design and growth of the diamond films
- Diamond quality checks
- Metal deposition
- Electrical testing of the device, both in and out of beta radiation.

The methods and apparatus utilised throughout the experimental section will be ‘as standard’ apart from where clearly stated to be otherwise. The diamond used in this research will be entirely grown in the University of Bristol Diamond Laboratory (S111) and will utilise the MiP architecture with its proven ability for diamond betavoltaic applications. All layers and contacts other than the thickness of the i-diamond layer will be retained for ease of comparison between devices. A diagram of the MiP structure is shown in figure 2.1.

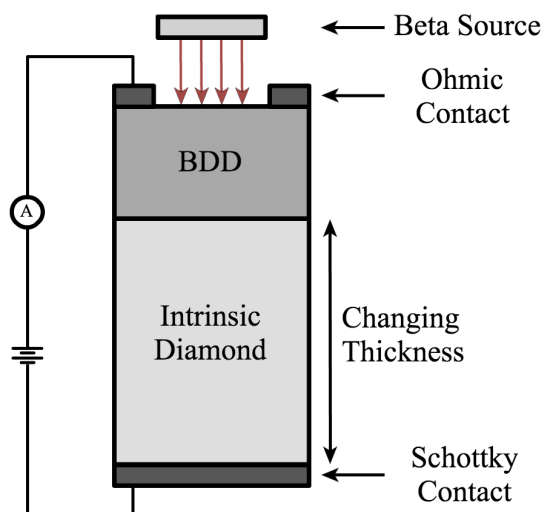


FIGURE 2.1: Cross section of the MiP diode used as the betavoltaic device architecture.

2.1 Diamond Growth

The chosen structure is comprised of a p-type diamond penetration layer, large intrinsic region and Schottky metal back contact. The substrate chosen for growth was n-type single crystal Si due to its low cost and effectiveness for CVD diamond growth. A large slab of (100) plane Si was cut along a pre-scored edge to leave multiple freestanding $10\text{ mm} \times 10\text{ mm}$ substrates of $500\text{ }\mu\text{m}$ thickness. These were cleaned sequentially in acetone, ethanol and methanol for five minutes in an ultrasonic bath before being thoroughly rinsed in deionised water. Any grease or dirt on the substrate surface was minimised during this cleanse. The substrates were then seeded to increase the nucleation density of diamond growth. This was conducted by immersion of the substrates into a solution of a carboxyethylsilanetriol di-sodium salt (25 % in water) solution before rinsing in deionised water. The substrates were then added to a solution of diamond particles (25 carats/kg, supplied by Microdiamant) before a further rinse in deionised water. The addition of salt provided the ‘glue’ for the diamond seed onto the substrate and prevented any aggregation of the diamond particles.

Once seeded, the first layer of the betavoltaic structure could be deposited. For the MiP structure desired, the active region of the device is the vertical (transmission) region through the centre of the films and so the silicon substrate must be removed at a later stage in order to leave freestanding diamond. The thickness of the active region will only be tens of microns in total and is expected to be very brittle, so a window frame structure was designed in order to add mechanical stability to the device. By removing only the central section of the substrate, a Si frame could remain around the final structure

without affecting the device operation. The design for this structure is shown in figure 2.2.

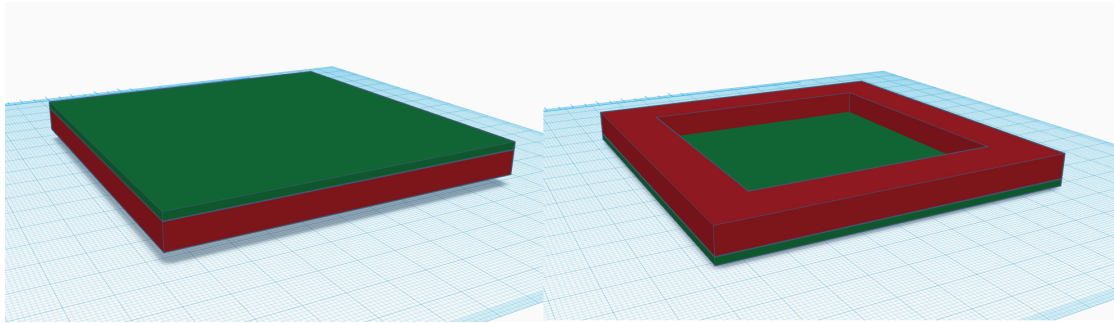


FIGURE 2.2: Model of the i-diamond layer (green) grown onto a Si substrate (red). The left image shows the structure after growth and the right image shows the underside of the frame structure of the device after unwanted substrate removal.

As seen in the left image in figure 2.2, a CVD grown diamond layer (green) would be grown onto the Si substrate (red). The central zone of the silicon substrate could then be removed in order to expose a freestanding diamond film. The resulting window frame shape (shown in the right image) provides mechanical support for the film without altering the active region of the device.

Where possible, the intrinsic layer of the device must be grown first to minimise boron contamination from a BDD layer into the undoped diamond. The undoped diamond was grown using a home-built MWCVD reactor in the University of Bristol Diamond Laboratory. The reactor was an ASTeX style reactor with proven growth rates of approximately $10 \mu\text{m h}^{-1}$ and is shown in figure 2.3.

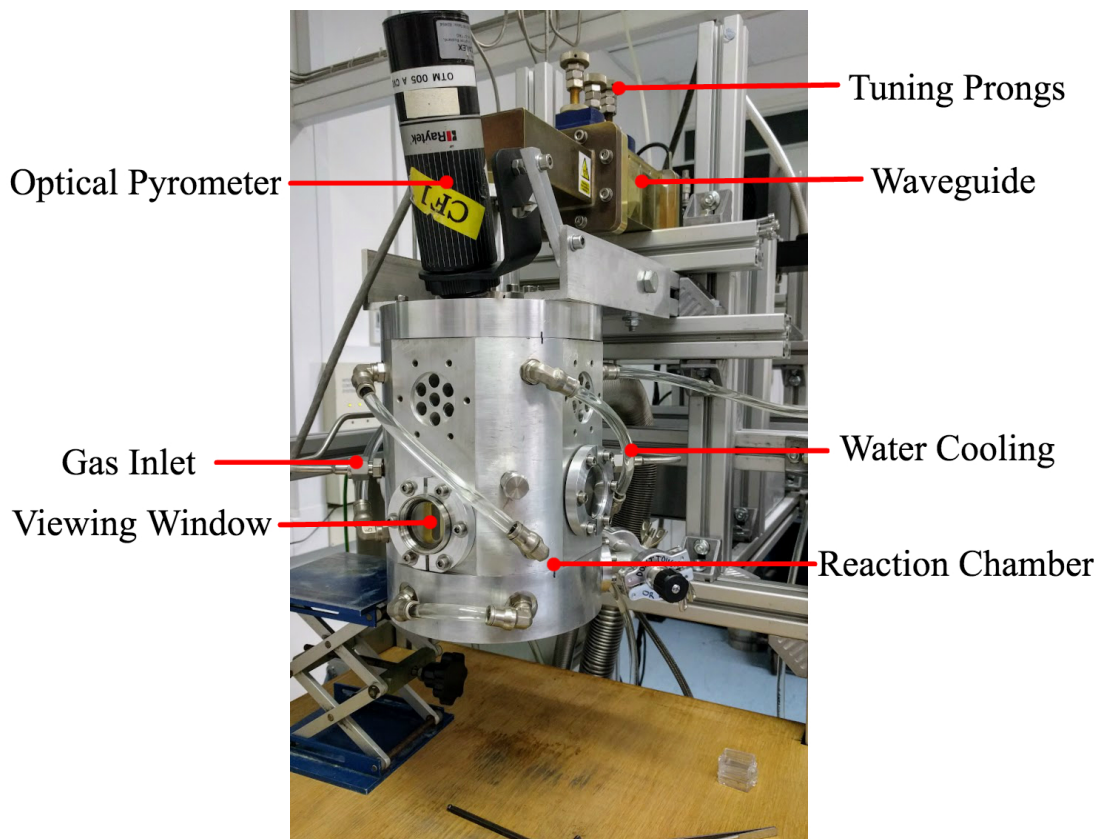


FIGURE 2.3: Annotated photograph of the MWCVD reactor used.

The 1 cm² silicon substrates were each placed onto a molybdenum substrate holder and into the CVD reactor. The addition of a 0.1 mm diameter tungsten wire beneath the substrate holder helped to provide a thermal break between the water cooled reactor base. The reactor was closed and the pressure reduced to 2×10^{-2} Torr before gases were introduced and a microwave plasma struck. The amount of reflected power was brought to a minimum using the three tuning prongs labelled in figure 2.3 and parameters kept as constant for the duration of growth. The parameters chosen were selected as the finest conditions for this reactor, determined over several studies at the University of Bristol. These were as follows:

TABLE 2.1: Undoped diamond growth conditions for the MWCVD reactor used. sccm (Standard Cubic Centimeters per Minute) is a flow rate in cm³ min⁻¹ at a standard temperature and pressure.

Pressure / Torr	130
Substrate Temperature / °C	≈ 850
Microwave Power / W	1300
Hydrogen Flow Rate / sccm	300
Methane Flow Rate / sccm	12.6

Each sample was grown using the same parameters but with varying duration in order to assess how changing the thickness of the i-layer in the MiP structure affected the workings of the betavoltaic cell. The growth durations were chosen between 2-8 hours at hourly steps. There was no method of measuring the growth thickness of undoped diamond *in situ* and so thicknesses were approximated from a previously calculated growth rate at the same conditions. The thicknesses could then be more accurately measured after deposition. The MWCVD reactor used was continuously undergoing maintenance and therefore the dates of diamond growth were noted in order to construct a timeline contingent upon any unknown discrepancies in the results.

Once the undoped diamond layer had been grown onto the substrate and removed from the CVD chamber, the central region of the silicon substrate needed to be removed in order to expose the nucleation side of the diamond as shown in figure 2.2. It has previously been shown that laser milling away the reverse of a substrate is an efficient way of removing large amounts of unwanted material. However, a balance needed to be selected which could efficiently remove the large thickness of silicon without damaging any of the diamond film grown. This could be achieved by using a laser cutter to remove the bulk of the unwanted silicon before chemically removing the final layers. A chemical etch is a much gentler way of removing the unwanted material and the solution composition could be selected which would not degrade the quality of the diamond film. The laser used was an alpha series micromachining laser (532 nm) manufactured by Oxford Lasers. A number of remnant silicon substrates were tested using an ‘in-house’ square milling program in order to finalise the laser conditions to offer the desired results. The optimised parameters are shown in table 2.2.

TABLE 2.2: Final laser mill conditions for removal of the unwanted Si substrate.

Laser Current / %	90
Attenuation / %	100
Speed / mm s⁻¹	2.5
Pulse Distance / mm	0.0025
Pitch / mm	0.005
Z-Step / mm	0.175
Number of Passes	1
Distance Milled / μm	360

After removal of most of the unwanted substrate, the rest of the silicon was removed using a 30 wt% KOH solution at 80 °C. The strong solutions were made in small volumes of 20 ml to minimise the difficulty of disposal and to allow for contaminated solutions to be changed with negligible waste. Etching of (100) silicon at these conditions has

been found to remove approximately $75 \mu\text{m h}^{-1}$ at a 55° angle to the surface [150]. The KOH solution will leave the CVD diamond unaffected and so was an effective way to remove the silicon substrate in this case. To avoid the solution etching away the desired Si frame, a Kapton[®] polyimide mask was used to specifically expose only the undesired areas of substrate. The Kapton[®] masks could be cropped to different shapes in order to distinguish between samples when in the solution. An example of a mask with the central region uncovered for removal in KOH is shown in figure 2.4.

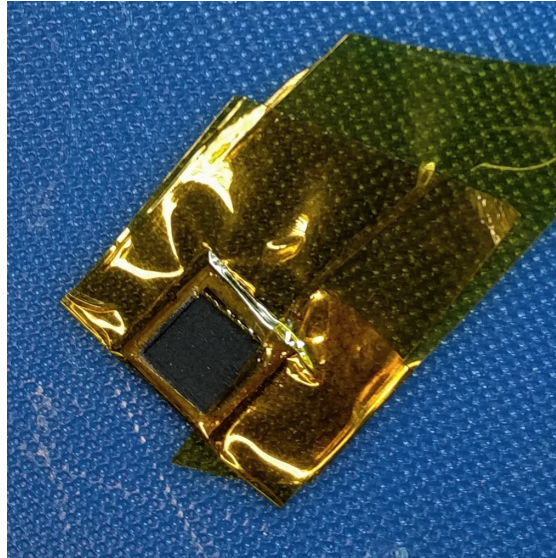


FIGURE 2.4: Photograph of a structure with Kapton[®] mask before addition to the KOH solution.

Once the unwanted silicon in the centre of the structure had been removed (approximately two hours in heated KOH), the p-type boron doped layer could be grown onto the freestanding diamond after more cleansing in ethanol, methanol, acetone and deionised water. The ultrasonication bath could not be used at this stage due to the fragility of the freestanding diamond, instead samples were soaked in each solution for roughly five minutes with multiple light agitations to swill the sample around the beaker to expose all areas to the solution. The BDD was then grown onto the nucleation face of the i-diamond in a HFCVD reactor as follows.

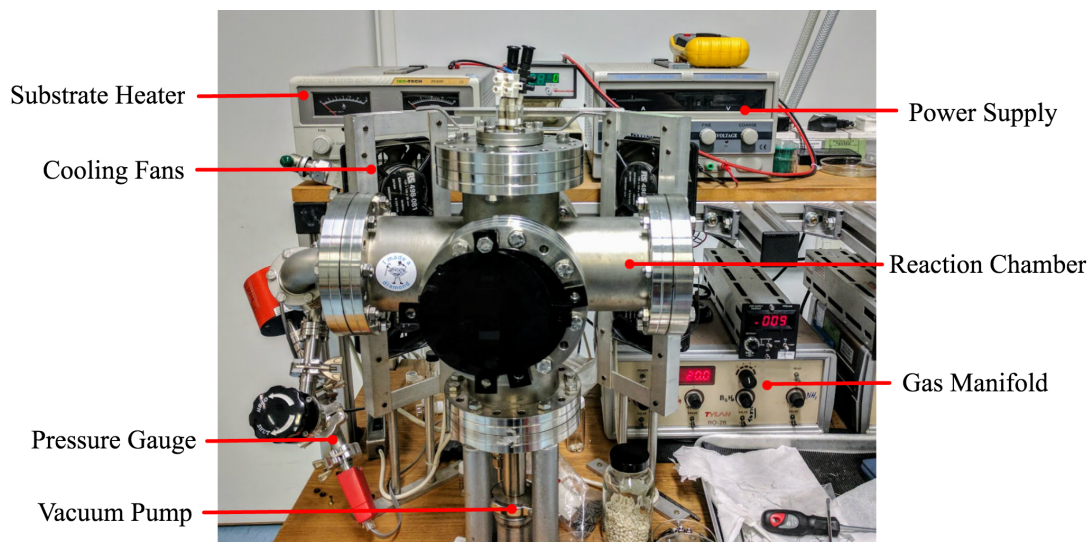


FIGURE 2.5: Annotated photograph of the HFCVD reactor used.

The sample was inserted to the CVD chamber and positioned underneath three tantalum filaments. Care had to be taken not to damage the brittle diamond layer and as a consequence metal tweezers were no longer used to handle the devices. Instead, small portions of filter paper were used to slide the samples in and out of their sample holder. Once in place, the chamber was secured and pumped down to a pressure below 10^{-2} Torr before turning on the power source. The parameters of growth are shown in table 2.3 and were checked regularly during operation to avoid drift.

TABLE 2.3: Boron doped diamond growth conditions for the HFCVD reactor used.

Pressure / Torr	20
Current / A	25
Hydrogen Flow Rate / sccm	200
Methane Flow Rate / sccm	2
Diborane Flow Rate¹/ sccm	100

The boron doped diamond film was grown for a duration of one hour to give a thin, full layer coverage of polycrystalline BDD. From additional work on this apparatus, the doping concentration of boron is expected to be 10^{20} cm^{-3} from the parameters used.

¹diborane gas is 5 % in H_2

2.2 Diamond Characterisation

The surfaces of the samples were characterised using an optical microscope, Raman spectrometer and scanning electron microscope (SEM) after each of the growth stages in order to test the quality of each surface. The optical microscope used was a Carl Zeiss AxioLab, with up to 1000 \times zoom, which allowed the surfaces of the samples to be visually analysed quickly and easily. The Nomarski polarisers on the microscope, in particular, allowed for detection of foreign contamination on the surface by enhancing the contrasts of features with different optical path lengths.

The use of a Renishaw 2000 Laser Raman Spectrometer with a 532 nm laser allowed for allotropic characterisation together with the crystallinity of the samples to be analysed. The Raman shift and width of CVD grown diamond was compared to a single crystal calibration piece after each growth run to gain this information. A visual check of the surface could also be conducted using the viewfinder window in the *WiRE* software used. The calibration scan of the single crystal diamond was conducted before every set of Raman spectra taken, in order to continually test the accuracy of the spectrometer. Any discrepancies of the diamond peak of the calibration sample from the literature 1332 cm^{-1} value are accounted for in the results [151].

As the samples were extremely delicate, both the Raman and optical characterisation methods were conducted with the samples remaining in their sample holder. The lids of the styrene sample holders could be removed to allow the surface of the sample to be freely characterised. This approach did not affect the quality of the deductions made, but the minimal transfer of the samples minimised their risk of fracture.

A JEOL JSM-IT300 SEM offered more precise assessment and viewing of the surface morphology of the CVD diamond. This also assisted in the calculation of grain sizes and thicknesses to suitable precision. In order to image the undoped diamond surface, silver conductive paint was used to stop the samples from charging under radiation from the incident electron beam, this helped in focussing onto the surface with higher magnification. The use of the conductive paint was also utilised to hold the samples steady during SEM imaging as the commonly used sticky pads were too secure for the fragile diamond films. Using the conductive paint allowed for the whole baseplate to be removed from the SEM and the sample removed by dissolving the paint in acetone. A cross section of the centre of the film was needed in order for the thickness to be accurately determined. Thickness calculations using the edges of the substrate would not be accurate due to growth of diamond over the sides of the substrate during the CVD process.

At each stage during the growth process described in section 2.1, the quality of the surfaces were tested using the three methods described in the above paragraphs. Both the nucleation and growth faces of the undoped diamond film were tested after substrate removal and any differences between them noted. Accurate thickness measurements were not conducted until the end of the research due to the destructive nature of the method used (fracturing sample to expose cross section).

2.3 Metallisation

Before the metals could be deposited onto the diamond, the surfaces needed to be thoroughly cleaned and oxygen terminated. The surfaces were cleaned with a solution of heated (75 °C, 50 wt%) HNO₃ followed by a 30 minute ozone treatment in a Jelight UVO 42A-220 cleaner. The ozone clean used ultraviolet light (254 nm) and a constant gas flow of oxygen to O-terminate the diamond. All samples were then attached to the deposition plate of a Balzer 510 vacuum coater for metal evaporation. The central region of the ohmic contacts were concealed using masking tape to expose only the corners of the sample. By masking the active region of the samples, the incoming electrons would not lose any energy on passing through a metal before reaching the betavoltaic device. The Balzer evaporator allowed for an oxygen/argon gas mixture to be added to the chamber before deposition, this would further perform an O-termination needed for metalisation. The metal to be deposited was heated to 900 °C in a tungsten dimple boat and evaporated onto the sample stage 30 cm away when at pressures below (10⁻⁵ Torr). The ohmic contacts chosen for the devices were Ti/Au onto the heavily BDD side of the devices. The carbide layer formation required for an efficient ohmic contact would be suitably constructed from the high temperatures used during the metal deposition (assessed from previous work on this apparatus). Once the ohmic contact had been attached, the samples were remounted onto the same holder with their reverse face exposed. The Schottky metal contact for this face was required to coat the active region of the device and so the masks were used in a different setup than for the ohmic contact. Both masks are shown in figure 2.6. The Schottky contacts chosen were Zr/Al and required no annealing after deposition. The contacts had to be deposited in this order due to the high temperatures required for carbide formation in the ohmic contacts lowering the barrier height of the Schottky contacts, limiting the rectifying behaviour of the device. The betavoltaic devices were ready for electrical testing after deposition of both metal contacts.

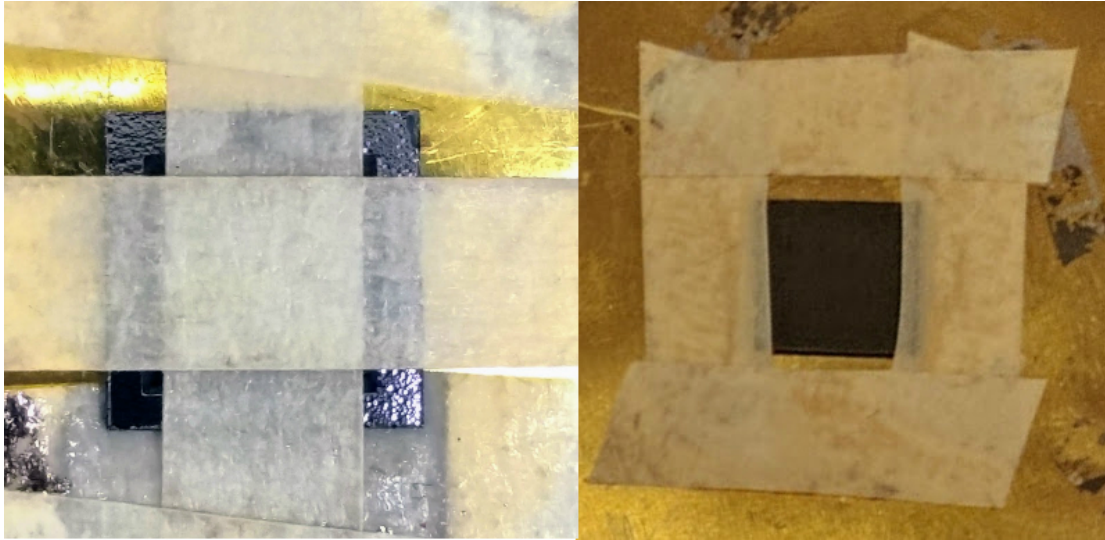


FIGURE 2.6: Photographs of the different masks used for metal deposition. Ohmic contact mask shown left with four BDD corners exposed. Schottky metal deposition mask shown right with exposed central active region.

The first attempt at adding contacts to the device did not meet the requirements for a betavoltaic device as the top and bottom metals came into contact around the sides of the device, effectively bypassing any conduction through the resistive i-diamond centre. The contacts had to be removed from both sides of the devices to overcome this. If the BDD (also conductive) was seen to wrap around the edges of any device, this also had to be removed by slicing away the edge of the sample using the laser cutter with conditions shown in table 2.2 and approximately 30 passes. The laser was focussed initially onto the CVD diamond side of the sample in order for the focus of the beam to be most accurate when cutting through the delicate part of the device. To cut through the full thickness of the sample, a milling pattern (roughly 50 μm wide) had to be used instead of a simple linear cut to remove the unwanted material and allow the laser to focus on new material as it moved lower into the device.

A thorough clean of the diamond samples was conducted in order to remove the faulty metal contacts from the devices as well as removing any contaminants from the surface. This was conducted by addition of the samples to a solution of $\text{HNO}_3/\text{H}_2\text{SO}_4$ acid heated to approximately 100 $^\circ\text{C}$ for 30 minutes under reflux. This not only removed any deposited metal, grease or contaminants from the diamond surface but also any conductive graphitic carbon which may have been introduced during the laser milling. The heated acid treatment also oxygen terminated the diamond surface which was a requirement for effective metal contacts. The metal contacts were again deposited utilising the same setup explained above but now without the oxygen/argon pre-treatment as the surface had already been thoroughly O-terminated from the acid cleaning. Great care was taken to cover the edges of the devices when the metal was redeposited.

Deposition of the metal contacts was conducted by Dr Neil Fox in the University of Bristol School of Physics. Estimations of the metal layer thicknesses were noted from previous experiments on this apparatus and by review of the coated viewing windows of the apparatus used. After metalisation, the samples were again cleaned using ethanol, methanol, acetone and deionised water, and were treated to a 30 minute ozone treatment in the Jelight UVO cleaner in order to ensure surface passivation and minimise any surface current flow.

2.4 Electrical Characterisation

Using a homemade van der Pauw sheet resistivity setup with Keithley 6221 current source, Keithley 2182A nanovoltmeter and *LabVIEW* software, the resistances of both sets of samples were calculated. The samples to be studied were placed onto a plastic stage and four gold tips placed onto the (ohmic) corner contacts of the BDD faces with care taken not to damage the active region. A current applied through two contacts on a common edge induced a voltage at the opposite two contacts which could be measured by the voltmeter. Resistances were calculated using Ohm's law at all eight configurations (current applied in both directions at each position) of contact placement in order to limit any directionality of conduction in the material. The sheet resistance (R_s) was solved using the van der Pauw formula and *WolframAlpha* online computational knowledge engine [152].

The same method was used to calculate the resistance of a number of test samples. Firstly, a BDD layer without any ohmic contacts was tested in order to calculate the resistance added by the metal contacts. The resistances of the silicon (n-type) substrate and CVD grown i-diamond layers were also calculated in order to gain further understanding of the electrical conduction through the device. The van der Pauw setup used is shown in figure 2.7.



FIGURE 2.7: Aerial photograph of the van der Pauw setup used. The device in the photograph is an unwanted test sample and does not have the four metal probes in contact with the ohmic contacts as usually employed for analysis.

The next stage to completing the betavoltaic battery structure included attaching 22 gauge tinned copper wires to the top and bottom metal contacts to allow the electrical flow through the device to be measured. Initially, this was attempted with lead/tin/silver solder but the intensity of the high temperatures required and run-off of flux used in the solder across the devices limited this use of the material. Instead, silver conductive paint was used as a softer, temporary way of fixing wires to the material. The conductive paint was initially found to wet the surface of the diamond too quickly to be of any use as an adhesive. This was overcome by allowing the paint to set at an elevated temperature for a few minutes before any contact to the device was made. By adding a drop of paint to the wire tip, leaving it to set for a few minutes on a heated hot plate (50 °C) before attaching the metal contact, a secure fix could be made between the wire and device. This was completed for both sides of the samples with a 30 minute bake on the hot plate in between attachment and use, to ensure the contact had thoroughly dried.

Once the wires were attached to all samples, preliminary electrical information of the structures was measured using a Fluke 289 multimeter. This multimeter could test for diodic character by measuring the resistances and voltage drops in both directions across the device. Full current/voltage (I/V) sweeps were then conducted on the devices in air by connecting the samples to an AIM TTI PLH250 power supply and RBD 9103 picoammeter with standard spring clips and measurements recorded using a bespoke

LabVIEW program. The I/V sweeps were conducted by manually adjusting the bias to the Schottky side of the sample whilst measuring the current using the software. Due to the large resistances of the thick i-diamond layers in the devices, potentials of up to 250 V in both forward and reverse directions were applied using this setup to induce a measurable current. The accuracies of the power supply and ammeter combination were tested against two large resistors of known resistance.

The current/voltage plots of all devices were then collected with addition of a 13.9 MBq Ni-63 beta source with only one active face. The wires connected to the ohmic side of the device were removed by dissolving in acetone and were instead connected onto the inactive face of the radioactive foil- this could be used for all structures. The 7 mm \times 7 mm nickel source used, lay comfortably within the window frame cut out of the structures, but needed a slight squeeze in order to maintain contact to the BDD face when at rest on a desktop. An empty styrene sample holder filled with precisely cut foam provided a workable bed to hold this setup. A photograph of the fixture used is shown in figure 2.8. The sample holder fixture used also completely encased the radiating beta particles, showing no increase in radiation intensity from the background scan when tested with a Geiger-Müller counter. The open circuit voltage and resistances of each sample was also recorded using the multimeter.

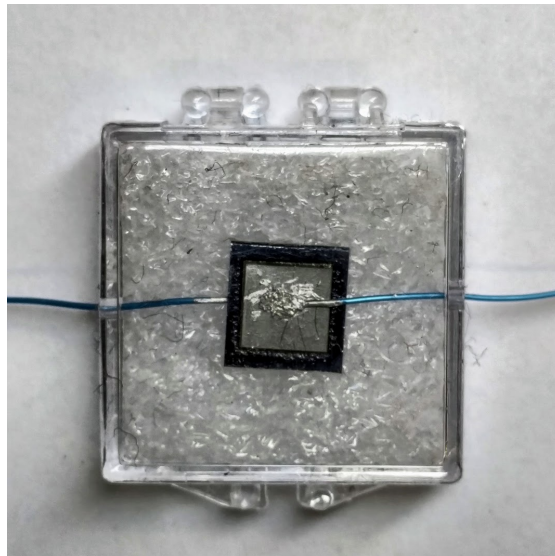


FIGURE 2.8: Photograph of the adapted styrene sample holder for betavoltaic device testing. The dimensions of the cut foam require small force to close the holder which sandwiches the beta source into the diamond structure. Note the grooves cut into either side of the sample holder to allow the wires to vacate the casing.

To test the contact of the nickel to BDD interface, a setup was constructed which swapped the Ni-63 foil with a non radioactive Ni-59 foil of the same dimensions. Again,

I/V characteristics were measured and compared to the results in which the wires were connected directly to the device.

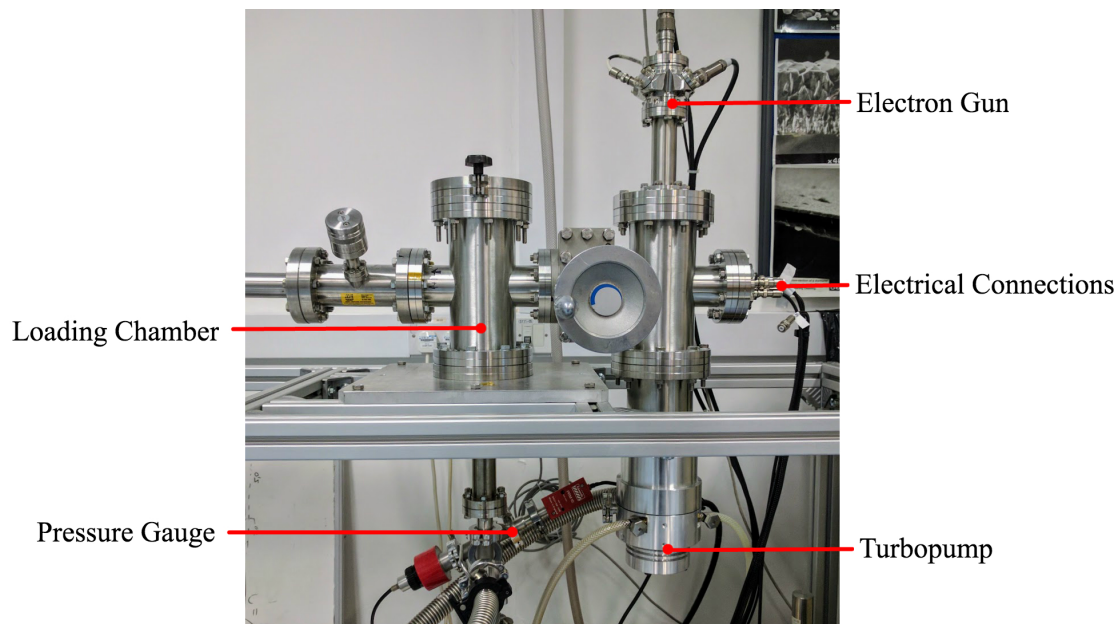


FIGURE 2.9: Annotated photograph of the secondary emission setup used.

Finally, the electrical properties of the devices were documented under vacuum. Using a secondary emission setup in the University of Bristol Diamond Laboratory (shown in figure 2.9), the necessary electrical connections could be made to the betavoltaic device within vacuum and parameters changed from the same *LabVIEW* software. Electrical connections were made to a removable sample holder which could bias or collect the current from any of the connections depicted in figure 2.10. A good electrical connection between the sample and the base plate was made by firstly connecting the sample to a removable aluminium disk (using silver paint) and then by taping this disk onto the base plate in the holder. The removable disk was cut at the onsite workshop using a 1 mm aluminium sheet. A 10 mm \times 10 mm region was then milled from the centre of the disk, using laser conditions as shown in table 2.2, to allow the samples to sit securely within a recess in the plate. A hole was finally cut through the centre of the disk to allow transmissive results to be measured (at the transmission plate) using the sample holder. The diamond device was placed inside this removable sample holder and introduced to the vacuum chamber using a sliding loading arm and gate valve. The added resistance of this route was measured using the multimeter.

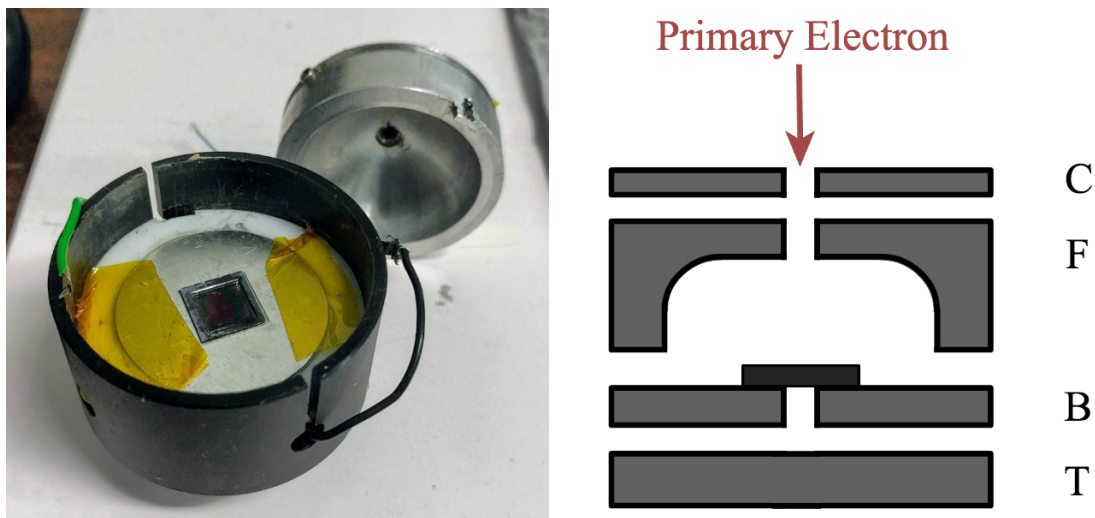


FIGURE 2.10: Photograph (left) of the sample holder for the secondary emission setup with labelled electrical connections (right). Electrical connections were possible to: collecting plate (C), Faraday cup (F), base plate (B) or transmission plate (T).

When in the operative location and at sufficient vacuum ($<10^{-6}$ Torr), I/V results were collected within the vacuum chamber by joining the wires from the device to the connections on the sample holder, bypassing their original use. The sample fixture shown in figure 2.8 could not be added to the vacuum due to large outgassing of the plastic and therefore the Ni foil was instead taped into place using Kapton[®] tape. In this apparatus, an electron beam could be incident onto the sample surface and both the reflected and transmitted yields measured at varying beam energies (up to 5 keV). Unfortunately, the electron gun was not tested in time for experimental analysis and so could not be used. An extension to this setup which utilised the secondary emission design was to place the radioactive source onto the top plate (C) with the active face pointing down towards the sample- effectively substituting an electron gun for a beta source. The secondary electron yields could then be collected using this configuration in the manner intended for this apparatus.

2.5 Simulation

Computational simulations showing how electrons penetrate and move through the diamond bulk were finally conducted for the fabricated devices. The 3D Monte Carlo software, *CASINO*, was used to model the backscattered, secondary and transmitted electron signals from the beta source and diamond device. The dimensions of the modelled sample were as experimentally recorded for the devices fabricated and multiple growth layers included in order to nearer mimic the conditions of the polycrystalline material. The parameters used specific to the fabricated device are shown in table 2.4. The number

of electrons simulated at each run was 1000 and the primary electrons were all assumed to travel normal to the surface.

TABLE 2.4: Simulation parameters utilised for the *CASINO* electron penetration software.

Average Beam Energy / keV	17.42 [33]
Maximum Beam Energy / keV	66.94 [33]
Exciton Generation Energy / eV	19.82 [85]
Boron Doping Concentration / (B/C)	1 %
BDD Thickness / nm	512
BDD Grain Size / nm	100
Diamond Thickness / μm	50
Diamond Grain Size / μm	1-15 (linear increase with thickness)

Chapter 3

Results & Discussion

3.1 Diamond Growth

3.1.1 Undoped Layer - (i)

After growth of the i-diamond layer, an initial survey of the surface, under an optical microscope, showed that there were no obvious areas of differing materials or impurities in any of the samples. The calibration scan along with Raman spectrum for the first layer of growth of sample A8 is shown in figure 3.1. For all Raman spectrum shown in this research, the intensities (y-axis) have each been normalised to the height of their 1332 cm^{-1} diamond peak to allow for simple comparisons to be made of the analysed samples. A more detailed comparison between Raman spectra could be assessed with removed baselines. However, the full spectra shown in this report are sufficient to prove that high quality CVD diamond had been grown.

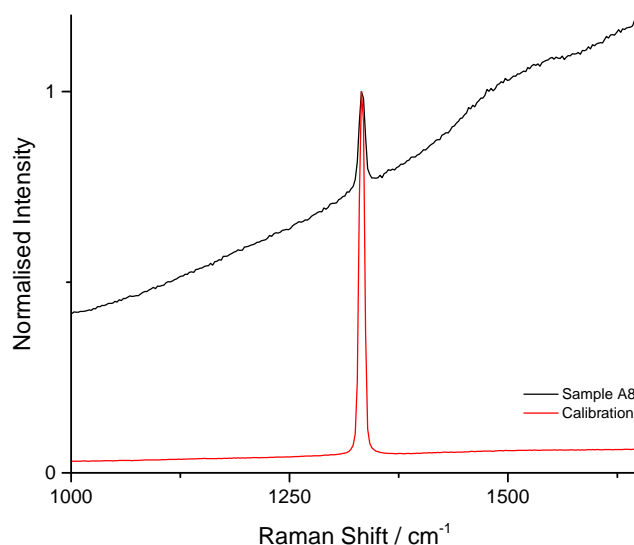


FIGURE 3.1: Raman spectra of both the undoped diamond layer of sample A8 along with single crystal calibration sample.

The intense peak of the calibration sample at 1332 cm^{-1} shows the characteristic peak of diamond. This showed that no adjustments needed to be accounted for in the CVD samples spectra. Comparison of the CVD grown spectra with this calibration showed that the surface was predominantly microcrystalline diamond and of a high quality- this deduction was made from the following observations:

1. The lack of intense peak at a Raman shift of approximately 1575 cm^{-1} shows that there is negligible graphitic (sp^2) carbon at the sample surface.
2. The small full width at half maximum (FWHM) of the characteristic diamond peak proves high crystallinity samples.

The rising background of the CVD spectrum shown in figure 3.1 is result of the photoluminescence of nitrogen vacancy defects in the diamond lattice, these are not present in the calibration spectrum due to low nitrogen content in the single crystal diamond. If the diamond were to be nanocrystalline, many more vibrational modes would become Raman active due to a break down in the vibrational selection rules from the highly disordered sample. The resulting spectrum of a nanocrystalline sample would have extra peaks throughout the $1000\text{-}2000\text{ cm}^{-1}$ range analysed in this report. Most notably, a peak at approximately 1150 cm^{-1} would be present which would show the sp^2 hybridised carbon structures present in the grain boundaries of nanosized diamond crystals [153].

The Raman spectrum shown proves that a high quality of undoped diamond has been grown, this will assist in creating an efficient betavoltaic device. The high carrier mobilities and resistances attributed with microcrystalline i-diamond will allow better charge transport and secondary electron generation through the sample bulk. By overlaying the Raman spectra of the i-diamond grown, all of the samples represent microcrystalline diamond with diamond peak centres less than 1 %, and FWHM value less than 1 cm^{-1} , from that of the single crystal calibration. The result is shown in figure 3.2. Unfortunately, sample A6 was fractured before the Raman data was collected and so is not included in the figure or any further analysis.

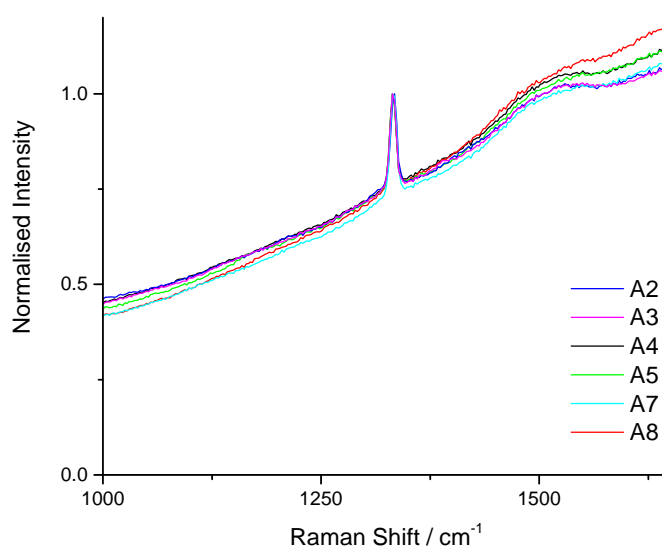


FIGURE 3.2: Raman spectra of the i-diamond growth surface for all samples.

It was expected that the quality of the spectrum would increase with increased growth duration. This was not noticed, but instead all samples showed the high quality spectra expected from the CVD reactor used. This hints that even the smallest sized grains are sufficiently larger than the region penetrated by the Raman laser. The elemental characteristics for the i-layer on the Raman spectrometer are as expected from the CVD diamond grown, SEM imaging of the same layer was then conducted in order to closely look at the morphology of the growth surface.

On initial imaging of the samples using the SEM, there were no clear regions of imperfections and all showed predominantly (111) diamond faces with a uniform grain size. The samples were of consistent thickness indicating that there was no substantial temperature gradients in the CVD reactor used. A typical SEM image of the undoped diamond growth layer is shown in figure 3.3.

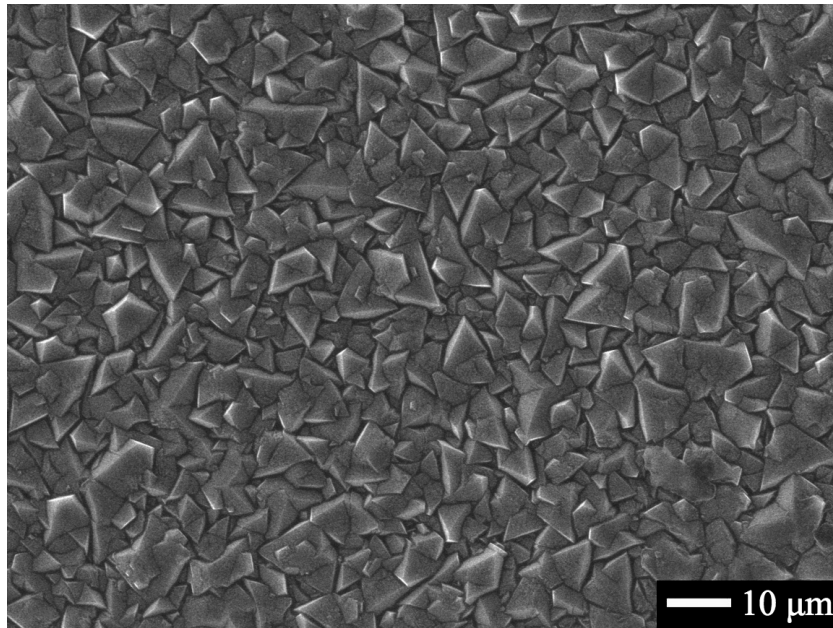


FIGURE 3.3: SEM image of the undoped diamond layer of sample A3. Beam energy = 20 keV, magnification = 1000 \times .

The determination of grain sizes was initially formulated using an intercept technique, whereby the number of grain boundaries intersecting a straight line are counted and compared to the actual length of the line drawn. However, the high density of boundaries in crevices of the larger grains resulted in wildly differing results which depended on where the line was taken. The calculation of surface crystal sizes was instead conducted as an average of randomly selected crystal faces which were fully exposed and positioned normal to the detector. As the surfaces were predominantly (111) faces, the grain sizes were recorded as the altitude of the triangular faces ¹. As expected from the previous results in section 1.1.9, the crystal sizes increased with growth duration. The formal results for crystal sizes are shown in figure 3.4.

¹the altitude of a triangle is the line segment from a corner to the opposite edge, meeting at a right angle

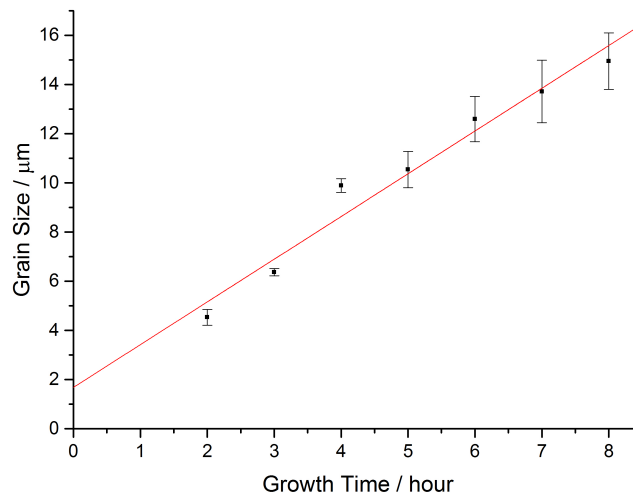


FIGURE 3.4: Plot showing the linear variation of grain size with growth duration.

From figure 3.4, the fitted growth rate line extends back to intercept near zero as physically logical for diamond growth. A reason for the small, positive intercept could be due to the diamond seed crystals having considerable size before the growth had started or simply due to inaccuracies in the data points calculated. The results were also considered to possibly overestimate the average sizes of crystals at the sample surfaces, due the bias of human selection towards the larger grain sizes, but the method was repeatable and considered to give more accuracy than the frenetic results offered with the intersection method. Consequently, these results should be taken as the upper limit of average grain dimensions.

For the final MiP betavoltaic structure appointed for this research, the thickness of the undoped diamond was varied in order to assess how the i-layer affects the electrical output of the battery. From figure 3.4, as this i-layer thickness increases, so does the grain size. The grain size of the undoped diamond will greatly affect the penetration and movement of electrons through the structure and hence will significantly alter the outcome of the structure for a given thickness. Due to the columnar nature of CVD diamond growth, electrons will rather move through any grain boundaries than through the more resistive i-diamond. This movement through grain boundaries will limit the generation of secondaries within the undoped region and so is deficient. It is not possible to simply change the thickness of the material without impacting the crystal size through this relationship. This correlation must therefore be incorporated into the final results.

As each electron is emitted from the beta source and enters the diamond to move through the thickness of the material, it will also encounter a varying size of crystal. Smaller grained regions have a higher density of grain boundaries and electron traps

than larger grains and so the electron penetration will also be subject to a varying quality of diamond. This makes estimations of penetration and escape depths, as well as a constant electron energy loss relationship, difficult due to the constant variation of diamond quality throughout the thickness of the sample. The nucleation layers will be where this variation is most pronounced and so could be minimised by growing thicker slabs of CVD diamond before polishing away the nucleation layers. This would not solve the problems created with varying grain sizes but would limit the large discrepancies at nucleation stages. However, this alternative was considered undesirable due to the difficulties of polishing diamond and the resultant large wastage of material.

At these initial stages of device construction, the thicknesses of i-diamond could not be accurately calculated as no cross sections were available to analyse on the SEM. Instead, the next stage of the betavoltaic cell fabrication was conducted and precise thickness measurements put on hold until a later stage.

3.1.2 Substrate Removal

The parameters used by the laser mill to etch away the unwanted Si substrate were tested on a number of remnant n-type silicon wafers before use on the final structures in order to find the conditions which could promptly remove most of the unwanted substrate without affecting the growth surface. The conditions of the test mills are included in table 3.1, with all tests conducted at 90 % current, 0.175 mm Z-step and 0.005 mm pitch.

TABLE 3.1: Laser conditions for seven test mills into Si substrates.

Test No.	Attenuation (%)	Speed (mm s ⁻¹)	Pulse Distance (μm)	No. Passes	Distance Milled (μm)
T1	75	2.5	2.5	1	140
T2	100	2	2	1	230
T3	100	2.5	2.5	2	390
T4	100	2.25	2.25	2	Cut Through
T5	100	1.5	1.5	1	400
T6	100	2.5	2.5	1	320
T7	100	2.5	2.5	1	360

The dimensions of the test milling patterns were scaled down to 3 mm × 3 mm to assist in prompt testing of numerous parameters (tests T1-T6). Once the optimal conditions had been found, the milling area was enlarged to 7.2 mm × 7.2 mm (T7) as a final test to see if scaling up the mill to the true size affected the cutting depth. The dimensions

of the final laser mill were selected in order to be able to fully enclose the beta source ($7 \text{ mm} \times 7 \text{ mm}$) allowing a good contact to be made. Test sample numbers T1 and T2 did not mill away enough of the substrate for efficient device constructions, samples T4 and T5 showed signs of damage to the growth surface. The degradation of sample T4 is shown in the left image of figure 3.5. Sample T3 did not show any signs of degradation to the growth surface but due to a large amount of substrate debris (silicon oxides) being generated on the milling surface during cutting, it was decided that a single pass must be used to avoid the lasers path having to cross the areas of ‘fuzz’ which would significantly alter the depth cut per laser pass. The oxidised silicon waste is shown on the final test sample in the right image of figure 3.5.

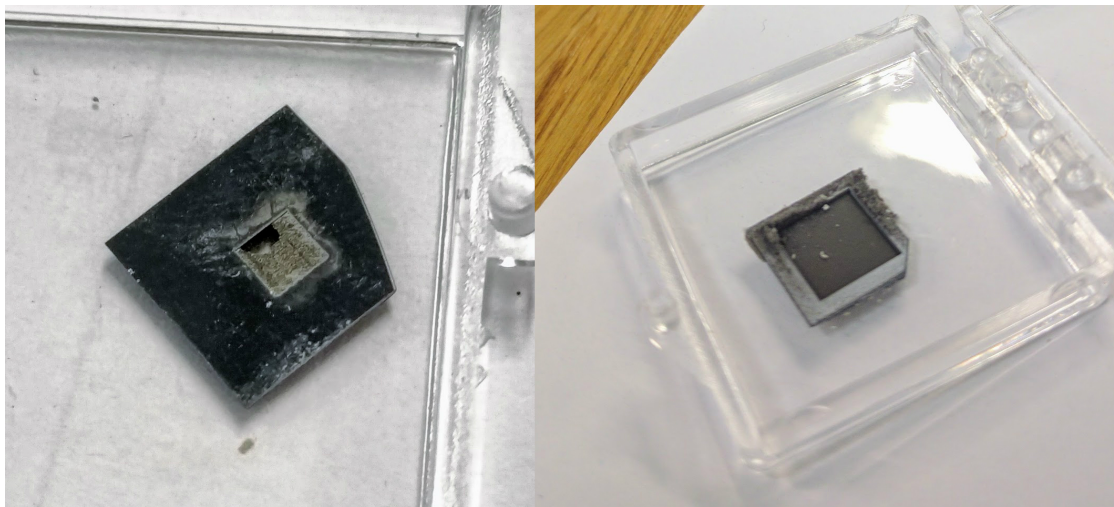


FIGURE 3.5: Photographs of two test pieces of Si substrate material after differing laser mill conditions. The left image shows sample T4 with obvious degradation to the underside during laser mill. The right image shows the final test conditions of sample T7 with significant Si oxide residue shown around the support frame.

Sample T6 gave promising results as it removed 64 % of the silicon substrate without affecting the growth surface. On scaling up the dimensions of the milling area, the depth cut increased slightly (72 %) which could be a result of either differences in the laser focus or possibly less obstruction of the laser beam by the debris. This likelihood was ignored as this result was reproducible at the larger dimension and still showed no signs of deterioration of the substrate growth surface.

Once the bulk of the substrates had been removed using the laser cutter, Kapton[®] tape was initially used to mask the areas of substrate required for the window frame structure before addition to the hot solution of KOH. However, removing the tape from the sample after the etch was completed proved difficult due to the delicacy of the i-layer. The active regions of both A2 and A3 were both fractured beyond repair and consequently could no longer be used for betavoltaic devices. The use of the mask was discontinued. When the

test sample (T7, shown in figure 3.5) was added to the KOH without any tape mask, it was found that the scored central square was etching considerably faster than the rest of the substrate. Consequently, the bulk of the frame was thought to remain when the diamond nucleation surface became exposed. The lack of tape also minimises the risk of contamination to the diamond surface from either the adhesive used in the tape or the tape itself. A photograph of the nucleation face of the resulting structure is shown in the left photograph in figure 3.6, with a microscopic image of the diamond growth side shown in the right image.

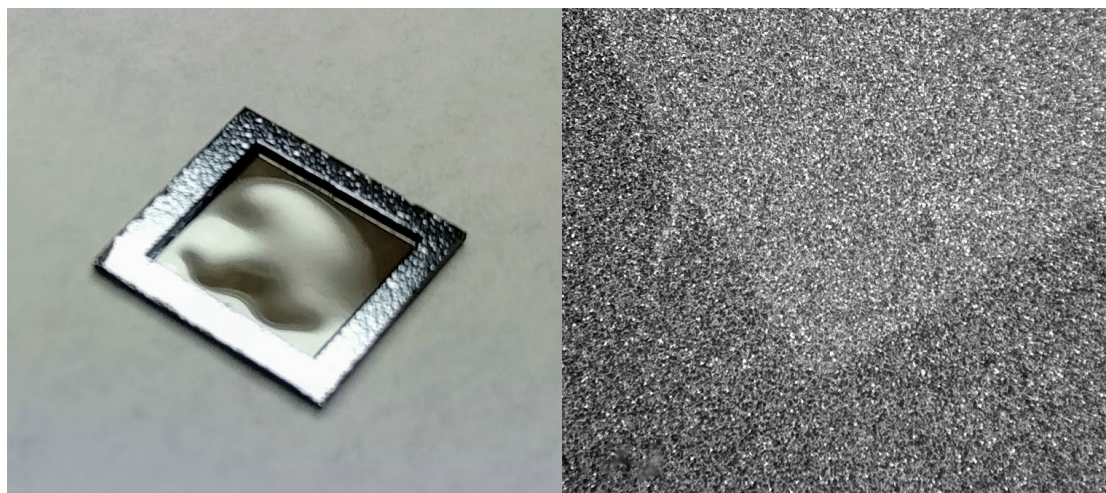


FIGURE 3.6: left) Photograph of sample A6 after KOH etch completion. Both the warped freestanding diamond and rough Si surface dimples can be noticed. right) Optical microscope image of the growth surface of sample A6 (50 \times zoom), with variation in contrast corresponding to the region of freestanding diamond film.

The exposed CVD diamond nucleation layer is remarkably shiny to the eye and can be noticed when revealed in the solution by contrast to its matte appearance before etching (compare figures 3.6 and 3.5). The exposed nucleation layer appears to be concaved in the photograph in figure 3.6, which can be clearly seen when a directional light was projected onto it. This is likely to be due to unbalanced stresses on the freestanding diamond from the silicon frame, but as this layer was very delicate- this could not be sensibly explored further. In this same image, the silicon frame can be seen to possess small surface mounds which were not present before this chemical etch was completed. These are probably due to the KOH slowly consuming the un-scored silicon surround. The frame structure will still provide the mechanical stability required from it and these small imperfections are ignored. As shown in the microscope image in figure 3.6, the quality of the CVD diamond layer was not affected during the etching process which was as expected due to the inertness of diamond to KOH. From the two regions of different contrast in this image, the frame structure can be seen from the growth side of the sample when exposed to light, showing the slimness of the CVD diamond layer grown.

The negligible damage of the chemical etch to the outer frame previously discussed was found in all but one of the samples. Sample A8 did show a significant deterioration of the frame structure when removed from the KOH, this structure is photographed in figure 3.7.

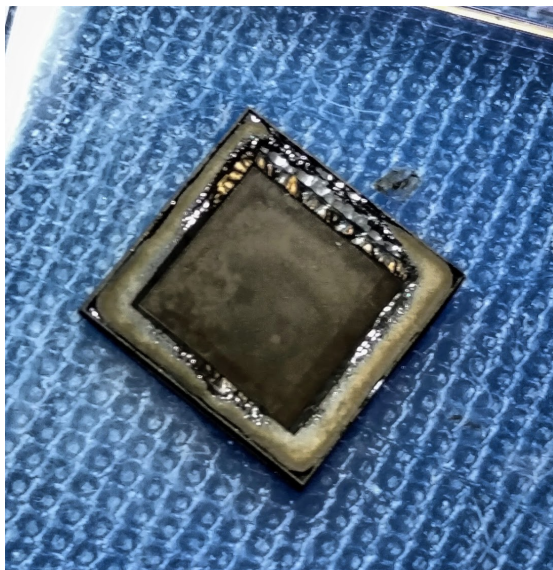


FIGURE 3.7: Photograph of sample A8 with considerable degradation of the Si support frame on all four edges.

From figure 3.7, the silicon window frame shows obvious signs of decay on all four edges of the sample. This sample was the longest growth duration observed and this degradation was initially thought to be due to the intense temperatures of CVD growth affecting the bottom side of the substrate over the prolonged growth periods. However, on further inspection of the other samples (particularly sample A7- the next longest duration) this was not seen on any edge of any other sample. The substrate temperature of A8 was not any higher than the others and so the break down of the frame was assumed to be due to the laser milling process. If the laser was not at suitable focus when the mill program was started, the initial cuts would not have been clean and may have chipped away at the surface when rastered. Any small scratch introduced from the laser cutting would then be greatly exaggerated in the KOH solution due to the isotropic etching of solution if present within a small crevice. This hypothesis would also explain why all four of the side walls of this sample are damaged. Despite the obvious degradation, sample A8 had no damages to the active window region and so was assessed further.

The cloudy surface contamination seen in figure 3.7 when compared to the photograph in figure 3.6 was removed when cleaned with ethanol, methanol, acetone and deionised water. This surface impurity was also seen at another point during KOH etching. The

reason was considered to be due to large amounts of removed silicon in the small volume of solution. A fresh batch of KOH solution was made to overcome this on both occasions.

3.1.3 Nucleation Face

Once all silicon was removed from the active regions of the devices, the newly exposed nucleation surfaces were assessed using an optical microscope, Raman spectrometer and SEM as previously conducted for the growth face. On initial inspection of the nucleation surface under the optical microscope, small imperfections in the frame edges could be noted in samples other than A8 which were not seen by eye. However, these were minor and thought not to be obviously affecting the mechanical benefits of the frame. These were still noted for possible elaboration at a later processing stage. An example of this edge fracture together with substrate surface roughening is shown in the left image of figure 3.8. A high proportion of the substrate surfaces and frame edges inspected had not degraded considerably from the etching process. The decay of the silicon frame was lessened over the course of the wet etching process, probably due to the increased ability to see when the diamond layer was entirely exposed. This limited the time for the samples to be in the solution. An example of a corner frame which has held up well throughout the etching process is shown in the right image of figure 3.8.

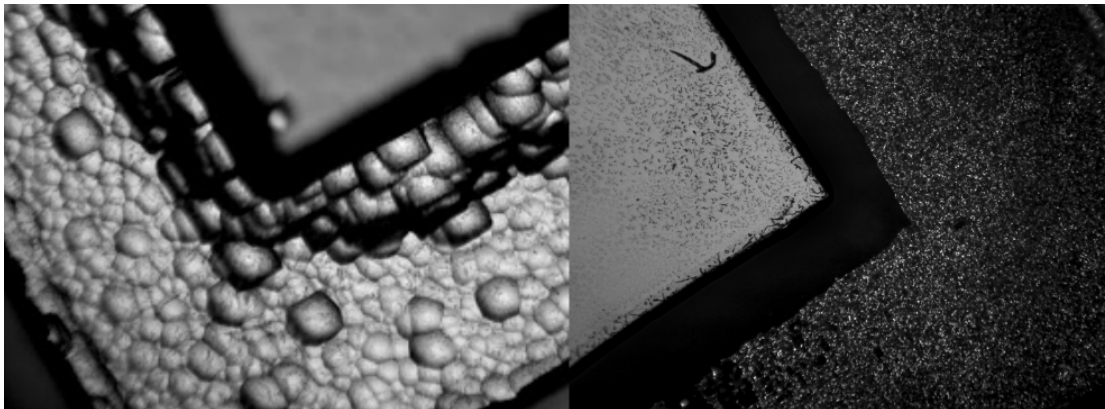


FIGURE 3.8: left) Optical microscope image of sample A6 ($50\times$ zoom) showing slight degradation of Si frame and surface dimples (photograph shown in figure 3.6). right) Optical microscope image of sample A5 ($50\times$ zoom) showing minimal break down of the Si frame and unknown contaminant on the active region. The image shown is comprised of two images at differing focal lengths and was merged into a single image using *Pixlr* editor

In the right image of figure 3.8, a mesh like pattern can be seen when under the optical microscope which was not spotted by eye. This area was going to make up the active region of the final devices and so this surface needed a further inspection to assess whether this smear was a contaminant, and if so, how to remove it. On further inspection of

the web pattern found on sample A5 (figure 3.8), a similar impurity was present on the nucleated surface of A8. Viewed under the microscope with Nomarski polarisers, there was no difference in contrast between the ‘vein’ like patterns and the flat surface showing that both were at the same plane. The results from the optical microscope were not conclusive in determination of this contaminant and so the samples needed further investigation to assess what this could be. The web pattern was a surface feature and so the SEM was selected to give better topological information than the Raman spectrometer. An SEM scan of sample A8 immediately showed a netlike pattern across the nucleation face at low magnification ($20\times$) as shown in figure 3.9, but nothing unusual was noted at higher magnification.

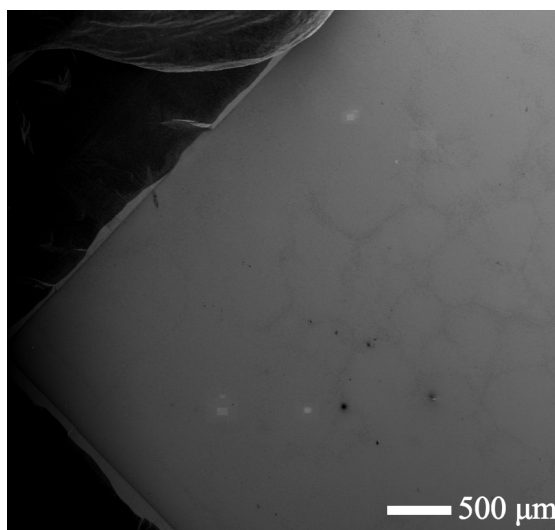


FIGURE 3.9: SEM image of sample A8 showing webbed pattern on the nucleation face of undoped diamond. The image shows rectangular regions of charged surface where the electron beam has previously been focussed despite the use of silver conductive paint (top left) to limit this. Beam energy = 5 keV, magnification = $20\times$.

Both of the samples which featured this surface contaminant were isolated and again cleaned with ethanol, methanol, acetone and deionised water. These samples were also soaked in HNO_3 and xylene in a soft attempt to remove any stubborn substances without having to polish the surface. On further examination under the optical microscope, the contaminant on these samples had been removed by the second cleaning process. It is not known what was the cause of this impurity, but both of the offending samples were etched using a common batch of KOH solution which may have been contaminated. The solution used had also been previously subject to the Kapton[®] tape from the first attempts at chemical etching. The unknown mesh pattern could be due to any form of impurity in this solution, possibly introduced from the adhesive in the tape or an impurity on the glassware used. As this webbed substance was simply removed using the

second clean, this surface matter could also have been due to an improper clean of the samples the first time around.

Once the surface contaminant had been removed from the two samples, all samples were analysed in the SEM for higher magnification surface imaging. The nucleation faces at higher magnifications showed a smooth surface with the only topological variations being thinly dispersed craters. There were regular regions of varying intensity, corresponding to a different material composition, of a similar size and shape to the craters but they appeared in a common plane with the surface. Both of these features are revealed in figure 3.10. The sizes of these regions were approximately μm in diameter. The craters aforementioned could be the locations at which there was large silicon crystals in the substrate used and the areas of differing contrast could be due to different compositions of the initial diamond growth. The Si substrate material was attributed to be the cause of this variation.

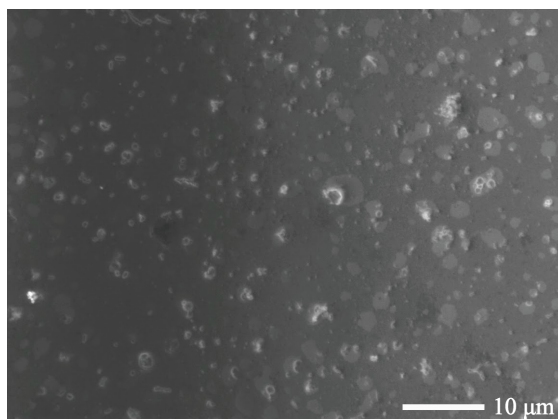


FIGURE 3.10: SEM image of sample A4 showing small craters in the nucleation surface as well as similar sized regions of differing intensity. Beam energy = 20 keV, magnification = 1900 \times .

The samples were then analysed in the Raman spectrometer to complete characterisation of this layer. The resulting Raman spectra still showed the intense 1332 cm^{-1} diamond peak but now with larger peak spreading and a larger graphitic carbon bump at 1575 cm^{-1} . The FWHM of the diamond peaks in all samples' nucleation faces were larger than the corresponding growth faces. This was as expected due to the higher purity diamond being found at the larger crystal sizes on the growth face. Essentially, the surface of the nucleation face was totally comprised of impurities and so the resulting spectrum is expected to be of lower quality. However, the penetration depth of the Raman laser is expected to be greater than the thickness of the nucleation region and so the spectrum will still show the strong diamond peaks from deeper within the bulk material [154]. The Raman spectrum of the nucleation face of sample A8 is compared to the growth side of the same sample and is shown in figure 3.11. The larger graphitic carbon bump

of the nucleation face can be noted at approximately 1575 cm^{-1} and an overall higher background intensity noted from the intersection of the intensity axis at a Raman shift of 1000 cm^{-1} . These trends were seen across all samples.

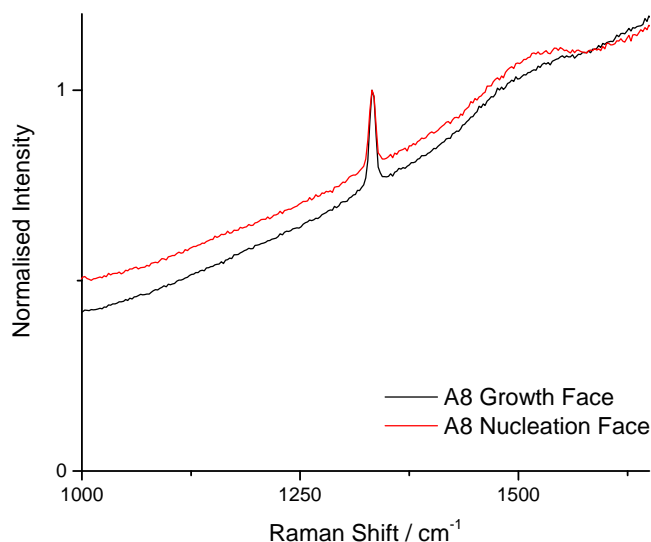


FIGURE 3.11: Comparison of the Raman spectra of the nucleation and growth faces of sample A8.

The nucleation surface had been sufficiently characterised with no obvious deficiencies found and so the samples could now go onto the next fabrication step- to have their BDD layer grown. It was decided that the BDD layer would be selected to be grown on the nucleation side of the freestanding diamond, for a number of reasons. By having the electrons penetrate the structure through the nucleation region, the primary electrons will pass through the region of highest grain boundaries and hence trapping density when they have the most energy. On passing this nucleation layer (albeit with a considerable energy loss), any low energy secondaries generated will have the higher quality material to travel through to reach the reverse face. By growing the BDD on the nucleation face, the beta source can also sit within the frame structure to provide a casing for the betavoltaic battery. This case will encourage a secure contact between the beta source and the diamond whilst also providing some containment from the radiating beta particles allowing for easier handling.

3.1.4 Boron Doped Layer - (P)

The BDD was grown in a separate CVD reactor as not to contaminate the reactor used to grow solely undoped diamond. Any small boron contamination of the i-diamond layer

would dramatically affect the workings of the device by reducing the mobility, depletion width and hence limit the generation of secondaries. The boron impurity concentration of the i-layer must be as low as feasible due to the mobility rapidly reducing to as little as 1.5 % of its pure value on doping concentrations of 10^{16} cm^{-3} [155]. A thin layer of BDD was sufficient to provide the heavily p-doped layer required for efficient electron penetration, electrical conduction and to provide the surface needed for ohmic metal deposition. Growing this layer as thinly as possible would cater for these criteria whilst also limiting the region for high electron energy loss. From previous work on the HFCVD apparatus used, it was established that approximately 15 minutes of growth was the minimum time needed in order for full layer coverage of BDD onto a diamond substrate. However, growth using a frame structure or even growing onto the nucleation side of diamond had not been tested. The unusual shape of the window frame structure is thought to introduce temperature variations to the surface due to the Si frame and nucleation layer being different distances from the filaments. For these reasons, the growth time was chosen as 30 minutes in order to achieve a full covering of film. Tantalum filaments were chosen over the superior (but considerably more expensive) rhenium wires due to there being no need for H-termination of the samples or for longer growth durations which would have otherwise limited the use of tantalum.

A blind test in an SEM was conducted between a sample with BDD layer and a sample without the layer to assess whether the 30 minute grown layer was of full coverage. The full explanation of this is shown in appendix A. The outcome of this trial was in fact that a full hour's BDD growth was needed to conclusively give full film coverage. An SEM image of a final BDD layer is shown in figure 3.12.

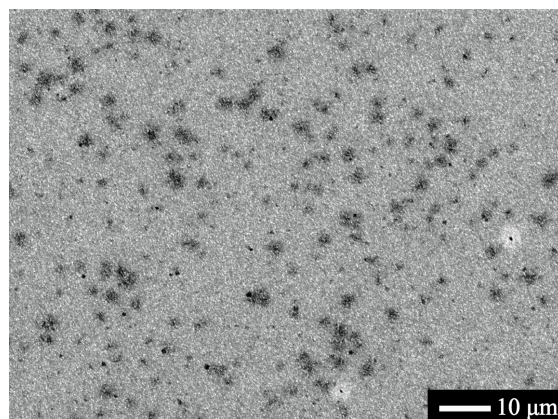


FIGURE 3.12: SEM image of sample A5 showing BDD layer with scattered regions of differing intensity. Beam energy = 20 keV, magnification = $1200\times$.

From figure 3.12, there are obvious regions of differing material make-up shown by the darker patches in the images. These were seen across all samples and presumed to be due to the similar sized inconsistencies, noted in figure 3.10, from the Si substrate. Due

to the lack of focus at higher magnifications, no accurate grain size calculations could be documented, but the morphology of the BDD layer was noted as nanocrystalline. The hour long boron doped diamond samples also had a blue tinge when viewed by eye, this is expected for heavily doped BDD samples due to the boron impurities in the crystal changing the wavelength of scattered light [156].

3.1.5 Thickness Measurements

At this stage in betavoltaic device fabrication, there was sufficient indentation within the samples for depth measurements to be taken using cross sections of the fractured active regions. Samples A2, A3 and A6 had all been broken prior to the BDD layer growth and therefore thicknesses of these samples could be analysed and an approximate i-diamond growth rate distinguished without having to fragment any of the remaining devices. In order to calculate the thickness of the BDD grown layer, sample A2 was bisected and one half entered to the HFCVD chamber for an hour's BDD growth. The cross sections of both halves of A2 were then compared in the SEM. The samples were held into place using a metal jig with silver conductive paint added to the surface to avoid charging. A photograph of this setup is shown in figure 3.13.

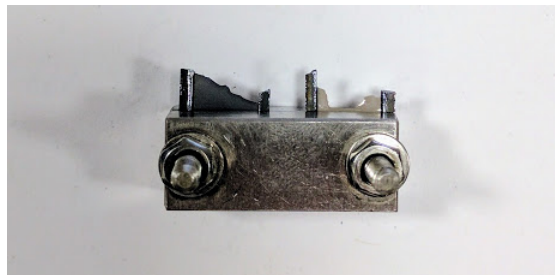


FIGURE 3.13: Device used to measure cross sections of grown CVD diamond holding two halves of sample A2. The fragment on the left is darker than the fragment on the right showing the presence of a BDD layer.

The difference in darkness between the active regions of the two samples shown in figure 3.13 show the presence of a BDD layer onto the thin i-diamond layer. An example of the resulting SEM image of the i-diamond only sample is shown in figure 3.14.

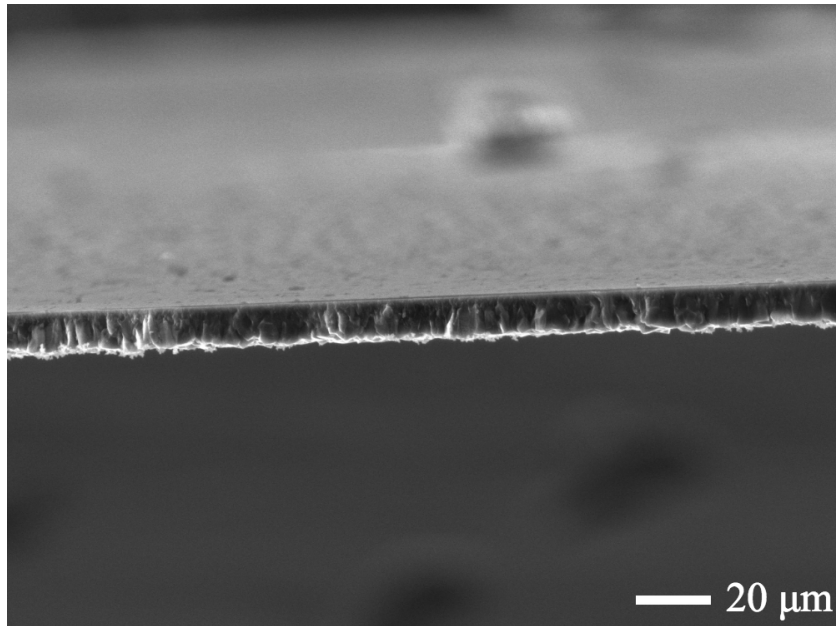


FIGURE 3.14: SEM image of the cross section of sample A2. Beam energy = 20 keV, magnification = 750 \times .

The thickness of the sample could be promptly calculated using a ruler tool included in the software package of the SEM used. However, the ruler tool required the user to select a line parallel to the surface in order to calculate the normal growth. The accuracy of this method relied on visual interpretation of a common plane within the inherently rough surface. To counteract this, the thicknesses of the samples were calculated using the online *Pixlr* image editor which could detect and outline the surface shape from differing contrasts seen within the image. By noting the shortest distance (in pixels) between the highlighted regions above and below the sample and comparing this to the scale bar, the actual thicknesses of the samples could be calculated with far greater accuracy. An image using this method is shown in figure 3.15 with the surface outlines highlighted in blue.

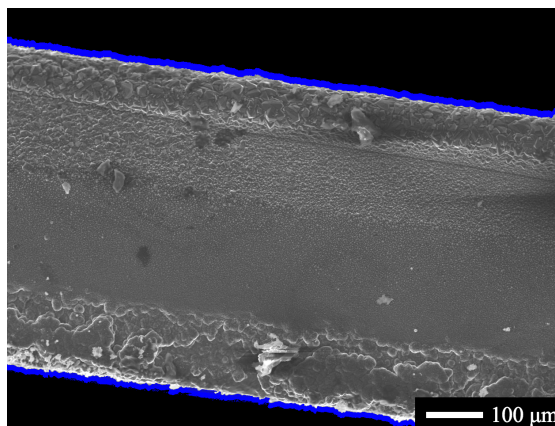


FIGURE 3.15: SEM image of the edge of sample A6. Beam energy = 20 keV, magnification = $130\times$. This image shows the edge of the sample rather than a fractured cross section, the presence of diamond growth over the sides of the substrate can be seen.

Using the cross sectional images from the SEM and *Pixlr* online photo editing tool, the thickness of the BDD film was calculated as 510 ± 20 nm and the varying thicknesses of the i-diamond layers are shown in figure 3.16.

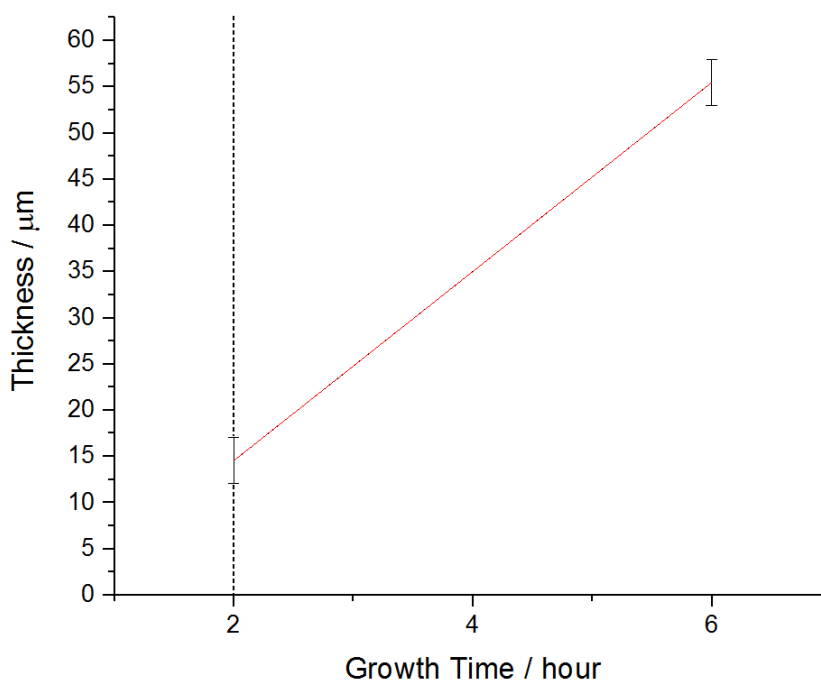


FIGURE 3.16: Plot using the thickness measurements to calculate an approximate growth rate. The growth was assumed to be unstable during the nucleation period below 2 hours.

It was assumed that the growth rate of the i-diamond layer would be linear after the initial nucleation stages of CVD growth. The minimum growth duration of the samples was two hours and so the nucleation region was assumed to be within this time period and discounted from the rate calculation. A growth rate of 10 ± 2 $\mu\text{m h}^{-1}$ was calculated

from the slope of the fitting line in figure 3.16 between the two measured growth times. This was broadly as expected from previous studies at similar conditions in the MWCVD reactor. From the calculated growth rate, the thicknesses of the i-layers are shown in table 3.2.

TABLE 3.2: Thickness of i-diamond layers for different durations calculated from an estimated growth rate.

Sample Number	Approximate Diamond Thickness / μm
A2	15
A3	25
A4	35
A5	45
A6	55
A7	66
A8	76

A later thickness calculation of sample A3 measured at $23 \pm 2 \mu\text{m}$ which is within the associated error range of the thicknesses approximated from the growth rate.

3.2 Metal Contacts - (M)

The next stage of betavoltaic battery fabrication was to deposit the metal contacts onto either side of the structure. Both sides of the device were to have two thin layers of metal deposited onto them from the Balzer vacuum evaporator. On inspection of the nucleation side of the device, the chemical etch of the silicon had left a wedge of substrate, sloping from the BDD layer surface to the top of the silicon frame structure. This sloping frame is depicted in the model in figure 3.17. When the ohmic contacts were attached to the device, a full continuous path from the top of the substrate to the BDD surface would remain (shown in figure 3.18) ².

²the BDD layer (shown blue in figures 3.17 and 3.18) had grown around the top of the silicon frame structure (red), this is not depicted for simplicity and was not considered to be a continuous covering layer

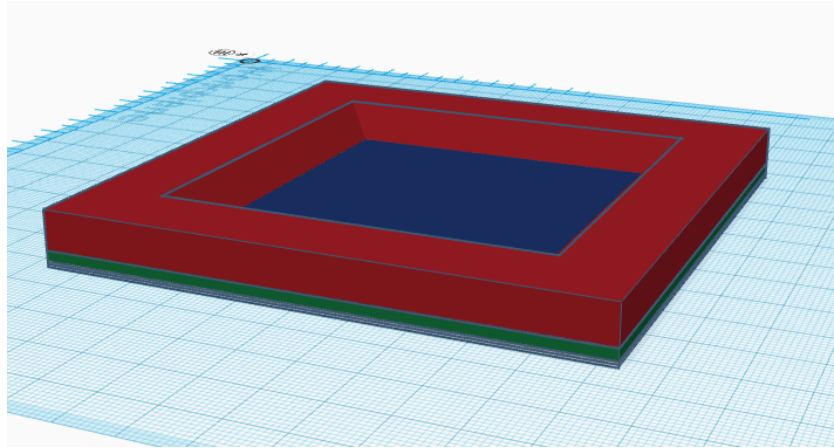


FIGURE 3.17: Model of the window frame structure with red silicon substrate, green i-diamond layer and blue BDD layer. The anisotropic etching of KOH on the silicon substrate has left a sloped region from the BDD layer to the top of the silicon frame.

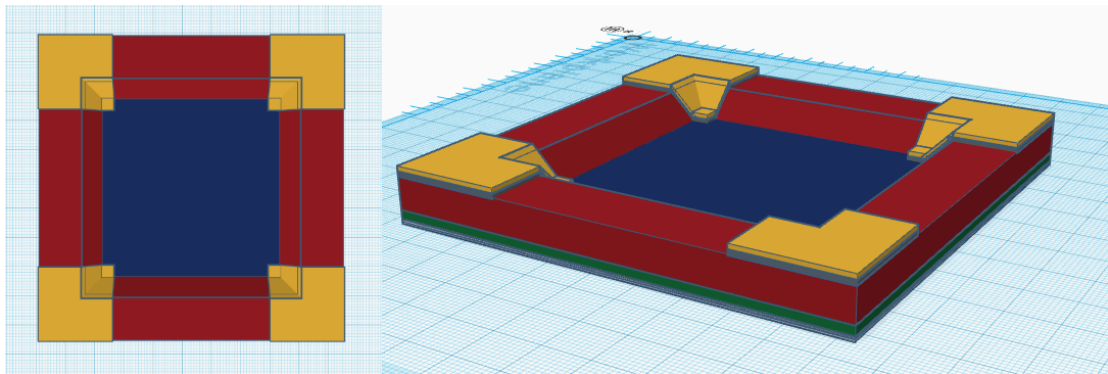


FIGURE 3.18: Model showing how the ohmic metal contacts will deposit onto the sample. Evaporating the metals from a direction normal to the surface has caused sufficient metalisation between the BDD and top of the Si frame.

The samples were thoroughly cleaned, oxygen terminated and both ohmic and Schottky contacts applied before being inspected for quality of deposition. It could immediately be noted that in some cases, the metal contacts were overlapping the sides of the devices, bringing the top and bottom of the samples into immediate contact. This would restrict the transport of electrons through the active region of the device as all current would preferably flow around the edge due to the negligible resistances when compared to that of the thick i-diamond layer. In CVD growth, the deposited solid is found to grow over the edges of the substrate material exposed to the reactor. Due to the high concentrations of boron used for the BDD layer growth, it is likely that an overlapping conductive path would be formed around the edges of the sample, again hindering electron flow through the active region. To remove the overlap of the BDD/metals, thin slices were laser cut away from the edges of the devices in order to reisolate the two metals of the device. An

image showing the device with both contacting metals and removed edge is shown in figure 3.19.

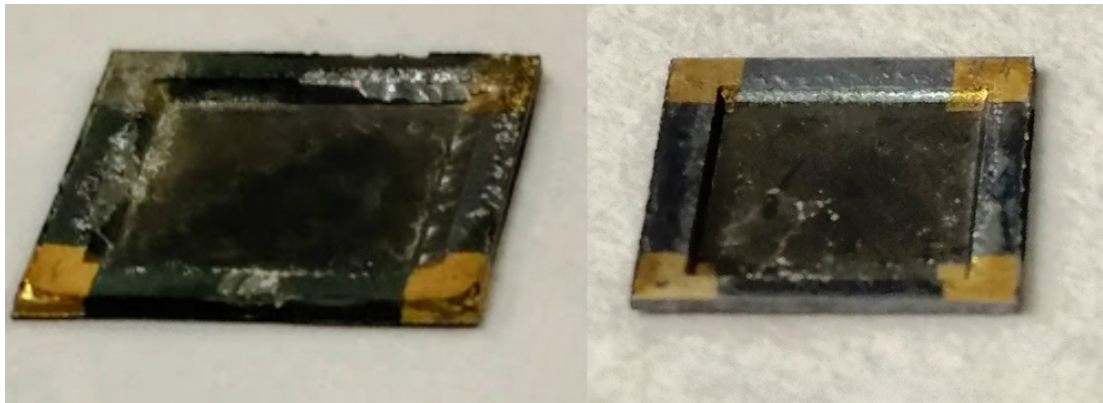


FIGURE 3.19: left) Photograph of sample A8 with ohmic (Ti/Au) metal contacts overlapping the sides of the device. right) Photograph of sample A7 with front edge removed in the laser cutter.

Although the two metals will now be isolated, any graphitic carbon or surface impurities from the laser mill may be present on the edges of the devices, which could still allow conduction around the surfaces. For this reason, the contacts needed to be completely removed from the samples, a thorough acid clean conducted to remove all surface contaminants and the new contacts re-deposited using an updated mask.

Despite needing to be removed from the window frame structures, the ohmic contacts deposited onto some of the test samples could still be analysed by the van der Pauw setup. The thickness of the ohmic contacts were estimated as 10 nm of Ti covered with 80 nm of Au. Two BDD layers had their electrical properties characterised with and without the addition of the ohmic contacts and by comparison of the two results, the ohmic contacts were approximated to increase the sheet resistance of the samples by $0.3 \Omega/\square$. This difference was considered negligible to the $10^5 \Omega/\square$ expected from the undoped diamond³. The ohmic contacts were added to the devices primarily for the sheet resistivity measurements to be assessed, as the small areas ($< 1 \text{ mm}^2$) of planar contact were considered too small for metal wires to be attached to the top face of the final betavoltaic device. In this context, contact to the reverse of the beta source would provide a more stable connection. For these reasons, the ohmic contacts were not re-attached to the devices and instead, the sheet resistivity measurements were recorded directly from the heavily BDD layer. The Schottky metal contacts were re-deposited to the centre of the i-diamond surface at thicknesses of approximately 10 nm Zr capped with 50 nm Al.

³ohms per square (Ω/\square)- unit of sheet resistance that is dimensionally equal to an ohm

3.3 Device Testing

3.3.1 Sheet Resistivity Measurements

Once the metals were removed from the devices and the Schottky contacts re-applied, the resistances of the samples were measured using the van der Pauw method. Due to the low resistances of the BDD layer, large currents of up to mA had to be applied in order to induce a measurable voltage across the film. Any lower currents caused an insufficient voltage to be induced across the sample and the voltage/time plot did not show the alternating pulsing wave pattern as required from the oscillating potential.

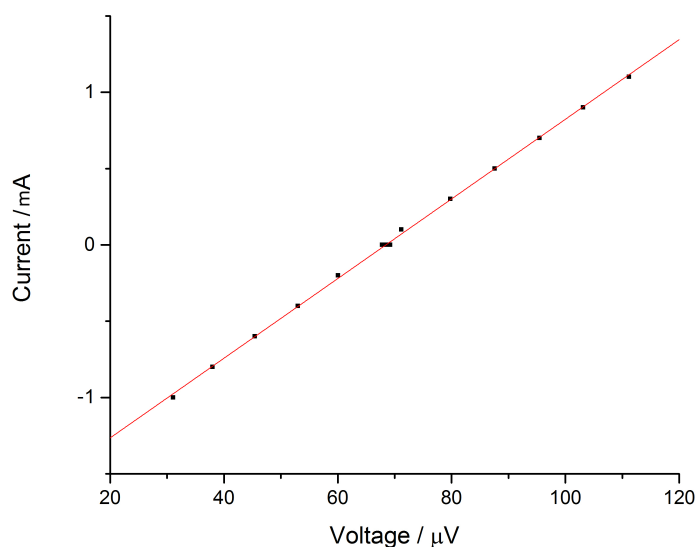


FIGURE 3.20: Linear I/V plot of a planar BDD film from the surface conductivity measurements in the van der Pauw setup.

The resulting I/V plot of one configuration from this apparatus is shown in figure 3.20, with gradient proportional to the resistance of the film (Ohm's law). The overall sheet resistance of the BDD layer was calculated using the van der Pauw equation as $29.7 \pm 0.9 \Omega/\square$. This value was higher than expected for heavily boron doped diamond, but could be due to the high density of grain boundaries in the nanocrystalline diamond obstructing the current flow through the conductive BDD grains.

The sheet resistances of the i-diamond and Si substrate were also calculated to complete the conductivity results for all components. A much lower applied current was used for the i-diamond layer due to the increased resistance that it possessed. The sheet resistance of the oxygen terminated undoped diamond was calculated as $0.36 \pm 0.05 \text{ M}\Omega/\square$. This large resistance was a requirement for the final betavoltaic structure and again revealed

the quality of the i-diamond layer and determined sufficient O-termination (or at least lack of conducting surface termination). A supplementary sample of the silicon substrate used was found to have a sheet resistance of $21.1 \pm 0.4 \Omega/\square$. This result flagged concerns as the silicon frame was providing less resistance than the rest of the structure and was subject to complete investigation.

The fact that the silicon substrate was conductive meant that additional care regarding the edges of the structure needed to be taken. If the window frame structure was sufficiently resistive, simply separating the top and bottom of the structure as depicted in the laser cut sample in figure 3.19 would force the electrical flow through the active region of the device due to the large resistive path around the edges of the device. However, the reality that the frame is more conductive than any other section of the device obstructs this notion. Any beta particles entering the BDD layer can now simply travel around the frame with little resistance. The paths available for current flow about the device can now be simplified to either along the edge of the i-layer or through the bulk of the i-layer (with similar path lengths), as everything above and below this film being assumed to be in contact and not greatly affecting the total resistance of the sample. Any small contaminants or overlaps around the edge of this undoped diamond could provide a route for carriers to flow around the device without ever passing through the active region, evidently disregarding the function of the structure. The second deposition of the Schottky barrier metal into only the central region of the device, alongside regular oxygen surface treatments, will limit the carrier flow around the surface of the device by increasing both its path length and surface resistance.

Despite this shortcoming, thin wires were attached to the top and bottom of the devices using silver conductive paint to allow the full current/voltage characteristics of the samples to be measured. This would give further information to assess whether the surfaces of the devices were allowing an alternative route of conduction.

3.3.2 Current/Voltage Characteristics

Preliminary trials were conducted on the devices using a Fluke multimeter. By connecting the wires from the samples to the multimeter in both directions, it allowed testing to see if the devices showed any diodic behaviour using the ‘diode test’ function on the multimeter. A purchased zener diode was first tested using the multimeter which reproduced the appropriate voltage drop, proving the efficacy of this method. All samples were tested this way with none showing any rectifying behaviour. On further inspection of the multimeter manual, the multimeter was programmed to display that no rectifying characteristics were present for any samples with a voltage drop higher than 5 V. The betavoltaic devices

tested have thick i-diamond regions with corresponding high resistances. This would give voltage drops considerably higher than the maximum values read by the multimeter and it was considered that this method could not be used to test for the rectifying behaviour of devices. Instead, the resistances of the samples were measured in both directions across the active region in order to assess any differences. Most of the devices were above the maximum resistance measured by the multimeter ($500\text{ M}\Omega$) in both directions with only one sample (A8) showing lower resistances of $329\text{ k}\Omega$ and $284\text{ k}\Omega$. The resistances found in this sample are undoubtedly due to electron flow between the contacts through some pathway other than the active region. This sample was recleaned and contacts re-attached in order to try and find the cause of this low measured resistance, but with no success. This lower resistance sample was not discounted despite its obvious flaws and was continued to be characterised with the other devices.

One of the devices (A5) originally showed a lower resistance in one direction than the other. When sample A5 was connected in the reverse direction, its measured resistance was above the $500\text{ M}\Omega$ maximum for the multimeter used. However, when connected in the forward direction, the resistance measured initially displayed $111\text{ M}\Omega$ before counting up to the maximum value over approximately five seconds. This device therefore showed different electrical resistances in the forward and reverse directions and was showing some sort of capacitance established from the increasing resistance with time. This sample was the only device to show rectifying behaviour and was the most likely to show full diodic character when tested in the I/V setup.

Before the samples were connected to the power source and ammeter setup for I/V analysis, a background current reading was taken. The large amount of electrical noise present in the lab gave current fluctuations on the order of $10\text{-}100\text{ pA}$. This background value would moderately spike to tens of nA randomly, possibly due to use of the large nuclear magnetic resonance (NMR) spectrometer in the adjacent laboratory or any movements of other lab users and their apparatus. The capability of the electrical setup as a whole could be increased if measurements could be conducted within a Faraday cage to limit any external noise. The setup utilised in this research was mostly connected with shielded BNC (Bayonet Neill-Concelman) cables but occasionally used single-pole connectors which would greatly increase the background noise. Updating this wiring would prove a simple method to minimise the error in the current measured. Nevertheless, the accuracies of the power source and picoammeter setup were tested against two known resistors of $100\text{ M}\Omega$ and $1000\text{ M}\Omega$ through the full 250 V range of the source. The results for both resistors are shown in figures 3.21 and 3.22.

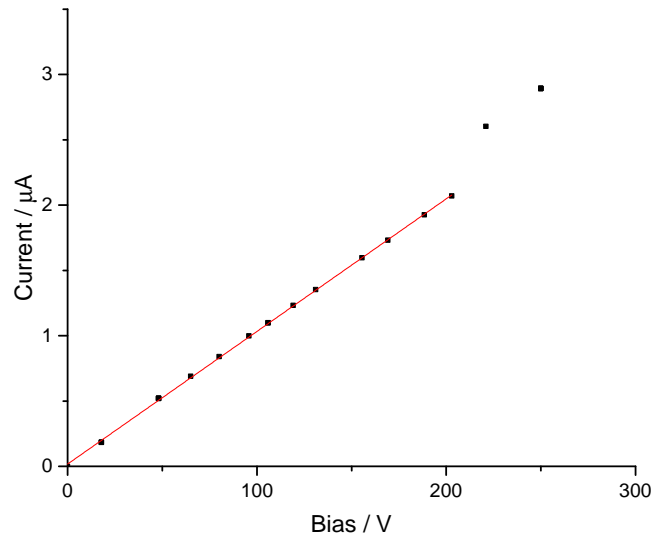


FIGURE 3.21: Linear I/V characteristics of the 100 M Ω resistor. Note the jump in current flow at 200 V bias.

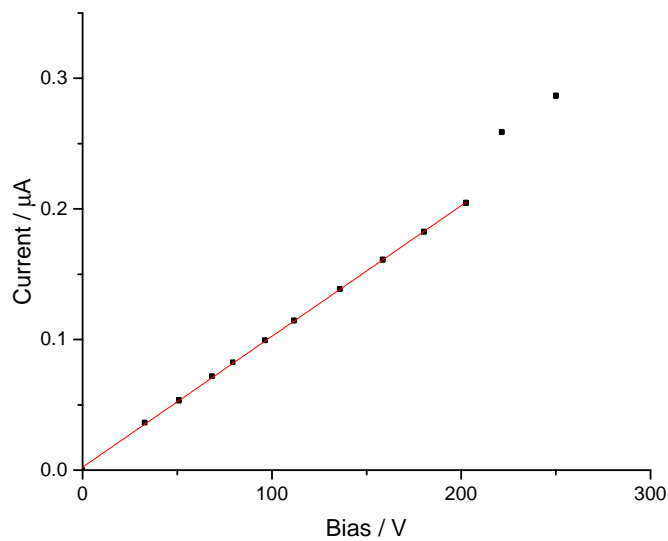


FIGURE 3.22: Linear I/V characteristics of the 1000 M Ω resistor. Note the jump in current flow at 200 V bias..

From the results of these tests, it can immediately be seen that the I/V plot is linear as expected for the constant resistance. On further inspection it can be seen that the linear plots show a small jump at voltages of 200 V in both resistors. A ‘status’ viewer added to the *LabVIEW* program from the *RBD Actuel* software included with the picoammeter also switches from ‘in-range’ to ‘unstable’ or ‘out-of-range’ at these

corresponding voltages, despite still reading currents lower than the maximum allowed by the ammeter. For these reasons, the usable range of the setup was decided as 200 V and is marked by the (red) linear fit on the plots in figures 3.21 and 3.22. Using this range of potentials, the resistances of the resistors were calculated from the slope of the I/V plots. The two resistances were calculated as $98 \pm 1 \text{ M}\Omega$ and $999 \pm 1 \text{ M}\Omega$ for the 100 M Ω and 1000 M Ω resistors respectively. Both of these values land within the 2 % error range of the resistors used, proving functionality of the setup. The CVD grown devices were next tested using this equipment.

Sample A5 (the only device showing rectification) was the first to be tested by the I/V set up. The currents were measured at changing applied bias from -200 V to +200 V with the resulting voltage sweep shown in figure 3.23.

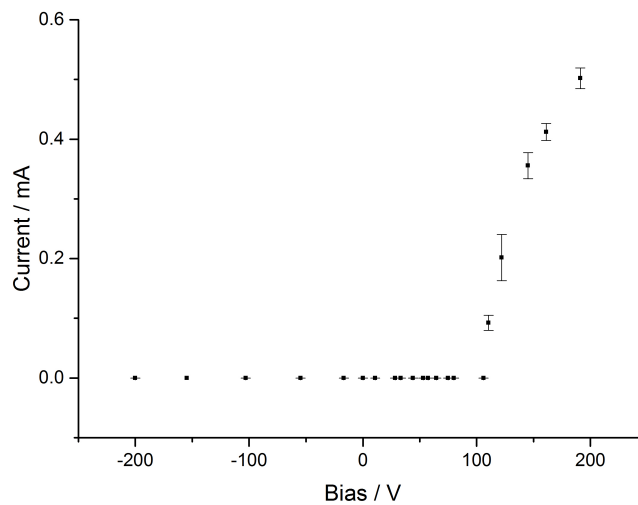


FIGURE 3.23: I/V plot of sample A5 showing rectifying behaviour.

From figure 3.23, sample A5 blocks current in the reverse direction whilst allowing current through the structure in the forward direction. This is as expected from a Schottky diode device. However, the forward direction does not follow the linear path as predicted by Ohm's law. The turn on voltage of sample A5 is also recorded as approximately 100 V which is considerably higher than expected for the diamond diode. The I/V characteristics of the other samples were compared to these unusual findings.

Samples A4 and A8 showed no rectifying behaviour and resulted in linear I/V plots throughout the full bias range with resistances different to those calculated with the multimeter. A8 was still showing a lower resistance than the other devices. However, the calculated resistance of A4 was sufficiently high to discount any surface conduction and so the difference in measurements was attributed to the methods used. The reasons

for the lack of rectifying behaviour in these devices were probably due to deficiencies in the Schottky metal contact to i-diamond. If the O-termination of the diamond surface had become unstable before metal deposition, then the barrier height would have been significantly reduced and hence no rectifying behaviour would be seen. The potential reasons for this are as follows:

1. The large grain sizes of the growth face of the devices may introduce a surface which is too rough for the metal to consistently cover the surface. Any discontinuities in the metal to diamond interface would drastically degrade the workings of the contact by decreasing the barrier height without any visual clues of weakening.
2. The contact wires were often applied multiple times before a secure contact was made to the device. This removal and reattachment of wires may have introduced small silver particulate to the surface of the diamond during the dissolving of the silver conductive paint used. This would limit the proximity of the wire to the metal and result in inaccurate characteristics.

The only feasible way to thoroughly remove all silver particulate from the surface would be through chemical treatments which would also remove the Schottky metals, offering further unwanted complications. These inconsistencies were difficult to address due to the inability to recognise where the faults could lay. As some of the devices were showing the diodic behaviour desired, the method used was able to give the expected results and therefore the discrepancies were attributed to some variation at the metal interface which was not anticipated.

A7 gave the best overall I/V sweep of all devices. This sample showed a linear response in the forward direction with resistance equal to $100\text{ k}\Omega$ and no flowing current under reverse bias up until a breakdown voltage of roughly 75 V . The turn on voltage of this device was calculated as less than 1 V which was closer to the result expected from similar research than the 100 V found in sample A5 [142]. The results for this device are shown in figure 3.24.

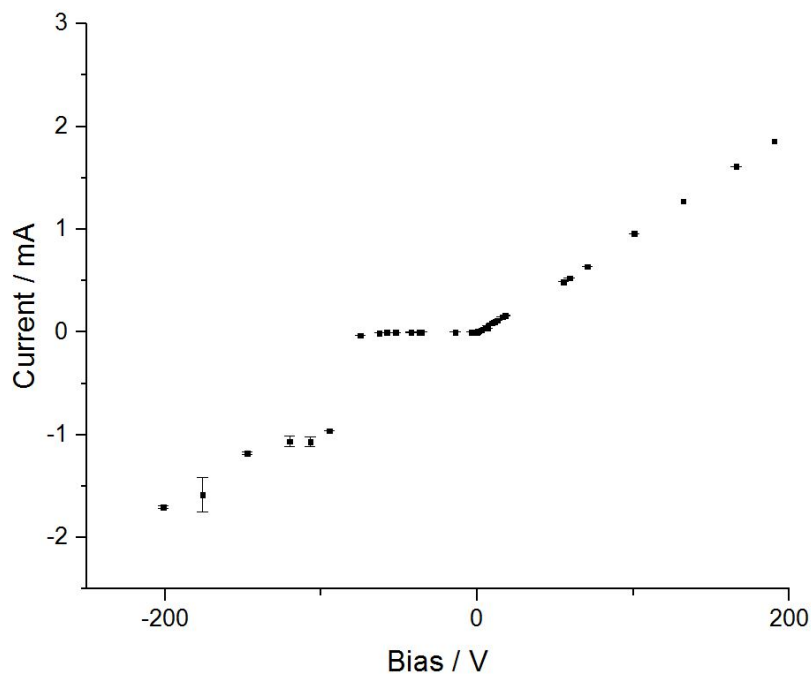


FIGURE 3.24: I/V plot of sample A7 showing rectifying behaviour.

It can be seen that beyond the reverse breakdown voltage of this device, the I/V characteristics follow a similar linear Ohmic path as in the forward direction. This is as predicted for this device as once a voltage greater than that of the breakdown has been passed, the diode is no longer rectifying and acts with a set resistance. The I/V results from this device are closer to those expected of a Schottky diode than for sample A5, although both showed good rectifying behaviour which could fabricate a working betavoltaic battery under beta illumination.

Once characterised, the wire contacts were removed from the BDD layer of the devices and instead attached to the Ni-59 test foil. This metal was placed into the indentation of the window frame structure and again I/V characteristics were measured in air as a calibration for the Ni-63 radioactive foil. The results for this test setup proved to be identical to the results for wires attached to both sides of the devices, showing that the electrical contact between the nickel and the BDD layer was sound. The devices were now analysed under illumination from the Ni-63 foil with a wire attached to the inactive face of the source.

3.3.3 Beta Illumination

The I/V curves of the remaining devices were again tested in air as previously described, but now with addition of the radioactive foil instead of the test piece. Sample A5 which

had previously shown rectifying behaviour (figure 3.23) exhibited an increase in current upon illumination of the beta source. The results of this sample both in and out of beta radiation are shown on the semi-logarithmic plot in figure 3.25.

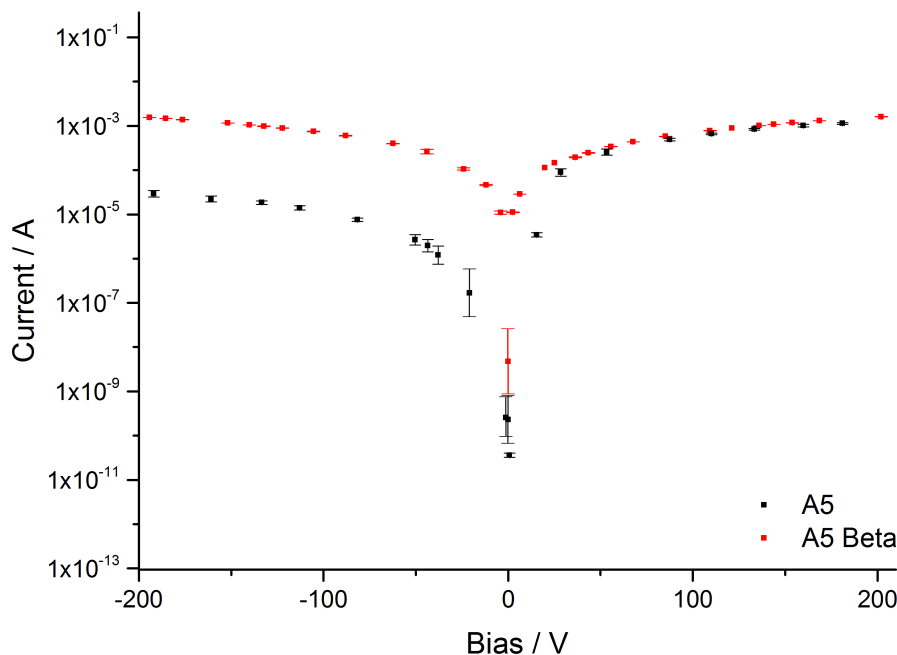


FIGURE 3.25: Semi-logarithmic I/V plot of sample A5, with and without beta illumination. The logarithmic ‘ticks’ on the y-axis were removed as not to clutter the markings.

From figure 3.25, under forward bias the measured currents on addition of the beta source are similar to those of the sample without. Under reverse bias, however, the measured current is regularly two orders of magnitude higher with the addition of a beta source. This sample is showing the characteristics expected from the betavoltaic structure and its characteristics will be assessed further to evaluate its worth as a freestanding battery.

The two samples which showed no diodic character (A4 and A8) again showed no gain upon illumination of the beta particles and followed a linear path as shown for sample A8 in figure 3.26.

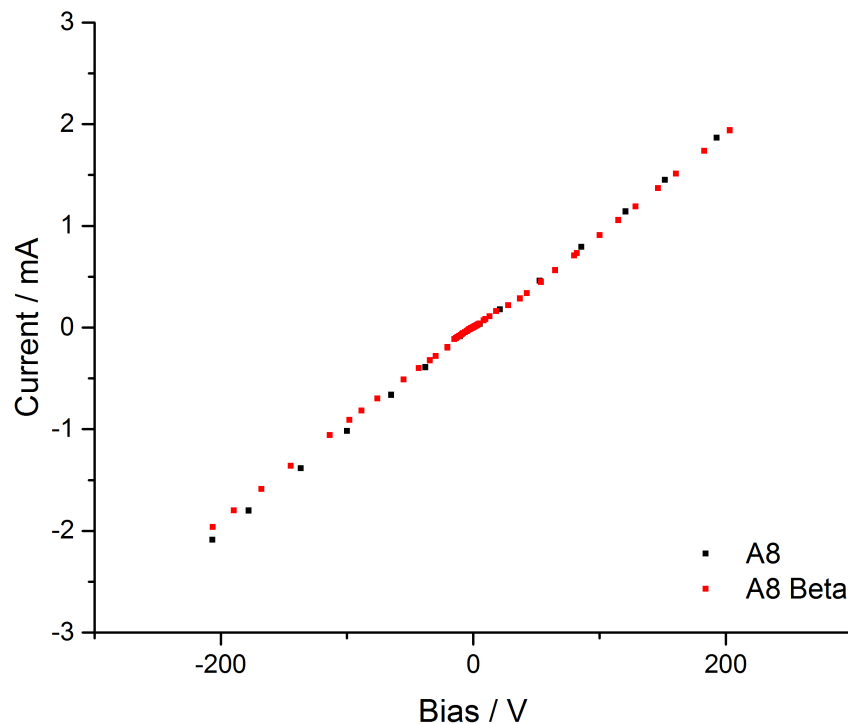


FIGURE 3.26: Linear I/V plot of sample A8, with and without beta illumination.

Sample A8 had the lowest resistance of all devices when measured with the multimeter despite being the thickest i-diamond layer. It was considered that this sample had some sort of superficial contaminants which were allowing surface conduction. In order to test this hypothesis, the silicon frame was broken away from the active region of this device, leaving fragments of freestanding diamond which could have their resistances calculated without any Si surround. The new resistances measured from this sample showed above the maximum resistance of the multimeter in both directions, similar to the majority of the other devices. This conclusively proved the presence of surface conduction around the device which would also explain the linear resistances shown in figure 3.26.

Rather unusually, sample A7 showed a large increase in device resistance when a new set of wire contacts were made to it. The device now only let current of tenths of μA through it under beta illumination at a 200 V bias, compared to all other devices which permit mA. This device had previously given the near perfect rectifying characteristics shown in figure 3.24 and did have the expected high current under large bias. The device now corresponds to a huge resistance of 290 G Ω compared to the 100 k Ω previously recorded. The reason for this increase is unknown. However, many devices showed major inconsistencies on reapplication of the contact wires despite using precisely the same

methods and materials. It was unsure what caused this variation but was attributed to be due to the contact between the wire and Schottky metal.

From the results of all devices under beta illumination, there is one sample which gives the pertinent results (A5) and another which previously showed rectifying behaviour without the source but has had a remarkable increase in resistance on beta illumination (A7). A number of final tests were conducted before the final betavoltaic battery parameters were tested.

Any small air gaps between the beta source and battery structure would result in an energy loss of the primary beta particles before even reaching the structure. By adding the whole device setup to a chamber under vacuum, the physical contact between the source and device could be tested. The results of both rectifying devices (A5 and A7) in and out of vacuum were indistinguishable, concluding that any air gap between the source and device was minimal and did not fundamentally affect the battery structure.

The electron gun was untested and was therefore unable to be used for electron yield calculations of the devices. The method previously considered using the beta source in place of the electron beam was also unable to be utilised. It was calculated that the total current emitted from the beta source used was approximately 2.22 pA, meaning that only 0.1 pA would be emitted through the small aperture in the vacuum setup if the source was mounted on the top plate as previously discussed (section 2.4). The electron yields from the diamond would therefore need to be in the range of 10^3 - 10^4 to have currents detectable above the background electrical noise. The transmissive yields of the samples were expected to be less than five and so this method could not be analysed with the low activity source used. The electron gun mounted to the secondary emission setup had lower electron energies (up to 5 keV) than the beta source but considerably higher currents (μ A), which would have been measurable with the ammeter used if sufficiently configured.

Despite this shortcoming, the open circuit voltage and short circuit current of the two rectifying devices (A5 and A7) were recorded by the multimeter and picoammeter in order to characterise the energy output of the battery. Sample A5 measured an open circuit voltage of 1.5 ± 1 mV which was small but distinguishable from the background value of 4 μ V. The short circuit current was recorded as 0.3 ± 0.1 nA which was close to the laboratory noise levels previously found, but was repeatedly showing this value above the background current at the time of evaluation (10^{-11} A). For sample A7, the open circuit voltage and short circuit current were measured as 40 ± 4 mV and 24 ± 6 nA respectively. The value of this short circuit current is considerably higher than expected for this device. The sample did not have its full voltage sweep measured due to showing high resistances and so no further information could be obtained as to why this value

was so large. This sample could potentially have a large associated capacitance which could be charging from the constant exposure to beta radiation and discharging when measured by the picoammeter. A high short circuit current and low open circuit voltage are common characteristics of a Schottky diode device with large intrinsic region, the devices show this (if not with greater readings than expected) [33]. Regardless, the short circuit current was repeatable and so was taken as valid.

3.4 *CASINO* Simulations

Simulations of the fabricated devices were modelled and analysed in the *CASINO* software to give information on the betavoltaic structure which could not be measured experimentally. The model was built using multiple growth layers through the vertical structure in order to mimic the conditions the primary beta particle would experience on moving through a polycrystalline material. The thicknesses of the i-diamond layers were gradually increased over the device thickness to imitate the increasing grain sizes found as the primary beta particles penetrated through the device. The resulting model was not an accurate representation of the actual material composition in the bulk diamond, but was a better resemblance than that of a perfect, unbroken lattice as conventionally simulated by the program. Even if the polycrystalline nature of the material could be sufficiently modelled in the software, the results from the simulation will never be able to accurately determine the output of the device as attentively as experimental findings and so should only be used as an approximate guide. The simulated electrons are modelled as travelling at a normal to a flat BDD penetration surface. This does not accurately report the wider range of energies and angles emitted from the beta source and roughness of the CVD diamond surface but will help to gain some understanding into the order of dimensions relevant to the betavoltaic design.

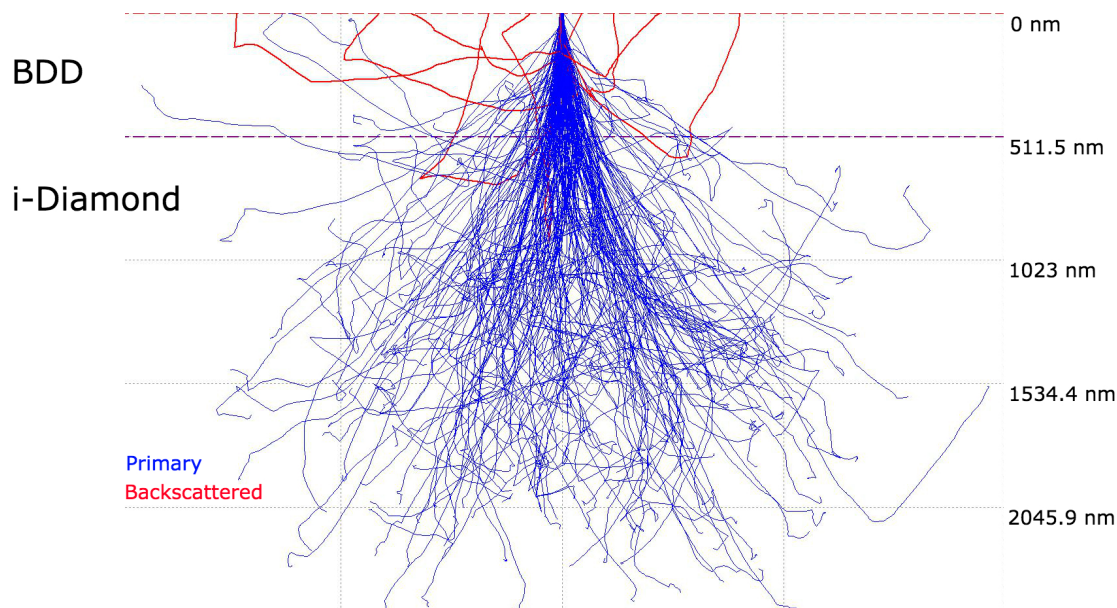


FIGURE 3.27: Simulation of the trajectories of 1000 electrons (with 17.42 keV primary energy) into a model of the betavoltaic device fabricated.

From the simulations at a 17.42 keV primary electron energy (average energy of Ni-63 source), the backscattering coefficient of primary particles was calculated to be approximately $5 \pm 1\%$. This result is small relative to other large band gap semiconducting materials as expected due to the low atomic number of carbon. The maximum penetration depth into the structure at this primary energy was calculated to be $2.2 \pm 0.1 \mu\text{m}$. This depth is similar to as expected from equation 1.5 and corresponds to the primary electron losing all of its energy at a point $1.7 \mu\text{m}$ into the i-layer, considerably shorter than the thickness of the smallest tested device of $35 \mu\text{m}$. The in-built electric field of the Schottky structure may help to pull the primary electrons through the device which cannot be simulated by the program, but it is unlikely that many generated secondaries will make it through the full thickness of the devices.

The primary energy of the beam was subsequently varied over the range emitted from a Ni-63 source (0-66.94 keV) in order to explore the secondary electron generation in the device. The results for the energies giving the highest yields are shown in figure 3.28.

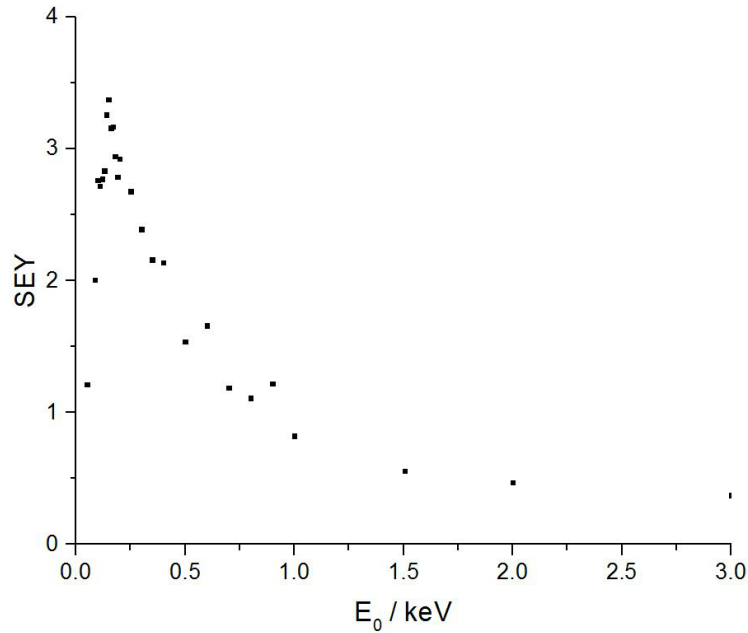


FIGURE 3.28: Simulation results of the variation of RSEY with primary electron energy. The primary energy was increased through the full range of energies emitted from a Ni-63 beta source. The RSEY at a 17.42 keV primary energy was 0.08 ± 0.01 and decreased further on increasing primary energy.

From figure 3.28, the SEY with primary electron beam energy shows the curve expected from section 1.2.11. The maximum reflective yield was found at a primary beam energy of 0.15 keV. Using this result along with those of the 17.42 keV beam, it can be approximated that from the 19.82 eV that the primary particles transfer to create an exciton in polycrystalline diamond, only a small proportion of the transferred energy is given to the secondary electron's energy to escape the bulk (corresponding to moving less than 10 nm). The escape depth of secondary electrons is found to be very small when compared to the large $>35 \mu\text{m}$ active region and so would explain the negligible secondary yield (0.08 ± 0.01) at the average primary energy from the Ni-63 source. A simulation by another group has found that the escape depth of generated secondaries can potentially be as high as 160 nm for microcrystalline diamond [157]. However, this value is still low compared to the device thickness and so either a more penetrative source needs to be used on the existing structures or thinner diamond devices fabricated for use with the Ni-63 source.

3.5 Final Discussion

From both the experimental and computational results for the rectifying devices (A5 and A7), an overall efficiency of the betavoltaic structures could be approximated. The

parameters used are shown in table 3.3 along with their method of calculation.

TABLE 3.3: Parameters required for total efficiency calculation along with their method of computation.

	A5	A7	Source
Short Circuit Current / nA	0.3 ± 0.1	24 ± 6	Experimental
Open Circuit Voltage / mV	1.5 ± 1	40 ± 4	Experimental
Fill Factor / %	50	50	[135]
Backscattering Coefficient / %	5 ± 1	5 ± 1	Simulation
Charge Collection Efficiency / %	95	95	[106]
Exciton Generation Energy / eV	19.82	19.82	[85]

The charge collection efficiency of diamond devices is referenced to be almost unity for large device thicknesses and relatively low average penetrating beta energy (as in the case of this experiment). However, the grain boundaries present in the polycrystalline material may lower this slightly and so the CCE was taken to be 95 % as an appropriate estimate for the fabricated devices [158]. The fact that near the maximum current is met under a small reverse bias supplements this approximation. The fill factor of the devices could not be calculated due to not having the satisfactory I/V characteristics under beta illumination at low voltages. The fill factor of the fabricated devices were both taken to be 50 %. This is lower than recorded in previous experiments but due to the inconsistencies of results on beta illumination, it was expected that this parameter would be low [106]. The self absorbance of the source could also not be calculated as the active thickness of the beta source used was not known. Instead, the source efficiency was taken as unity despite realistically only being a proportion of this.

The total efficiency of both devices were calculated using the product of the device and coupling efficiencies given in equations 1.7 and 1.8. The total efficiencies of samples A5 and A7 were computed as 0.003 % and 0.1 % respectively. These values are very low when compared to other fabricated diamond betavoltaic batteries, which can be mostly attributed to the low open circuit voltage measured across the thick i-diamond layer. The numerous estimations of the parameters in table 3.3 together with the negligence of self absorption of the source will cause the actual efficiencies of the devices to be even lower than those stated.

Despite the low total efficiencies of the fabricated betavoltaic structures, the results conclusively show rectifying behaviour and measurable electrical outputs on illumination of the beta source. The low activity of the source used and the penetration depth of primary electrons being shown as much less than the device thickness are not expected to give values comparable with the most effective betavoltaic structures. Pairing the

fabricated structures with a more penetrative source may drastically increase the efficiency of the comparatively thick devices. Regardless of the low efficiencies, the results from this study have helped the understanding of how a polycrystalline betavoltaic structure should be fabricated. The information gained has been utilised to plan of a more effective betavoltaic structure. This is described in the following section.

3.5.1 Improved Device Design

From previous studies, it has been shown that the optimal thickness for the betavoltaic structure can be computed from the penetration depth of the beta source used. Due to the range of energies emitted from a beta source being weighted to the lower values, the depletion width of the device should be made equal to the penetration depth of the primary beta particles for most efficient collection [159]. This would cause the majority of primary beta particles to lose their energy within the depletion region of the device, generating the maximum number of secondaries in this region which can move through the solid to the rear metal contact of the device. The depletion width of a Schottky structure can be altered by changing the semiconductor doping concentrations, surface terminations and metals used [160]. The depletion width should be maximised using these attributes before being increased to equal the depth of electron penetration by growth of an appropriate i-layer. The thin active regions (2 μm) required for this improvement would introduce difficulties with device manufacture due to the increased delicacy of the diamond layer. This could potentially be minimised by using a lateral semiconducting structure, although the results of such are not as effective as a vertical MiP diode. Merged p-n junction/Schottky devices have been recently studied as a compromise between manufacturing difficulty and device workings but with limited success [78]. For simplicity of design, the vertical MiP structure will again be chosen due its proven ability in betavoltaic structures. However, the structure will be paired with a more penetrative beta source (e.g. Pm-147). This could allow the active region to be made thicker to cope with the higher energy beta particles which are able to penetrate approximately 19 μm into diamond [33].

The first major adjustment to the architecture used should be the substrate material chosen. Silicon has proven to be a fine substrate for high quality CVD diamond growth, but the high conductance of n-type Si relative to the CVD grown BDD has exacerbated the difficulty of promoting charge transport through the active region of the fabricated device. Using undoped silicon substrates would dramatically reduce the likelihood of surface charge transport while still allowing the paramount CVD substrate conditions.

The undoped diamond should still be grown first onto the substrate to minimise the diffusion of boron dopants into the i-layer. Growing a thick undoped layer onto the substrate will increase the effectiveness of the device by decreasing the density of grain boundaries therefore increasing the mobility and diffusion length of any bulk carriers near the surface. The increased grain size will also increase the resistance and lower the impurity concentration in the i-layer which will positively affect the generation of secondary electrons. A thick undoped layer will allow the structure to include the favourable large grain sizes, but the thickness will need to be reduced to allow the secondary electrons to sufficiently escape the structure. The nucleation stages of the i-layer will be removed at a later manufacturing stage to reduce the final active thickness to the appropriate dimension.

The second adjustment to the experimental study would come with the placement of the BDD layer. It is proposed that growing the BDD layer onto the growth layer of the device will give better characteristics for a betavoltaic cell structure. By growing onto the growth face of diamond, the BDD layer will be growing on top of the largest sized grains as opposed to having to nucleate themselves as in the previous design. Microcrystalline BDD grains will be more conductive than the nanocrystalline layer grown in this research and the minimised nucleation layers will reduce the regions of significant carrier recombination [31]. The larger surface roughness of the BDD layer will also limit the backscattering of primary beta particles due to the ‘pyramid structure’ of the CVD diamond surface promoting electron transport towards the bulk.

For growth onto this surface, the boron doping concentration could be lowered from 10^{20} to approximately 10^{18} as this would still allow the electrical conduction and highly doped region for ohmic contact required for the structure, but will minimise the density of scattering due to impurities and allow greater electron penetration. A mask is also suggested to cover the sides of the device during BDD growth in order to reduce the unwanted growth around the sides of the sample. This will limit any surface conduction and avoid the undesirable laser removal of the device edges previously utilised. Growing the BDD onto a planar surface will also minimise the temperature gradients experienced from growing within the frame structure and the full coverage layer could be grown thinner in order to bring the depletion region as close as possible to the beta source. The large $10\text{ mm} \times 10\text{ mm}$ BDD layer will additionally give a larger expanse for metalisation and wire connections, allowing superior contacts to be made.

Once this BDD layer had been grown, the unwanted substrate could now be removed to leave a window frame structure using the laser mill and chemical etch as previously described. Despite the large number of device fractures during this research, the window

frame structure undoubtedly increased the ease of handling throughout the many fabrication stages. Reducing the active region to a smaller dimension (e.g. $3.5 \text{ mm} \times 3.5 \text{ mm}$) for device testing before scaling up for a final cell characterisation would also limit the sample fractures. A smaller active region would negatively reduce the region for beta illumination, but the resulting values could still be characterised for device testing before extrapolating to a larger area for a final structure. Uniform polycrystalline diamond growth over larger active regions is not as complicated as in the case of single crystal diamond and so the device geometry could be scaled up with minimal effort once the optimal conditions had been found. The smaller sized active region on similar sized Si substrates would also allow a larger expanse available for both metal contacts and wire attachment which had proved difficult for the previously fabricated devices.

Once the nucleated face of the i-diamond had been exposed from the chemical etch as in the previous experimental case, an additional laser mill into the nucleated face would be conducted. By milling away the nucleation region of the i-diamond layer, the beta particles travelling vertically through the structure will be subject to higher quality material throughout their passage. Growing the undoped diamond to the same thickness for all devices before etching away different thicknesses will give the varying i-layer thicknesses desired, but now with similar grain sizes. This will allow for more effective analysis between devices due to a greater consistency between layer properties. The milled surface will be smoother than the growth face after cleaning and so will also provide a more stable platform for O-termination of diamond than on the rough growth surface.

The O-termination must be conducted chemically as in the case of the second deposition in this experimental study. This method efficiently cleans all contaminants of the surface which proved very difficult to distinguish at later stages in device testing. The oxidation in a heated solution of $\text{HNO}_3/\text{H}_2\text{SO}_4$ under reflux ensures full surface coverage which is vital for both metalisation and limiting surface conductance. Using the new design with flat BDD layer covering the full area of the Si substrate, ohmic contacts may be deposited onto the devices considerably easier. The metals chosen for both contacts, associated thicknesses and masking setups will be kept constant, owing to giving the best results from the literature (sections 1.2.7 and 1.2.8). The ohmic contacts should be first deposited onto each corner of the BDD layer leaving the active region clear, with a metalised area larger than previously deposited in order for wire contacts to be made. Despite a contact to the rear of the beta source being sufficient for the experimental device, soldering a thin wire onto Ti/Au contacts has been shown to give low, linear electrical resistances over a far greater range than that of the initial experimental arrangement [79]. The ohmic contacts can now be annealed to ensure consistent carbide formation over the larger area. The Schottky contact metals should be deposited into the O-terminated

diamond within the cutout of the device. Deposition of the Schottky metal onto the nucleation face of the structure has also proven to give better rectification due to the added stability of the O-termination [161]. After a final ozone treatment in a Jelight UVO cleaner to passivate the surface, wires should be soldered onto both top and bottom contacts. This permanent fixture will limit the inconsistencies found with reapplication of the silver conductive paint discovered throughout the research.

Finally, the beta source can be placed onto the flat BDD surface for penetration through the active region. The source will no longer sit within the frame cutout but will have the added benefits associated with penetrating into a high quality region as well as less backscattering. The styrene sample holder with cut foam used for device testing could be altered for this new setup and could again provide the crucial contact between beta source and BDD layer.

Chapter 4

Conclusion

4.1 Summary

The principal aim of the project was to design and manufacture a working betavoltaic battery using CVD grown polycrystalline diamond. The thickness of the intrinsic region of the betavoltaic structure used was adjusted to investigate how this layer affected the overall performance of the battery. The MiP structure was selected in order to maximise the number of secondary electrons generated within the device by positioning the depletion region as close as possible to the electron penetration face. Ni-63 was chosen as the beta source as this is a pure beta emitter with long half life and maximum energy below the radiation limit of diamond ($>MeV$) [143]. Considerable analysis of the grown diamond layers was conducted under an optical microscope, Raman spectrometer and SEM in order to assess how any inhomogeneity in the diamond film would affect the electrical output of the device. This was vital, as once the device had been assembled, there was no way of accessing the central layers of the structure for further clarification.

Two of the seven constructed devices were able to be electrically tested as a standalone battery when paired with the Ni-63 beta source. The remaining diamond structures were disregarded throughout the experiment, predominantly due to the breakages of the active layers or poor Schottky metal junctions. This must clearly be improved for the method used to become effective and accurate. Despite the high failure rate, the open circuit voltage and short circuit current of the most potent device was measured as 40 ± 4 mV and 24 ± 6 nA. The value of this short circuit current is remarkably high, possibly higher than the current achievable by secondary electron generation alone from the beta source. This suggests that there may be some other activity within the battery (possible capacitance) which was causing these large readings. This was not addressed during this

project due to lack of experimental time available, but the sample has been donated to Dr Neil Fox in the University of Bristol School of Physics for further investigation.

Computational experiments were conducted using Monte Carlo simulations in the *CASINO* software in order to gain information on how the electrons emitted from the beta source react on entering the device. The results of the simulation showed that the particles emitted from the source will only travel approximately 2 μm into the polycrystalline material before losing all of their energy. The thickness of the active region should therefore be made of a similar thickness in order for the maximum number of generated electrons to be measured by the device. This outcome was discovered too far into the manufacturing process to scale to this dimension of grown diamond. Additionally, the thinnest fabricated devices were fractured during construction and could not be tested. The smallest active layer of a tested device was 35 μm . This thickness will have obviously depleted the results of the battery device when paired with a Ni-63 source, but could possibly function well if utilised with a more penetrative source.

The overall efficiency of the most effective device was calculated as 0.1 %, which is lower than that shown by similar experiments, but shows the capability and effectiveness of using polycrystalline diamond in electronic devices as a lower cost alternative to single crystal diamond [106]. This efficiency is low primarily due to the low open circuit voltage recorded giving a small internal efficiency of the semiconductor. It is this value which will need to be improved in order to increase the overall efficiency of device as the CCE is already approaching unity. However, it must be remembered that even a small efficiency of a betavoltaic battery can produce an energy output comparable to the most efficient chemical batteries. Therefore, the effective use of this device may still be workable for nanoelectronic applications [142].

This research and laboratory work successfully constructed a working polycrystalline battery structure as proposed. However, due to a high number of device failures (>70 %), the outcome from the varying i-diamond thickness could not be fully ascertained. The most positive results from this research came largely in the form of information showing how the structure could be improved. A full explanation of how the diamond device would be fabricated for further analysis is shown in section 3.5.1, but a number of additional experimental procedures could also be developed in order to gain additional results for the devices.

4.2 Future Work

Experimentally calculate critical parameters

A fundamental route of future work would be to calculate the critical parameters of the device throughout the course of structure construction. Considerable characterisation of the CVD grown layers were managed throughout this research, but little consideration was taken into the electrical characteristics. Most importantly, the Schottky barrier height and depletion region width were not calculated in this research and it is these parameters which fundamentally determine the electrical output of the structure. Rather than assuming that the devices incorporated the values found in the literature, actually determining them for each sample would dramatically increase the understanding of the structure and would help to ascertain where any discrepancies or faults may lie. Although the calculation of these parameters may not be exact from the simulations or approximations in the methods used, the results will assist in discovering the range at which the true value lies. This will limit any major discrepancies in the optimal values and fabricated device (e.g. as shown in the data when assessing the i-diamond thickness). By manufacturing a number of samples based around the calculated values, the user will have a far greater opportunity of manufacturing a highly effective battery.

The Schottky barrier height can be calculated by measuring the capacitance at varying reverse voltage [160]. This could be simply conducted as an extension to the I/V characterisation and would be another effective test into the rectification ability of devices. An approximate width of the depletion region can be calculated from a relationship dependant on the Schottky barrier height, material dopant concentration and dielectric constant [33]. The optimal geometry of the devices can then be calculated for a chosen beta source using *CASINO* electron penetration simulations and the calculated depletion width.

Addition of a magnet

A further development, which may positively affect the electrical output of the device, could be to pair the betavoltaic structure with a hollowed cylindrical magnet. The addition of the magnet will apply a magnetic field perpendicular to the penetrative face of the structure which will exert a force on any primary electron not travelling parallel to this. This will cause the electrons path to follow a spiraling cycloidal path towards the betavoltaic device. The penetration depth of a primary electron is commonly approximated to be half of the actual stopping range of the particle as most beta particles will not travel parallel to the thickness of the material [33]. Adding a magnet could accelerate the primary particles towards the structure, increasing the penetration depth and potentially exciting a greater number of useful secondary electrons that will positively affect the output of the battery.

Hybrid batteries

An adapted use for betavoltaic batteries has also been developed which uses the continuous current of a betavoltaic battery to ‘trickle’ charge a secondary Li-ion battery over periods of inactivity [33]. This hybrid battery method merges the long lifetime of betavoltaic batteries with the higher power of chemical cells. This method can only be utilised in applications which require intermittent power, but could potentially be an application where a betavoltaic battery’s key attributes are most effectively exploited.

Betavoltaic nanowires

Another possible (but significantly more difficult) area of future research would be to look into constructing the betavoltaic device from vertical semiconducting nanowires. This would improve the carrier collection, reduce electron reflection and provide a structure less sensitive to impurities [122]. This research has been previously explored in photovoltaic applications to increase the coupling efficiency of the device and owing to the similarities of betavoltaic batteries and solar cells in operation, it is expected that a similar increase could be possible in betavoltaic applications. A recent study into manufacturing 1D betavoltaic nanowires has shown the potential effectiveness of this method, documenting a significant conversion efficiency of 27.92 % and an open circuit voltage of 2.74 V [162].

C-14 battery

A further suggestion of future study with diamond betavoltaic batteries would be to incorporate C-14 into the fabricated device. C-14 has both a longer half life and larger average beta energy than Ni-63, but the main benefit of using carbon 14 is its ability to be used for growing the diamond structure itself. If a C-14 containing gas could be introduced to a CVD reactor to grow the diamond diode structure, then the betavoltaic device would not require an external beta source and could essentially provide its own power. The carbon 14 could also potentially be extracted from the huge number of graphite control rods from disused fission reactors. This would limit the difficulty in effective disposal of radioactive waste, as the radioactive C-14 could be enclosed within non-radioactive C-12 diamond, sealing the emitted beta particles and making the structure safe to handle. The fabricated structure could also be designed so that the depletion region of the device was in all directions about the radioactive C-14. This would allow all of the emitted primary electrons to be collected from the source rather than just those from the active face as shown in this research. Unfortunately, over time the C-14 will decay into nitrogen which may contaminate and degrade the quality of the diamond lattice- limiting the batteries long term use. Further research into the effects of this degradation are required. If the workings of a C-14 diamond battery were shown to maintain the highest efficiency throughout the lifetime of the C-14 source, this device may provide the breakthrough needed to make betavoltaic batteries more employable for areas where chemical batteries are ineffective.

Appendix A

BDD Layer Trial

After the growth time of the first sample was complete, it was removed from the chamber and tested using Raman spectroscopy, two point resistance measurements with a multimeter and SEM imaging in order to test the quality and coverage of the boron doped layer. The Raman spectrum was almost identical to that previously recorded for the nucleation face of this sample and showed no peak shifting or broadening as conventionally seen in boron doped diamond. The BDD layer grown was probably too thin to show any difference to the spectrum and so the result was inconclusive. The two point resistance showed a considerably lower value than for the undoped diamond (Ω instead of $M\Omega$) as expected but varied dramatically during repeats due to the poor contact of the probes to the surface, predominantly due to the lack of force placed onto the sample for fear of fracture. The samples were introduced to the SEM to more conclusively determine if a sufficient boron doped layer had been grown.

The sample which had had the 30 minute growth (A5) was entered to the SEM chamber alongside a sample with no boron doping (A3). Silver conductive paint was used to mount the samples into the holder and also to contact the nucleation face to the substrate holder in order to limit the amount of surface charging. By examining how the surfaces reacted upon radiation of the electron beam moving away from the conductive paint, an idea on the surface conductivity of the two samples could be obtained. Differences in the crystal morphologies were also expected to be noted at higher magnifications. A blind test was conducted in order to see if any major differences of the two samples could be identified from their behaviour under the electron beam. A relatively high beam energy of 15 keV was chosen in order to exaggerate any charging, the results of the blind trial are presented below.

The first sample under electron illumination was found to charge substantially at any considerable distance from the silver conductive paint. Under higher magnification, there

was also no obvious continuous BDD layer noted from the crystal morphologies. SEM images of this face near to the conductive paint are shown in figure A.1.

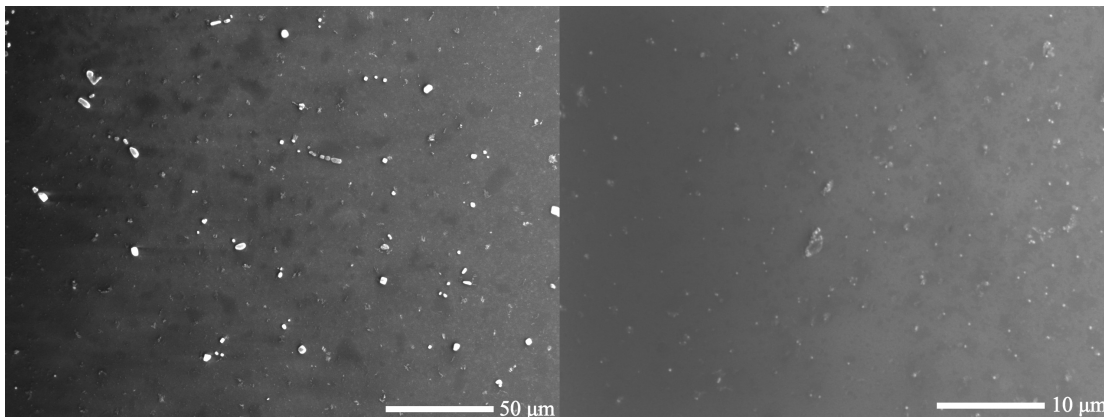


FIGURE A.1: SEM images of sample A3. The sample had been previously fractured but could still be analysed under a SEM. Beam energy = 15 keV, magnification left = 500 \times , magnification right = 2500 \times .

The second sample charged considerably less than the first on moving the beam away from the silver paint. Under a similar magnification to the first sample, substantially more crystals can be seen about the surface. The second sample could retain focus at a higher magnification than the first and can conclusively show crystal growth on the surface, but still show some inconsistency over the full area. The results for the second sample are shown in figure A.2.

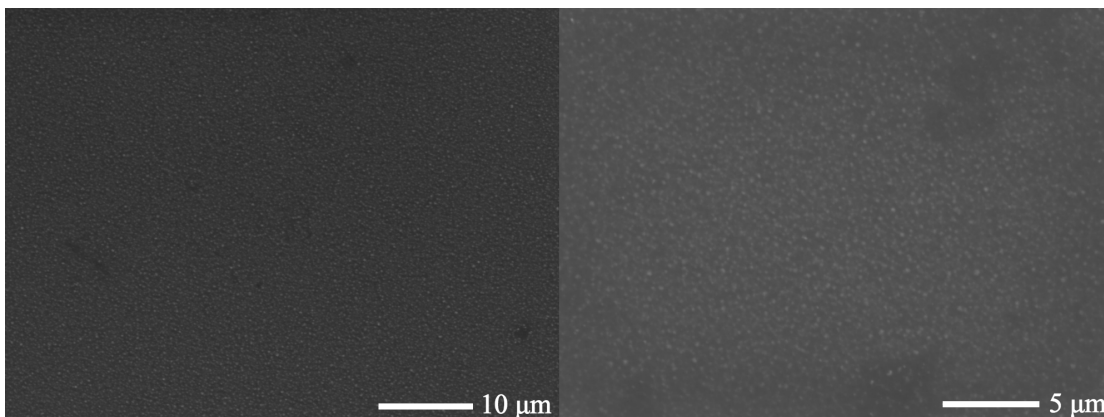


FIGURE A.2: SEM images of sample A5. Beam energy = 15 keV, magnification left = 2200 \times , magnification right = 4500 \times .

The second sample was in fact the boron doped sample as expected from the results of the SEM tests. However, due to fear of not having a uniform film of BDD, sample A5 (the sample with a boron doped layer) was re-entered to the HFCVD chamber and another 30 minutes of growth was conducted. All other samples were introduced to the CVD chamber individually for a full hour's BDD growth to get all samples to the same

point. Again the resulting samples were tested by Raman, two point probe resistance and SEM. The Raman spectra still showed no considerable differences to those previously examined due to the thinness of the BDD layer. The resistance tests showed again less than the undoped diamond but the fluctuations were still so great that no stable results could be taken.

On inspection of the hour long boron doped samples in the SEM, it was obvious to make out the grains of the grown BDD layer but proved hard to focus at high magnification. There was still conclusive results that a nanocrystalline BDD film was present and the betavoltaic structure could hence move onto its next processing stage.

Bibliography

- [1] W.J. Hershey. *The Book of Diamonds*. Kessinger Publishing Co, 2004.
- [2] V. Blank, M. Popov, G. Pivovarov, N. Lvova, K. Gogolinsky, and V. Reshetov. Ultrahard and superhard phases of fullerite C60: Comparison with diamond on hardness and wear. *Diamond and Related Materials*, 7(2-5):427–431, 1998.
- [3] R.T. Coelho, S. Yamada, D.K. Aspinwall, and M.L.H. Wise. The application of polycrystalline diamond (PCD) tool materials when drilling and reaming aluminium based alloys including mmc. *International Journal of Machine Tools and Manufacture*, 35(5):761–774, 1995.
- [4] H. Pierson. *Handbook of Carbon, Graphite, Diamond, and Fullerenes: Properties, Processing, and Applications*. Noyes Publications, 1993.
- [5] F.P. Bundy. The P , T phase and reaction diagram for elemental carbon, 1979. *Journal of Geophysical Research*, 85(B12):6930, 1980.
- [6] J. Robertson. Diamond-like amorphous carbon. *Materials Science and Engineering: R: Reports*, 37(4-6):129–281, 2002.
- [7] N. Setaka, B. Lux, K.E. Spear, K.V. Ravi, and J.P. Dismukes. *Proceedings of the Third international symposium on Diamond Materials*. Electrochemical Society, 3 edition, 1993.
- [8] J. Filik. *Fundamental Studies on the Deposition and Characterisation of Novel Diamond-like Materials*. PhD thesis, University of Bristol, 2006.
- [9] R. Vaz. *Studies of the secondary electron emission from diamond films*. PhD thesis, University of Bristol, 2013.
- [10] J. E. Shigley. High-pressure-high-temperature treatment of gem diamonds. *Elements*, 1(2):101–104, 2005.
- [11] R.M. Hazen. *The Diamond Makers*. Cambridge Univ. Press, 1 edition, 2000.

- [12] M. Prelas. *Handbook of industrial diamonds and diamond films*. Marcel Dekker, 1 edition, 1998.
- [13] B. Sun, X. Zhang, and Z. Lin. Growth mechanism and the order of appearance of diamond (111) and (100) facets. *Physical Review B*, 47(15):9816–9824, 1993.
- [14] P. W. May. Diamond thin films: A 21st-century material. *Philosophical Transactions of the Royal Society A: Mathematical, Physical and Engineering Sciences*, 358(1766): 473–495, 2000.
- [15] S. Matsumoto, Y. Sato, M. Kamo, and N. Setaka. Vapor deposition of diamond particles from methane. *Japanese Journal of Applied Physics*, 21(Part 2, No. 4): L183–L185, 1982.
- [16] L. Regel and W. Wilcox. Diamond film deposition by chemical vapor transport. *Acta Astronautica*, 48(2-3):129–144, 2001.
- [17] B. Dischler and C. Wild. *Low-Pressure Synthetic Diamond*. Springer Berlin, 1 edition, 2013.
- [18] J. Cifre, F. Lopez, J.L. Morenza, and J. Esteve. Analysis of contamination in diamond films by secondary ion mass spectroscopy. *Diamond and Related Materials*, 1(5-6):500–503, 1992.
- [19] V. Srikanth and X. Jiang. Synthesis of diamond films. *Synthetic Diamond Films*, pages 21–55, 2011.
- [20] N. Ali and S. Zhang. *Nanocomposite thin films and coatings: Processing, properties and performance*. Imperial College Press, 2007.
- [21] T. Ito and T. Teraji. Homoepitaxial diamond growth by high-power microwave-plasma chemical vapor deposition. *Journal of Crystal Growth*, 271(3-4):409–419, 2004.
- [22] Y. Mankelevich and P. May. From ultrananocrystalline diamond to single crystal diamond growth in hot filament and microwave plasma-enhanced CVD reactors: A unified model for growth rates and grain sizes. *The Journal of Physical Chemistry C*, 112(32):12432–12441, 2008.
- [23] H. Wilson, D.U. Wiechert, F. Picht, D. Leers, H. Lade, H. Hagemann, and P.K. Bachmann. Diamond chemical vapor deposition: Gas compositions and film properties. *MRS Proceedings*, 339, 1994.
- [24] N.G. Ferreira, M.R. Baldan, A.F. Azevedo, and W.M. Silva. Growth parameters optimization to synthesize CVD diamond through graphite etching. *INPE*, 28: 45–49, 2009.

- [25] A. Cheesman. *Investigations into the fundamentals of gas-phase and gas-surface chemistry prevalent in growth of Chemical Vapour Deposited diamond films*. PhD thesis, University of Bristol, 2006.
- [26] N.A. Fox, W.N. Wang, K.R. Hallam, M.N.R. Ashfold, J.C. Stone, and P.W. May. The effect of diamond surface termination species upon field emission properties. *Diamond and Related Materials*, 7(2-5):671–676, 1998.
- [27] S.J. Harris. Mechanism for diamond growth from methyl radicals. *Applied Physics Letters*, 56(23):2298, 1990.
- [28] P.W. May, W.J. Ludlow, M. Hannaway, P.J. Heard, J.A. Smith, and K.N. Rosser. Raman and conductivity studies of boron-doped microcrystalline diamond, faceted nanocrystalline diamond and cauliflower diamond films. *Diamond and Related Materials*, 17(2):105–117, 2008.
- [29] J.A. von Windheim, V. Venkatesan, D.M. Malta, and K. Das. Comparison of the electric properties of single-crystal and polycrystalline diamond by hall effect and capacitance-voltage measurements. *Diamond and Related Materials*, 2(5-7):841–846, 1993.
- [30] J. Graebner. Thermal conductivity of diamond films. *Journal of Wide Bandgap Materials*, 7(2):105–118, 1999.
- [31] E. Lipatov, D. Genin, D. Grigorev, and V. Tarasenko. Recombination radiation in the diamond. *Luminescence - An Outlook on the Phenomena and their Applications*, 2016.
- [32] A. Genis, W. Dromeshauser, and R. Linares. Enhanced diamond polishing, 2007.
- [33] T. Alam and M. Pierson. Principles of betavoltaic battery design. *Journal of Energy and Power Sources*, 3(1):11–41, 2016.
- [34] S. Kulesza, J.K. Patyk, M. Daenen, O.A. Williams, W. Van de Putte, J. Fransaer, K. Haenen, and M. Nesldek. Structural investigations of protective polycrystalline diamond coatings on titanium substrates. *Surface and Coatings Technology*, 201(1-2):203–207, 2006.
- [35] M.N.R. Ashfold, K.N. Rosser, S.R.J. Pearce, P.W. May, and J. Petherbridge. Molecular beam mass spectrometry investigations of low temperature diamond growth using CO₂/CH₄ plasmas. *Diamond and Related Materials*, 10(3-7):393–398, 2001.

- [36] J. A. Carlisle, O. Auciello, J. E. Gerbi, J. Birrell, and X. Xiao. Low temperature growth of ultrananocrystalline diamond. *Journal of Applied Physics*, 96(4):2232, 2004.
- [37] A. Gicquel, W.D. Brown, and J.L. Davidson. *Diamond materials: Proceedings of the sixth international symposium*. Electrochemical Society, 2000.
- [38] H. Noguchi. Base material for growing single crystal diamond and method for producing single crystal diamond substrate, 2013.
- [39] 2017. URL <http://e6cvd.com/uk/application/all.html>.
- [40] A.J. Tessmer, K. Das, and D.L. Dreifus. Polycrystalline diamond field-effect transistors. *Diamond and Related Materials*, 1(2-4):89–92, 1992.
- [41] T. Nuno, S. Okamoto, K. Nakajima, S. Tanaka, N. Shibuya, K. Okamoto, T. Nam-mori, and H. Itoh. Cast polycrystalline silicon solar cell with grooved surface. *IEEE Conference on Photovoltaic Specialists*, 1990.
- [42] P. Ascarelli and S. Fontana. Dissimilar grit-size dependence of the diamond nucleation density on substrate surface pretreatments. *Applied Surface Science*, 64(4):307–311, 1993.
- [43] T. Muto, T. Kimura, T. Kanai, and S. Yugo. Generation of diamond nuclei by electric field in plasma chemical vapor deposition. *Applied Physics Letters*, 58(10):1036, 1991.
- [44] P. Fallon, L. M. Brown, R. L. Woodin, and J. E. Butler. Thin film diamond growth mechanisms [and comment]. *Philosophical Transactions of the Royal Society A: Mathematical, Physical and Engineering Sciences*, 342(1664):209–224, 1993.
- [45] J.J. Cuomo, C.R. Guarnieri, S.J. Whitehair, J.C. Tsang, R.I. Fuentes, and J.E. Yehoda. Enhanced nucleation and growth of diamond on sic by plasma enhanced chemical vapor deposition using thin metal films. *Applied Physics Letters*, 60(23):2865–2867, 1992.
- [46] C. Huitle and E. Brillas. *Synthetic diamond films: Preparation, electrochemistry, characterization, and applications*. John Wiley & Sons, 2011.
- [47] C. Shi and T. Hao. Study on enhancement of diamond nucleation on fused silica substrate by ultrasonic pretreatment. *Diamond and Related Materials*, 13(3):465–472, 2004.
- [48] I. Lin, N. Tai, K. Leou, and C. Dong. Bias-enhanced nucleation and growth processes for ultrananocrystalline diamond films in ar/CH₄ plasma and their

- enhanced plasma illumination properties. *ACS Applied Materials & Interfaces*, 6 (13):10566–10575, 2014.
- [49] B. R. Stoner, G.-H. M. Ma, S. D. Wolter, and J. T. Glass. Characterization of bias-enhanced nucleation of diamond on silicon by in vacuo surface analysis and transmission electron microscopy. *Physical Review B*, 45(19):11067–11084, 1992.
- [50] S. D. Wolter, M. T. McClure, J. T. Glass, and B. R. Stoner. Bias-enhanced nucleation of highly oriented diamond on titanium carbide (111) substrates. *Applied Physics Letters*, 66(21):2810–2812, 1995.
- [51] J. Wilks and E. Wilks. *Properties and applications of diamond*. Butterworth-Heinemann, 1 edition, 1994.
- [52] J. E. Field, M. C. Payne, C. J. Pickard, and R. H. Telling. Theoretical strength and cleavage of diamond. *Physical Review Letters*, 84(22):5160–5163, 2000.
- [53] M.C. Salvadori, W.W.R. Araujo, F.S. Teixeira, M. Cattani, A. Pasquarelli, E.M. Oks, and I.G. Brown. Termination of diamond surfaces with hydrogen, oxygen and fluorine using a small, simple plasma gun. *Diamond and Related Materials*, 19(4): 324–328, 2010.
- [54] L. Ley, J. Ristein, and F. Maier. Electron affinity of plasma-hydrogenated and chemically oxidized diamond (100) surfaces. *Physical Review B*, 64(16), 2001.
- [55] Y. Hishikawa, S. Motojima, H. Iwanaga, T. Hashishin, and Y. Furuya. Interaction of hydrogen with carbon coils at low temperature. *Carbon*, 42(2):331–335, 2004.
- [56] L. Schlapbach, P. Aebi, O.M. Kuttel, and L. Diederich. Electron affinity and work function of differently oriented and doped diamond surfaces determined by photoelectron spectroscopy. *Surface Science*, 418(1):219–239, 1998.
- [57] C. Van Haesendonck, K. Haenen, W. Deferme, G. Bogdan, C. Toma, and A. Volodin. Electrostatic force microscopy study of electrical conductivity of hydrogen-terminated CVD diamond films. *physica status solidi (a)*, 204(9):2915–2919, 2007.
- [58] P. K. Baumann. Comparison of electron affinity and schottky barrier height of zirconium and copper-diamond interfaces. *Journal of Vacuum Science & Technology B: Microelectronics and Nanometer Structures*, 15(4):1236, 1997.
- [59] T. Teraji, Y. Garino, Y. Koide, and T. Ito. Low-leakage p-type diamond schottky diodes prepared using vacuum ultraviolet light/ozon treatment. *Journal of Applied Physics*, 105(12):126109, 2009.

- [60] N. Tokuda, H. Umezawa, S. Ri, K. Yamabe, H. Okushi, and S. Yamasaki. Roughening of atomically flat diamond (111) surfaces by a hot HNO₃/H₂SO₄ solution. *Diamond and Related Materials*, 17(4-5):486–488, 2008.
- [61] A. R. Lubinsky, D. E. Ellis, and G. S. Painter. Ab initio calculation of the electronic structure and optical properties of diamond using the discrete variational method. *Physical Review B*, 4(10):3610–3622, 1971.
- [62] I. Vlasov and E. Ekimov. On the origin of the raman scattering in heavily boron-doped diamond. *Condensed Matter - Materials Science*, 38, 2008.
- [63] P. R. Briddon, R. J. Eyre, and J. P. Goss. Theoretical models for doping diamond for semiconductor applications. *physica status solidi (b)*, 245(9):1679–1700, 2008.
- [64] H. Okushi, Y. Chen, S. Ri, H. Kato, and T. Makino. Electrical characterization of homoepitaxial diamond pn+ junction. *Diamond and Related Materials*, 14(11-12):1995–1998, 2005.
- [65] E.A. Ekimov and V.A. Sidorov. Superconductivity in diamond. *Diamond and Related Materials*, 19(5-6):351–357, 2010.
- [66] P. Bergonzo, J. Chevallier, F. Jomard, C. Mer, N. Habka, and J. Barjon. Resistivity of boron doped diamond. *Physica Status Solidi (RRL) - Rapid Research Letters*, 3(6):202–204, 2009.
- [67] J. Esteve, J. Cifre, G. Sanchez, M. C. Polo, and W. L. Wang. Internal stress and strain in heavily boron-doped diamond films grown by microwave plasma and hot filament chemical vapor deposition. *Journal of Applied Physics*, 80(3):1846, 1996.
- [68] D. Wu, Y. C. Ma, Z. L. Wang, Q. Luo, C. Z. Gu, N. L. Wang, C. Y. Li, X. Y. Lu, and Z. S. Jin. Optical properties of boron-doped diamond. *Physical Review B*, 73(1), 2006.
- [69] I. Sakaguchi, M. N.-Gamo, Y. Kikuchi, E. Yasu, H. Haneda, T. Suzuki, and T. Ando. Sulfur: A donor dopant for n-type diamond semiconductors. *Physical Review B*, 60(4):R2139–R2141, 1999.
- [70] R. Car, J. Bernholc, A. Antonelli, and S. A. Kajihara. Nitrogen and potential n-type dopants in diamond. *Physical Review Letters*, 66(15):2010–2013, 1991.
- [71] P. Koidl, R. Locher, C. Wild, R. Brenn, C. Haug, and R. Samlenski. Characterisation and lattice location of nitrogen and boron in homoepitaxial CVD diamond. *Diamond and Related Materials*, 5(9):947–951, 1996.

- [72] S. Koizumi. Growth and characterization of phosphorus doped n-type diamond thin films. *physica status solidi (a)*, 172(1):71–78, 1999.
- [73] R. Li, X. Hu, H. Shen, and X. He. Co-doping of sulfur and boron in CVD-diamond. *Materials Letters*, 58(12-13):1835–1838, 2004.
- [74] S. C. Eaton, Yu. E. Evstefeeva, J. C. Angus, A. B. Anderson, and Yu. V. Pleskov. Sulfur-doped n-type diamond: Preparation and electrochemical properties. *Russian Journal of Electrochemistry*, 39(2):154–159, 2003.
- [75] A. Kitai. *Principles of solar cells, LEDs and diodes*. Wiley, 1 edition, 2012.
- [76] E. Abiri, M. Salehi, S Kohan, and M Mirzazadeh. Multi-application pin diode. *2010 Second Pacific-Asia Conference on Circuits, Communications and System*, 2010.
- [77] A.V. Shah, R. Platz, and H. Keppner. Thin-film silicon solar cells: A review and selected trends. *Solar Energy Materials and Solar Cells*, 38(1-4):501–520, 1995.
- [78] M. Kubovic, H. El-Hajj, J.E. Butler, and E. Kohn. Diamond merged diode. *Diamond and Related Materials*, 16(4-7):1033–1037, 2007.
- [79] A. Traoré. *High power diamond Schottky diode*. PhD thesis, Université Grenoble Alpes, 2014.
- [80] B. L Sharma. *Metal semiconductor schottky barrier junctions and their applications*. Plenum Press, 1 edition, 1984.
- [81] R.T. Tung. Formation of an electric dipole at metal-semiconductor interfaces. *Physical Review B*, 64(20), 2001.
- [82] R.S. Sussmann. *CVD diamond for electronic devices and sensors*. Wiley, 1 edition, 2009.
- [83] T. Tachibana, B. E. Williams, and J. T. Glass. Correlation of the electrical properties of metal contacts on diamond films with the chemical nature of the metal-diamond interface. ii. titanium contacts: A carbide-forming metal. *Physical Review B*, 45(20):11975–11981, 1992.
- [84] M. Werner. Diamond metallization for device applications. *Semiconductor Science and Technology*, 18(3):S41–S46, 2003.
- [85] Q. Wu. *Measurements and studies of secondary electron emission of diamond amplified photo cathode*. Indiana University, 1 edition, 2008.

- [86] A. Feldman. *Applications of diamond films and related materials*. The Institute, 1 edition, 1995.
- [87] P. Muret, A. Traoré, A. Maréchal, D. Eon, J. Pernot, J. C. Pinero, M. P. Villar, and D. Araujo. Potential barrier heights at metal on oxygen-terminated diamond interfaces. *Journal of Applied Physics*, 118(20):204–505, 2015.
- [88] J. Howard, W. Rosenberg, and J. White. Schottky barrier contact and methods of fabrication thereof, 1977.
- [89] A. Fiori, T. Teraji, and Y. Koide. Thermal stabilization and deterioration of the wc/p-type diamond (100) schottky-barrier interface. *physica status solidi (a)*, 211(10):2363–2366, 2014.
- [90] T. Makino, S. Tanimoto, Y. Hayashi, H. Kato, N. Tokuda, and M. Ogura. Diamond schottky-pn diode with high forward current density and fast switching operation. *Applied Physics Letters*, 94(26):262101, 2009.
- [91] Y. Sundarasaradula and P. Sodhgam. Temperature dependence of electrical characteristics on pn junction power diodes irradiated by x-ray. *2012 9th International Conference on Electrical Engineering/Electronics, Computer, Telecommunications and Information Technology*, 2012.
- [92] J. Butler, M. W. Geis, K. E. Krohn, J. Lawless, S. Deneault, T. M. Lyszczarz, D. Flechtner, and R. Wright. Exceptionally high voltage schottky diamond diodes and low boron doping. *Semiconductor Science and Technology*, 18(3):S67–S71, 2003.
- [93] M.W. Gels and J.C. Twichell. Hole traps in natural type iib diamond. *IEEE Transactions on Electron Devices*, 44(9):1514–1522, 1997.
- [94] R. Abrams, C. Hor, J. Yater, and A. Shih. Secondary electron emission studies. *Applied Surface Science*, 111:251–258, 1997.
- [95] G. Brandes and J. Miller. Effects of dopant concentration, crystallographic orientation, and crystal morphology on secondary electron emission from diamond. *Journal of Applied Physics*, 82(9):4538, 1997.
- [96] K. O’Donnell, T. Martin, M. Edmonds, A. Tadich, L. Thomsen, J. Ristein, C. Pakes, N. Fox, and L. Ley. Photoelectron emission from lithiated diamond. *physica status solidi (a)*, 211(10):2209–2222, 2014.
- [97] D. E. Eastman, J. A. VanVechten, J. A. Knapp, and F. J. Himpsel. Quantum photoyield of diamond(111)- a stable negative-affinity emitter. *Physical Review B*, 20(2):624–627, 1979.

- [98] L. Ley, J. Ristein, B. Mantel, M. Riedel, and F. Maier. Origin of surface conductivity in diamond. *Physical Review Letters*, 85(16):3472–3475, 2000.
- [99] C.J.H. Wort and R.S. Balmer. Diamond as an electronic material. *Materials Today*, 11(1-2):22–28, 2008.
- [100] M. Latto. *The Electrochemistry of Diamond*. PhD thesis, University of Bristol, 2001.
- [101] P. Volpe, J. Pernot, P. Muret, and F. Omnés. High hole mobility in boron doped diamond for power device applications. *Applied Physics Letters*, 94(9):092102, 2009.
- [102] M. A. Plano, M. I. Landstrass, L. S. Pan, S. Han, D. R. Kania, S. McWilliams, and J. W. Ager. Polycrystalline CVD diamond films with high electrical mobility. *Science*, 260(5112):1310–1312, 1993.
- [103] H. Pernegger, S. Roe, P. Weilhammer, V. Eremin, H. Fraiss-Kolbl, E. Griesmayer, H. Kagan, S. Schnetzer, R. Stone, and W. et al. Trischuk. Charge-carrier properties in synthetic single-crystal diamond measured with the transient-current technique. *Journal of Applied Physics*, 97(7):073704, 2005.
- [104] W. Brauer and O. Hachenberg. Secondary electron emission from solids. *Advances in Electronics and Electron Physics*, 11:413–499, 1959.
- [105] M. Zadrazil, A.M.D. Assad, M.M. El-Gomati, and C.G.H. Walker. The secondary electron emission yield for 24 solid elements excited by primary electrons in the range 250-5000 eV: A theory/experiment comparison. *Scanning*, 30(5):365–380, 2008.
- [106] C. Delfaure, M. Pomorski, J. de Sanoit, P. Bergonzo, and S. Saada. Single crystal CVD diamond membranes for betavoltaic cells. *Applied Physics Letters*, 108(25):252105, 2016.
- [107] L. Schlapbach, P. Aebi, T. Pillo, P. Ruffieux, O.M. Kuttel, and L. Diederich. Photoelectron emission from nitrogen- and boron-doped diamond (100) surfaces. *Surface Science*, 417(1):41–52, 1998.
- [108] B. Pate and C. Bandis. Electron emission due to exciton breakup from negative electron affinity diamond. *Physical Review Letters*, 74(5):777–780, 1995.
- [109] J.R.M. Vaughan. A new formula for secondary emission yield. *IEEE Transactions on Electron Devices*, 36(9):1963–1967, 1989.

- [110] R. Vaz, P.W. May, N.A. Fox, C.J. Harwood, V. Chatterjee, J.A. Smith, C.J. Horsfield, J.S. Lapington, and S. Osbourne. Measurement of the secondary electron emission from CVD diamond films using phosphor screen detectors. *Journal of Instrumentation*, 10(03):P03004–P03004, 2015.
- [111] J. E. Yater and A. Shih. Secondary electron emission characteristics of single-crystal and polycrystalline diamond. *Journal of Applied Physics*, 87(11):8103–8112, 2000.
- [112] M. Nazare and A. Neves. *Properties, growth and applications of diamond*. INSPEC, 1 edition, 2001.
- [113] E. J. Sternglass and G. W. Goetze. Field-enhanced transmission secondary emission for high-speed counting. *IRE Transactions on Nuclear Science*, 9(3):97–102, 1962.
- [114] J.E. Yater, J.L. Shaw, K.L. Jensen, T. Feygelson, R.E. Myers, B.B. Pate, and J.E. Butler. Secondary electron amplification using single-crystal CVD diamond film. *Diamond and Related Materials*, 20(5-6):798–802, 2011.
- [115] T. Anthony and W. Banholzer. Properties of diamond with varying isotopic composition. *Diamond and Related Materials*, 1(5-6):717–726, 1992.
- [116] J. Goldstein. *Scanning electron microscopy and x-ray microanalysis*. Springer-Verlag, 3 edition, 2003.
- [117] W. M. Haynes, T. J. Bruno, and David R. Lide. *CRC handbook of chemistry and physics*. CRC Press, 84 edition, 2015.
- [118] A. Shih, J. Yater, P. Pehrsson, J. Butler, C. Hor, and R. Abrams. Secondary electron emission studies of diamond surfaces. *MRS Proceedings*, 416, 1995.
- [119] D. A. Dimitrov, R. Busby, D. L. Bruhwiler, J. R. Cary, I. Ben Zvi, T. Rao, X. Chang, J. Smedley, and Q. Wu. 3d simulations of secondary electron generation and transport in a diamond amplifier for photocathodes. *2007 IEEE Particle Accelerator Conference (PAC)*, 2007.
- [120] J. Warner. *The handbook of lithium-ion battery pack design*. Elsevier Science, 1 edition, 2015.
- [121] C. Chukwuka and K.A. Folly. Batteries and super-capacitors. *IEEE Power and Energy Society Conference and Exposition in Africa: Intelligent Grid Integration of Renewable Energy Resources (PowerAfrica)*, 2012.
- [122] S. Kumar. Atomic batteries: Energy from radioactivity. *Journal of Nuclear Energy Science & Power Generation Technology*, 05(01), 2015.

- [123] C. Liu, P. Chen, and K. Li. A 1 kw thermoelectric generator for low-temperature geothermal resources. *Thirty-Ninth Workshop on Geothermal Reservoir Engineering*, 2014.
- [124] R. Duggirala. *Radioisotope thin-film powered microsystems*. Springer-Verlag New York, 1 edition, 2014.
- [125] K. Bower. *Polymers, phosphors, and voltaics for radioisotope microbatteries*. CRC Press, 1 edition, 2002.
- [126] M. Romer, G.H. Miley, and N. Luo. Computer-based study of secondary emission cell (sec) efficiency compared to that of a vacuum-type direct collection cell. *IEEE Transactions on Energy Conversion*, 23(1):331–341, 2008.
- [127] D. Schalch and A. Scharmann. Limits of a tritium battery based on charged particle collection. *Atomkernenergie Kerntechnik*, 37(1):13–15, 1981.
- [128] B. Liu, K. Chen, N. Kherani, S. Zukotynski, and A. Antoniazzi. Betavoltaics using scandium tritide and contact potential difference. *Applied Physics Letters*, 92(8):083511, 2008.
- [129] G. Yakubov. *Nuclear Batteries with Tritium And Promethium-147 Radioactive Sources*. PhD thesis, University of Illinois, 2010.
- [130] S. Revankar and T. Adams. Advances in betavoltaic power sources. *Journal of Energy and Power Sources*, 1(6):321–329, 2014.
- [131] L. Olsen, P. Cabauy, and B. Elkind. Betavoltaic power sources. *Physics Today*, 65(12):35–38, 2012.
- [132] W. Sun, N. P. Kherani, K. D. Hirschman, L. L. Gadeken, and P. M. Fauchet. A three-dimensional porous silicon p-n diode for betavoltaics and photovoltaics. *Advanced Materials*, 17(10):1230–1233, 2005.
- [133] C. J. Eiting, V. Krishnamoorthy, S. Rodgers, T. George, J. David Robertson, and John Brockman. Demonstration of a radiation resistant, high efficiency sic betavoltaic. *Applied Physics Letters*, 88(6):064101, 2006.
- [134] T Adams, S Revankar, P Cabauy, L Olsen, B Elkind, and J Grant. Status of betavoltaic power sources for nano and micro power applications. *45th Power Sources Conference*, 2012.
- [135] Z. Cheng, X. Chen, H. San, Z. Feng, and B. Liu. A high open-circuit voltage gallium nitride betavoltaic microbattery. *Journal of Micromechanics and Microengineering*, 22(7):074011, 2012.

- [136] A.V. Sachenko, A.I. Shkrebti, R.M. Korkishko, V.P. Kostylyov, M.R. Kulish, and I.O. Sokolovskiy. Efficiency analysis of betavoltaic elements. *Solid-State Electronics*, 111:147–152, 2015.
- [137] H. Chen, J. Yin, and D. Li. Electrode pattern design for gaas betavoltaic batteries. *Journal of Semiconductors*, 32(8):084006, 2011.
- [138] C. Munson, M. Arif, J. Streque, S. Belahsene, A. Martinez, and A. Ramdane. Model of Ni-63 battery with realistic pin structure. *Journal of Applied Physics*, 118(10):105101, 2015.
- [139] C. Bauer, I. Baumann, and C. Colledani. Radiation hardness studies of CVD diamond detectors. *Nuclear Instruments and Methods in Physics Research Section A: Accelerators, Spectrometers, Detectors and Associated Equipment*, 367(1-3):207–211, 1995.
- [140] M. Brezeanu, T. Butler, N. Rupesinghe, S.J. Rashid, M. Avram, G.A.J. Amaratunga, F. Udrea, M. Dixon, D. Twitchen, and A. et al. Garraway. Single crystal diamond mip diodes for power electronics. *IET Circuits, Devices & Systems*, 1(5):380, 2007.
- [141] H. Umezawa, Y. Mokuno, H. Yamada, A. Chayahara, and S. Shikata. Characterization of schottky barrier diodes on a 0.5-inch single-crystalline CVD diamond wafer. *Diamond and Related Materials*, 19(2-3):208–212, 2010.
- [142] V. Bormashov, S. Troschiev, A. Volkov, S. Tarelkin, E. Korostylev, A. Golovanov, M. Kuznetsov, D. Teteruk, N. Kornilov, and S. Terentiev. Development of nuclear microbattery prototype based on schottky barrier diamond diodes. *physica status solidi (a)*, 212(11):2539–2547, 2015.
- [143] S. Seidal. Recent results on diamond radiation tolerance. *Journal of Instrumentation*, 9:113–121, 2014.
- [144] Y. Uhm, B. Choi, J. Kim, D. Jeong, and K. Son. Study of a betavoltaic battery using electroplated nickel-63 on nickel foil as a power source. *Nuclear Engineering and Technology*, 48(3):773–777, 2016.
- [145] B. Liu, K. Chen, N. Kherani, and S. Zukotynski. Power-scaling performance of a three-dimensional tritium betavoltaic diode. *Applied Physics Letters*, 95(23):233112, 2009.
- [146] H. Li, A. Lal, J. Blanchard, and D. Henderson. Self-reciprocating radioisotope-powered cantilever. *Journal of Applied Physics*, 92(2):1122–1127, 2002.

- [147] H. Guo and A. Lal. Nanopower betavoltaic microbatteries. *12th International Conference on Transducers, Solid-State Sensors, Actuators and Microsystems*, pages 36–39, 2003.
- [148] V. Kapur and B. Basol. Status of polycrystalline solar cell technologies. *Conference Record of the IEEE Photovoltaic Specialists Conference*, pages 23–30, 1992.
- [149] K. Wong and S. Dia. Nanotechnology in batteries. *Journal of Energy Resources Technology*, 139:14001, 2016.
- [150] H. Seidel. Anisotropic etching of crystalline silicon in alkaline solutions. *Journal of The Electrochemical Society*, 137(11):3612, 1990.
- [151] S. A. Solin and A. K. Ramdas. Raman spectrum of diamond. *Physical Review B*, 1(4):1687–1698, 1970.
- [152] L. van der Pauw. A method of measuring specific resistivity and hall effect of discs of arbitrary shape. *Philips Research Reports*, 13(1), 1958.
- [153] J. Filik. Raman spectroscopy: A simple, non-destructive way to characterise diamond and diamond-like materials. *Spectroscopy Europe*, 17(5), 2005.
- [154] F. Adar, E. Lee, S. Mamedov, and A. Whitley. Experimental evaluation of the depth resolution of a raman microscope. *Microscopy and Microanalysis*, 16(S2):360–361, 2010.
- [155] S.J. Rashid, A. Tajani, D.J. Twitchen, L. Coulbeck, F. Udrea, T. Butler, N.L. Rupesinghe, M. Brezeanu, J. Isberg, and A. et al. Garraway. Numerical parameterization of chemical-vapor-deposited (CVD) single-crystal diamond for device simulation and analysis. *IEEE Transactions on Electron Devices*, 55(10):2744–2756, 2008.
- [156] A. Aksenova, A. Altuhov, E. Ryabeva, V. Samosadnyi, V. Feshchenko, A. Chernyaev, and V. Shepelev. The investigation of boron-doped diamond absorbance spectrum. *Journal of Physics: Conference Series*, 798:012149, 2017.
- [157] V. Richter, B. Fizeer, Sh. Michaelson, A. Hoffman, and R. Kalish. Escape depth of secondary electrons induced by ion irradiation of submicron diamond membranes. *Journal of Applied Physics*, 96(10):5824–5829, 2004.
- [158] A. Brambilla, D. Tromson, P. Bergonzo, C. Mer, and F. Foulon. Thin CVD diamond detectors with high charge collection efficiency. *IEEE Transactions on Nuclear Science*, 49(1):277–280, 2002.

-
- [159] D. Alloni, C. Cutaia, L. Mariotti, W. Friedland, and A. Ottolenghi. Modeling dose deposition and dna damage due to low-energy emitters. *Radiation Research*, 182(3):322–330, 2014.
- [160] S. Kone, G. Civrac, H. Schneider, K. Isoird, R. Issaoui, J. Achard, and A. Gicquel. CVD diamond schottky barrier diode, carrying out and characterization. *Diamond and Related Materials*, 19(7-9):792–795, 2010.
- [161] J.C. Madaleno, S.C. Trippe, and L. Pereira. Comparison of the electrical behavior of schottky diodes built on the nucleation and growth surfaces of polycrystalline diamond. *Diamond and Related Materials*, 16(4-7):926–929, 2007.
- [162] Q. Zhang, R. Chen, H. San, G. Liu, and K. Wang. Betavoltaic effect in titanium dioxide nanotube arrays under build-in potential difference. *Journal of Power Sources*, 282:529–533, 2015.